

**ELECTROCHEMICAL PERFORMANCE OF
MANGANESE-BASED COMPOSITE
ELECTRODE FOR SUPERCAPACITOR
APPLICATION**

CHAN PEI YI

**FACULTY OF SCIENCE
UNIVERSITY OF MALAYA
KUALA LUMPUR**

2017

**ELECTROCHEMICAL PERFORMANCE OF
MANGANESE-BASED COMPOSITE
ELECTRODE FOR SUPERCAPACITOR
APPLICATION**

CHAN PEI YI

**THESIS SUBMITTED IN FULFILMENT OF THE
REQUIREMENTS FOR THE DEGREE OF
DOCTOR OF PHILOSOPHY**

**DEPARTMENT OF PHYSICS
FACULTY OF SCIENCE
UNIVERSITY OF MALAYA
KUALA LUMPUR**

2017

**UNIVERSITY OF MALAYA
ORIGINAL LITERARY WORK DECLARATION**

Name of Candidate: **CHAN PEI YI**

Matric No: **SHC 140044**

Name of Degree: Doctor of Philosophy

Title of Project Paper/Research Report/Dissertation/Thesis (“this Work”):

Electrochemical Performance of Manganese-based Composite Electrode for Supercapacitor Application

Field of Study: **Experimental Physics**

I do solemnly and sincerely declare that:

- (1) I am the sole author/writer of this Work;
- (2) This Work is original;
- (3) Any use of any work in which copyright exists was done by way of fair dealing and for permitted purposes and any excerpt or extract from, or reference to or reproduction of any copyright work has been disclosed expressly and sufficiently and the title of the Work and its authorship have been acknowledged in this Work;
- (4) I do not have any actual knowledge nor do I ought reasonably to know that the making of this work constitutes an infringement of any copyright work;
- (5) I hereby assign all and every rights in the copyright to this Work to the University of Malaya (“UM”), who henceforth shall be owner of the copyright in this Work and that any reproduction or use in any form or by any means whatsoever is prohibited without the written consent of UM having been first had and obtained;
- (6) I am fully aware that if in the course of making this Work I have infringed any copyright whether intentionally or otherwise, I may be subject to legal action or any other action as may be determined by UM.

Candidate’s Signature

Date:

Subscribed and solemnly declared before,

Witness’s Signature

Date:

Name:

Designation:

ABSTRACT

There were three manganese-based composite electrode systems being prepared in this work: (1) reduced graphite oxide-manganese oxide, (2) manganese-nickel oxide and (3) manganese oxide-poly (3, 4-ethylenedioxythiophene): poly (styrenesulfonate) (PEDOT: PSS). A two-electrode configuration of chronopotentiometry technique, with a constant current density of 2 mA cm^{-2} was applied for the preparation of composite electrodes. A stainless steel plate was acted as the substrate. The composite films deposited on stainless steel, or composite electrodes, were characterised by X-ray diffraction (XRD), field emission scanning electron microscopy (FESEM), transmission electron microscopy (TEM), cyclic voltammetry (CV), galvanostatic charge-discharge (GCD) and frequency response analysis (FRA). The changes in morphology, crystalline nature and electrochemical behaviours of the composite electrodes under the effect of deposition duration were investigated. In the first composite electrode system, the sheet-like reduced graphite oxide (RGO) was covered over the particles deposited on the substrate. It acted as a conductive pathway for electronic and ionic transportation. This composite electrode exhibited the highest specific capacitance when it was deposited at 13 mins. The continuous growth of particle with longer deposition duration led to the broken of RGO sheet, which subsequently affected the electrochemical performance. Second composite electrode system prepared, manganese-nickel oxide presented as a spongy-like structure under FESEM examination. There was no distinct boundary observed from FESEM images, indicating that two compositions had entangled well to each other. In this composite electrode system, 13 mins-deposited composite electrode obtained the best electrochemical performance. The manganese oxide-PEDOT: PSS as the third composite electrode system, was deposited in shorter duration (less than 1 min) compared with another two composite electrode systems due to the weaker adsorption on stainless steel. The morphology transformed from globular

to more fibrous structure when the electrodeposition was carried out for longer duration. This improved the electronic and ionic transportation in the composite film. PEDOT: PSS enhanced the specific capacitance of manganese oxide by acting as conductive pathway for electron and ions. In this system, the composite electrode that was deposited at 40 s performed the best electrochemical performance.

University of Malaya

ABSTRAK

Dalam tesis ini, tiga sistem elektrod komposit berasaskan mangan telah disediakan iaitu grafit oksida terturun-mangan oksida, mangan-nikel oksida, dan mangan oksida-*poly (3, 4-ethylenedioxythiophene): poly (styrenesulfonate)*. Teknik yang diaplikasikan ialah kronopotensimetri dengan menggunakan ketumpatan arus elektrik tetap (2 mA cm^{-2}) dalam konfigurasi dua-elektrod. Keluli tahan karat digunakan sebagai substrat di mana filem komposit akan dimendapkan di atasnya. Elektrod komposit yang tersedia dicirikan dengan menggunakan spektrometer pembelauan sinar-X (XRD), mikroskop pengimbas elektron medan pancaran (FESEM), mikroskop penghantaran elektron (TEM), voltammetri siklik (CV), galvanostatik cas dan nyahcas (CD) serta analisa sambutan frekuensi (FRA). Perubahan dalam morfologi, kehabluran, dan prestasi elektrokimia telah dianalisis. Dalam sistem elektrod komposit yang pertama, RGO muncul sebagai helaian yang menutupi zarah yang termendap atas substrat. Ia bertindak sebagai laluan pengangkutan untuk elektron dan ion. Elektrod komposit ini memperlihatkan kapasitans spesifik tertinggi apabila masa elektromendapan ialah 13 minit. Pertumbuhan zarah selanjor dengan tempoh masa elektromendapan boleh membawa kepada penghuraian helaian RGO yang kemudiannya menjejaskan prestasi elektrokimia. Mangan-nikel oksida, sebagai sistem elektrod komposit yang kedua, menunjukkan struktur span di bawah pemeriksaan FESEM. Imej FESEM tidak memaparkan sempadan yang jelas menunjukkan dua komposisi terpuntal baik sesame sendiri. Elektrod komposit dalam sistem ini yang dielektromendapkan selama 13 minit mempamerkan kapasitans speksifik tertinggi. Untuk sistem elektrod komposit yang ketiga, mangan oksida-PEDOT: PSS telah dielektromendapkan dalam jangka masa lebih pendek (kurang daripada 1 minit) berbanding dengan dua elektrod komposit yang lain disebabkan penjerapan yang lemah ke atas keluli tahan karat. Morfologi telah berubah daripada globul kepada struktur lebih bergentian pada jangka masa

elektromendapan yang lebih panjang. Ini memperbaiki pengangkutan elektron dan ion dalam filem komposit. PEDOT: PSS meningkatkan kapasitans spesifik mangan oksida dengan bertindak sebagai laluan konduksian untuk elektron dan ion. Dalam system ini, komposit elektrod yang dielektromendapkan selama 40 s menunjukkan kapasitans spesifik yang tertinggi.

University of Malaya

ACKNOWLEDGEMENTS

Firstly, I would like to express my deepest gratitude to my beautiful supervisor, Assoc. Prof. Dr. Siti Rohana Majid for the support and inspiration during my study. Research life is never easy and sometimes disappointing. However, my supervisor is like the Sun, shining her students with her knowledge and encouragement. She is like a lighthouse, led me through the challenges and moved forward in the dark. As a lecturer, she has to carry out lecture classes and guide in our experiments. I appreciate all the helps she has offered. I am not a typical brilliant student but I strive for excellence under her supervision.

Next, I wish to show my sincere thanks to the head of research centre I worked in: Prof. Dr. Abdul Kariem. He is a guider in not only researches, but also life. He always push us to limit and encourage us to go beyond ourselves. He offers many opportunities in order to expand our visions and life core values. The most respectful part of him is, he believes on us and never give up on any of us.

There are a lot of friendly and supportive labmates accompanied me while I pursued my study. They are my comrades and also my friends. Thanks to Dr. Woo, Dr. Teo, Dr. Hamdi, Dr. Sim, Dr. Liew, Dr. Jun, and Dr. Rusi, Jin Pin, and Chee Meng who provided me professional advices in doing researches; Kim, Syaza, Shah, Hanod, Myron, and Hon Ming who has offered me various help and encouragement; Mr. Ismail, Dhruv, Ammar, Farhana, Helmy, Rohaida, Mira, Ema, Syu, Najla, Dilla, Liyana etc who has been joined part of my research journey. I enjoyed the moment working together with them. Also thanks to the scholarship (SBUM) provided by University of Malaya.

Last but not least, I want to thank my family for their endless love and support.

Here, I would like to share a quote to end my acknowledgement.

‘Experience is what you get when you did not get what you wanted. And experience is often the most valuable thing you have to offer.’ *-The Last Lecture-*

TABLE OF CONTENTS

ABSTRACT	iii
ABSTRAK	v
ACKNOWLEDGEMENTS	vii
TABLE OF CONTENTS	viii
LIST OF FIGURES	xii
LIST OF TABLES	xv
LIST OF SYMBOLS AND ABBREVIATIONS	xvi
CHAPTER 1: INTRODUCTION	1
1.1 Research background	1
1.2 Objectives	3
1.3 Organisation of the thesis	3
CHAPTER 2: LITERATURE REVIEW	5
2.1 Introduction	5
2.2 Brief history and development of supercapacitor.....	7
2.3 Energy storage principles of supercapacitor.....	10
2.3.1 Electric double layer capacitor (EDLC).....	10
2.3.2 Pseudocapacitor.....	15
2.4 Electrode materials for supercapacitor	17
2.4.1 Carbon	17
2.4.2 Graphene	19
2.4.3 Transition metal oxides	21

2.4.4	PEDOT: PSS (Conducting polymer).....	35
2.5	Electrolyte	40
2.6	Electrodeposition.....	42
2.6.1	General principle of electrodeposition	43
2.7	Summary	44
CHAPTER 3: EXPERIMENTAL METHOD		46
3.1	Introduction	46
3.2	Composite electrode preparation.....	47
3.2.1	Reduced graphite oxide-manganese oxide	47
3.2.2	Manganese-nickel oxide.....	48
3.2.3	Manganese oxide-PEDOT: PSS.....	49
3.3	List of chemicals and materials	49
3.4	Characterisations	50
3.4.1	Field emission scanning electron microscopy (FESEM)	50
3.4.2	Transmission electron microscopy (TEM).....	51
3.4.3	X-ray diffraction (XRD).....	51
3.4.4	Electrochemical tests	52
CHAPTER 4: CHARACTERISATIONS OF REDUCED GRAPHITE OXIDE-MANGANESE OXIDE COMPOSITE ELECTRODE SYSTEM		59
4.1	Introduction	59
4.2	Reduced graphite oxide (RGO).....	60

4.3	Field emission scanning electron microscopy (FESEM)	61
4.4	XRD study	63
4.5	Electrochemical performance	65
4.5.1	Cyclic voltammetry (CV)	65
4.5.2	Galvanostatic charge-discharge (GCD).....	68
4.5.3	Frequency response analysis (FRA).....	70
4.6	Cycle stability	72
4.7	Summary	73
CHAPTER 5: CHARACTERISATIONS OF MANGANESE-NICKEL		
OXIDE COMPOSITE ELECTRODE SYSTEM.....		
5.1	Introduction	74
5.2	Field emission scanning electron microscopy (FESEM)	74
5.3	Transmission electron microscopy (TEM).....	75
5.4	X-ray diffraction (XRD).....	77
5.5	Electrochemical performances	77
5.5.1	Cyclic voltammetry (CV)	77
5.5.2	Galvanostatic charge-discharge (GCD).....	81
5.5.3	Impedance analysis and cycle stability.....	83
5.6	Summary	88

CHAPTER 6: CHARACTERISATIONS OF MANGANESE OXIDE- PEDOT: PSS COMPOSITE ELECTRODE SYSTEM.....	89
6.1 Introduction.....	89
6.2 Field emission scanning electron microscopy (FESEM).....	90
6.3 Transmission electron microscopy (TEM).....	93
6.4 X-ray diffraction (XRD).....	94
6.5 Cyclic voltammetry (CV).....	95
6.6 Galvanostatic charge-discharge (GCD).....	98
6.7 Frequency response analysis (FRA).....	100
6.8 Summary.....	103
 CHAPTER 7: DISCUSSIONS.....	 104
 CHAPTER 8: CONCLUSION AND SUGGESTIONS ON FUTURE WORK.....	 113
8.1 Conclusion.....	113
8.2 Suggestions on future work.....	115
 REFERENCES.....	 116
 LIST OF PUBLICATIONS AND PAPERS PRESENTED.....	 136

LIST OF FIGURES

Figure 2.1:	Basic construction of a capacitor.....	5
Figure 2.2:	Family of capacitor.....	7
Figure 2.3:	Configuration of (a) electrostatic capacitor and (b) aluminium electrolytic capacitor.....	8
Figure 2.4:	Models of the double layer: (a) Helmholtz model, (b) Gouy-Chapman (G-C) model, (c) Stern model and (d) Bockris, Devanathan, Müller (BDM) model.....	12
Figure 2.5:	Configuration of electric double layer capacitor (EDLC).....	14
Figure 2.6:	Hexagonal lattice of graphene.....	20
Figure 3.1:	Excitation signal of CV.....	52
Figure 3.2:	A typical cyclic voltammogram.....	53
Figure 3.3:	GCD plots of (a) EDLC and (b) pseudocapacitive materials.....	55
Figure 3.4:	Stationary polarisation curve (black bold line). The measurement of resulting current when a sinusoidal voltage is imposed over a steady voltage.....	57
Figure 4.1:	(a) UV-VIS spectra of GO and RGO and (b) the images of GO (left) and RGO (right).....	60
Figure 4.2:	FESEM image of composite film deposited at 10 mins.....	61
Figure 4.3:	FESEM images of RGO-manganese oxide deposited at (a) 13 mins, (b) 15 mins and (c) 18 mins at 200k of magnification.....	62
Figure 4.4:	EDX analysis of composite electrode.....	62
Figure 4.5:	XRD pattern of (a) composite electrodes, (b) bare stainless steel and (c) scraped off composite films.....	63
Figure 4.6:	(a) CV curves of composite electrodes at 1 mV s^{-1} , (b) CV curves of RM 13 at different scan rates and (c) graph of specific capacitance against scan rate (RM 13).....	65
Figure 4.7:	Galvanostatic (a) discharging curves of composite electrodes at various deposition duration and charge-discharge curves of (b) RM 15, (c) RM 13 at different currents.....	69
Figure 4.8:	Impedance test result of composite electrode deposited at different durations (a) Nyquist plot, (b) equivalent circuit, and fitted Nyquist plot at (c) 10 mins, (d) 13 mins, (e) 15 mins and (f) 18 mins.....	71

Figure 4.9:	(a) Capacitance retention percentage and (b) normalised current density as a function of cycle number for RM 13.....	72
Figure 5.1:	FESEM images of composite films deposited at (a) 10 mins, (b) 13 mins, (c) 15 mins and (d) 18 mins.....	75
Figure 5.2:	TEM images of composite films deposited at (a) 10 mins, (b) 13 mins, (c) 15 mins and (d) 18 mins at 40k magnifications.....	76
Figure 5.3:	XRD patterns of composite film deposited at different durations.....	77
Figure 5.4:	(a) CV curves of composite films deposited at different deposition durations at 1 mV s^{-1} , (b) specific capacitances obtained at various deposition durations, (c) composite film weights varied with deposition durations and (d) normalized CV curves of composite film deposited at 13 mins for different scan rates.....	78
Figure 5.5:	Discharging curve of composite films deposited at (a) different durations at 1 A g^{-1} and (b) 13 mins at various current densities.....	81
Figure 5.6:	(a) Nyquist plots for composite film deposited at different durations, (b) corresponding equivalent circuit, and Nyquist plot with fitted impedance curves at different deposition durations: (c) 10 mins, (d) 13 mins, (e) 15 mins and (f) 18 mins.....	84
Figure 5.7:	Bode plots of (a) phase angle versus frequency (in logarithmic scale) and (b) absolute impedance $ Z $ versus frequency (in logarithmic scale).....	86
Figure 5.8:	(a) Capacitance retention test of 13 mins-deposited composite film for 1000 cycles at 10 mV s^{-1} and (b) CV curves at different cycle numbers.....	87
Figure 6.1:	Morphologies of composite films deposited at different durations: (a, b) 10 s, (c, d) 20 s, (e, f) 30 s, (g, h) 40 s and (i, j) 50 s.....	90
Figure 6.2:	FESEM images of manganese oxide deposited at 40 s without PEDOT: PSS with magnification of (a) 50k and (b) 200k.....	92
Figure 6.3:	TEM images of composite film deposited at (a) 10 s, (b) 20 s, (c) 30 s, (d) 40 s and (e) 50 s.....	93
Figure 6.4:	XRD patterns of composite films deposited at various duration.....	94
Figure 6.5:	(a) Cyclic voltammetry curves of composite electrode at various deposition durations at 1 mV s^{-1} , (b) relationship between specific capacitance and deposition duration, (c) cyclic voltammetry curves of MP 40 at different scan rates (d) comparison of cyclic.....	95

Figure 6.6:	Galvanostatic (a) discharging curves of composite electrodes prepared at different deposition durations, (b) charge-discharge curves of 40 s-deposited composite electrode at various current densities and (c) discharging curves of film with and without PEDOT: PSS.....	98
Figure 6.7:	(a, b) Nyquist plots of the composite films deposited at different durations, (c) Nyquist plots of experimental and fitted data of 40 s-deposited composite electrode, (d) equivalent circuit of deposited composite film, Bode plots of (e) phase angle versus frequency (in logarithmic scale) and (f) absolute impedance $ Z $ versus frequency (in logarithmic scale).....	100
Figure 7.1:	Deposition mechanisms of (a) RGO-manganese oxide, (b) manganese-nickel oxide and (c) manganese oxide-PEDOT: PSS.....	105
Figure 7.2:	Images of composite electrodes (a) before and (b) after peeling off the adhesive tapes.....	111

LIST OF TABLES

Table 2.1:	Literature review on RuO ₂ -based electrode.....	22
Table 2.2:	Literature review on manganese oxide-based electrode.....	30
Table 2.3:	Literature review on nickel oxide-based electrode.....	34
Table 2.4:	Literature review on PEDOT: PSS-based electrode.....	39
Table 3.1:	Name of samples in reduced graphite oxide-manganese oxide composite electrode system.....	48
Table 3.2:	Designation of samples for manganese-nickel oxide composite electrode system.....	50
Table 3.3:	Sample names for manganese oxide-PEDOT: PSS composite electrode system.....	50
Table 3.4:	Information of chemicals and materials in the experiment.....	51
Table 4.1:	Specific capacitances estimated for composite electrodes deposited at different durations.....	67
Table 5.1:	Specific capacitances obtained at different scan rates for 13 mins-deposited composite film.....	80
Table 5.2:	Specific capacitances obtained from CV and GCD at various deposition durations.....	83
Table 5.3:	Specific energy and specific power estimated from C _{GCD} at 1 A g ⁻¹ for composite film deposited at different durations.....	83
Table 5.4:	Fitted values of equivalent circuit components for Nyquist plots at different deposition durations.....	86
Table 7.1:	Comparison study on three composite electrode systems.....	109

LIST OF SYMBOLS AND ABBREVIATIONS

A	:	Surface area
C	:	Capacitance
C_{cell}	:	Cell capacitance
C_{dl}	:	Double layer capacitance
C_{ϕ}	:	Pseudocapacitance
C_{sp}	:	Specific capacitance
d	:	Gap distance
ϵ	:	Dielectric constant
ϵ_r	:	Relative permittivity of the dielectric
f	:	Frequency
Q	:	Charge stored in a capacitor
ϕ	:	Phase angle
R_s	:	Solution resistance
R_{ct}	:	Charge transfer resistance
R_{ESR}	:	Equivalent series resistance
t	:	Time
ν	:	Scan rate
V	:	Potential difference
W	:	Warburg element
Z'	:	Real impedance
Z''	:	Imaginary impedance
3D	:	3-dimensional
AC	:	Activated carbon
BMIBF ₄	:	1-butyl-3-methylimidazolium tetrafluoroborate
BMIPF ₆	:	1-butyl-3-methylimidazolium hexafluorophosphate

BDM	:	Bockris, Devanathan, Müller
CNT	:	Carbon nanotube
Co	:	Cobalt
Co(NH ₂) ₂	:	Urea
Co ₃ O ₄	:	Cobalt (II, III) oxide
CPE	:	Constant phase element
CV	:	Cyclic voltammetry
CVD	:	Chemical vapour deposition
EC	:	Electrochemical capacitor
EDLC	:	Electric double layer capacitor
EDX	:	Energy-dispersive X-ray spectroscopy
Fe	:	Iron
FESEM	:	Field emission scanning electron microscopy
FRA	:	Frequency response analysis
G-C	:	Gouy-Chapman model
GCD	:	Galvanostatic charge-discharge
GO	:	Graphite oxide
HCl	:	Hydrochloric acid
H ₂ SO ₄	:	Sulphuric acid
H ₂ O ₂	:	Hydrogen peroxide
H ₃ PO ₄	:	Phosphoric acid
IHP	:	Inner Helmholtz plane
IL	:	Ionic liquid
KMnO ₄	:	Potassium permanganate
LDH	:	Layered double hydroxide
Mn	:	Manganese

MnO ₂	:	Manganese oxide
Mn ₃ O ₄	:	Manganese (II, III) oxide
MCMB	:	Meso-carbon microbeads
MWCNT	:	Multi-walled carbon nanotube
NaOH	:	Sodium hydroxide
Na ₂ SO ₄	:	Sodium sulphate
(NH ₄)CO ₂	:	Ammonium carbonate
Ni	:	Nickel
NiCo ₂ O ₄	:	Nickel cobaltite
NiO	:	Nickel oxide
Ni(OH) ₂	:	Nickel hydroxide
OHP	:	Outer Helmholtz plane
PANI	:	Polyaniline
PEDOT: PSS	:	Poly (3, 4-ethylenedioxythiophene): poly (styrenesulfonate)
PIP ₁₃ -FSI	:	N-methyl-N-propylpiperidinium bis(fluorosulfonyl)imide
PVDF	:	Polyvinylidene fluoride
PYR ₁₄ -FSI	:	N-butyl-N-methylpyrrolidinium bis(fluorosulfonyl)imide
RGO	:	Reduced graphite oxide
RuO ₂	:	Ruthenium oxide
rpm	:	revolutions per minute
SDS	:	Sodium dodecyl sulfate
SILAR	:	Successive ionic layer adsorption and reaction
SWCNT	:	Single-walled carbon nanotube
XRD	:	X-ray diffraction

CHAPTER 1: INTRODUCTION

1.1 Research background

The rapid development of portable electronic devices to the electrification of the transportation sector has increased the growth of energy storage devices (ESDs). ESDs such as battery, capacitor, fuel cell and flywheels store energy in the specific form of chemical, electrochemical, electromagnetic, or kinetic. Firstly, I would like to introduce the most common ESD, which is a battery.

Battery, as an electrochemical cell, produces electrical energy from the conversion of chemical energy. It is favourable by many applications because of its high energy capacity. Different types of batteries have been developed for specific purposes. Secondary batteries, or rechargeable batteries such as nickel-cadmium (NiCd) battery, nickel-metal-hydride (NiMH) battery and lead acid battery are the most common batteries. NiCd battery is famous for its long service life and endurance towards extreme temperature. However, special care is needed when disposing NiCd battery in a landfill because Cd is a toxic heavy metal that can pollute the environment. Some countries have already banned the usage of NiCd battery. Despite, NiMH battery are encouraged to be used and even replacing the NiCd battery. It is more environmental friendly compared with NiCd battery. Lead acid battery, is the oldest type of rechargeable battery and commonly used for starting automotive engines (Zu & Li, 2011). Among the rechargeable batteries, Li-ion battery is the fastest growing technology and slowly taking over the place of lead-based and nickel-based batteries in many applications. The invention of Li-ion battery has accelerated the growth of battery technology in terms of energy density from approximately 3 W h kg^{-1} to 5.5 W h kg^{-1} per year (Zu & Li, 2011). It has high energy density of $100 - 180 \text{ W h kg}^{-1}$, which is typically twice of NiMH (50 W h kg^{-1}) (Suksomboon et al., 2014). Li-ion battery is hazardous because of the high internal resistance that can cause burning or even explosion if it is shorted

accidentally (Wang et al., 2013). Hence, it needs a protection circuit to limit the voltage and current. Even though the battery technology is established, there are still some limitations on the development. As an energy storage device with high energy density, battery cannot fulfill the requirement in some applications that demand for short-term power need. Batteries designed for high power need are meant to sacrifice the energy density. This challenge has led to the growth and development of capacitor.

Due to the fact that the charge storage process of a battery involves redox reactions while a capacitor relies on electrostatic interaction, the achievable energy density of a capacitor is relatively lower. Nonetheless, this drawback is counteracted by other advantages such as long cycle life and good power performance. Nowadays, capacitor has evolved into 'supercapacitor' which can store more energy. Although the energy density is still considerably lower compared with a battery, the supercapacitor, as a high power device, can be used complementary with a battery. Supercapacitors are finding their ways and roles in electronic world. They have been considered to be used in several applications such as electric vehicle, electric hybrid vehicles, digital cameras, and digital communication devices (Miller, 2006; Pandolfo & Hollenkamp, 2006). In order to enhance the performance of a supercapacitor, attention should be focused on the improvement of energy density.

The electrochemical performance of a supercapacitor is dependent on the electrode material. Porous carbon, transition metal oxides, and conducting polymers are three main classes of electrode materials for supercapacitor. Previous studies have shown the enhancement in performance of supercapacitor since its first introduction (Acerce et al., 2015; Cuentas Gallegos & Rincón, 2006; Sawangphruk et al., 2012; Vijayakumar et al., 2013; Xie & Gao, 2007). Manganese oxide, reduced graphite oxide, nickel oxide and PEDOT: PSS were selected to be studied in this thesis (see Chapter 2 for more details).

This thesis, will therefore focus on the potential applications of these materials as composite electrodes in supercapacitors.

1.2 Objectives

The objectives of this thesis include

- To prepare and optimise the composite electrodes (reduced graphite oxide-manganese oxide, manganese-nickel oxide, and manganese oxide-PEDOT: PSS) in terms of electrodeposition duration using chronopotentiometry method.
- To investigate the effects of electrodeposition duration on the morphologies and structures of the prepared composite electrodes.
- To evaluate the electrochemical performances of the prepared composite electrodes.
- To determine the cycle stabilities of the optimised composite electrodes upon 1000 cycles.

1.3 Organisation of the thesis

The structure of this thesis can be summarized as follows.

Chapter 1 describes the motivation to study the electrode material of a supercapacitor, the objectives of carrying out this work, and the organisation of this thesis.

Chapter 2 focuses on the literature review inclusive of the brief history of the supercapacitor, energy storage mechanisms, and electrode materials of supercapacitor. Besides, the technique applied throughout the experiment will be introduced.

Chapter 3 explains the fabrication of composite electrodes. The characterisation techniques of the electrode materials also discussed in details.

Chapter 4 presents the characterisation results of the reduced graphite oxide-manganese oxide composite electrode. The electrochemical performance of this composite electrode is illustrated in this chapter.

Chapter 5 shows the characterisation results and electrochemical performance of the manganese-nickel oxide composite electrode.

Chapter 6 reports the characterisation results and electrochemical performance of the manganese oxide-PEDOT: PSS composite electrode.

Chapter 7 summarises and compares the properties and performances of three composite electrode systems.

Chapter 8 concludes the study of this work and provides the future prospect of this study.

CHAPTER 2:LITERATURE REVIEW

2.1 Introduction

A capacitor is a two-terminal electrical component that is used to store electrical energy, **Figure 2.1**. The amount of charge stored in a capacitor is termed as ‘capacitance’ (C), expressed in the unit of farad, which is abbreviated as ‘F’. Higher value of capacitance indicates more charge can be stored. The capacitance is dependent on the construction of a capacitor. According to **Equation 2.1**, C relies on the surface area of the conducting plate and the distance between two plates. The larger the surface area, the higher the capacitance. Besides, smaller gap distance between conducting plates allows more charge to be held, therefore higher capacitance can be achieved.

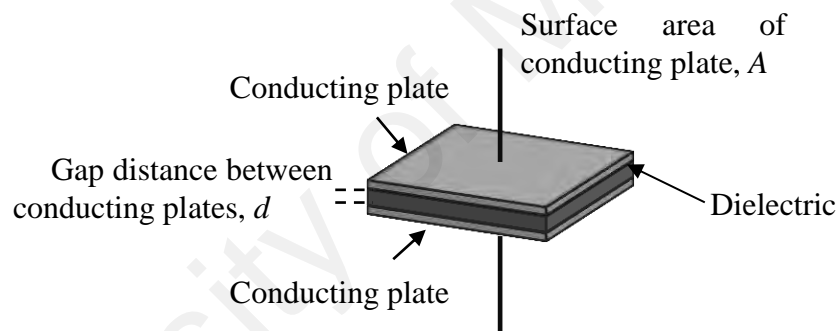


Figure 2.1: Basic construction of a capacitor.

$$C = \epsilon_r \frac{A}{4\pi d} \quad (2.1)$$

where ϵ_r (in unit of farad per meter) is the relative permittivity of the dielectric, A (in unit of squared meter) is the surface area of the conducting plate and d (in m) is the gap distance between the plates.

A capacitor is said to be ‘charged’ when the positive and negative charges accumulated on each plates separately after the electric field is applied. Both charges attract to each other but they can never come together due to the presence of dielectric.

The attraction between positive and negative charges creates an electric field between them. This electric field holds them on the conducting plates. There is a point at where the plate cannot hold anymore charges, indicating that it has stored charges to the maximum. This maximum of charge can be stored is termed as ‘capacitance’. On the other hand, the charge a capacitor is holding during the charging process is determined by the potential difference between the conducting plates.

$$Q = C \times V \quad 2.2$$

where Q is the charge stored in a capacitor (in unit of coulomb) and V (in unit of volt) is the potential difference between the conducting plates.

Equation 2.2 depicts the relationship between charge stored Q , capacitance C , and potential difference V . Since the capacitance C is a constant value, we can decide the charge stored in a capacitor by adjusting the potential applied on it. From this equation, we can deduce the meaning of ‘farad’. One farad refers to the capacitance of a capacitor achieved when it stores one coulomb of charge at one volt of potential applied. Conventional capacitor is rated in picofarad to microfarad range (10^{-12} to 10^{-6}). When the capacitance measured falls in the range from farad to kilofarad, the component is more appropriate to be called as ‘supercapacitor’ or ‘ultracapacitor’.

This is the basic principle behind a capacitor. Next, the brief history and development of supercapacitor will be explored. This is followed by the energy storage principles of supercapacitor which lead to the division between electric double layer capacitor (EDLC) and pseudocapacitor. Next, the electrode materials, electrolyte and the preparation methods of electrode are reviewed. Since the electrolyte for a supercapacitor is not the main concern on this work, it will only be briefly explained. The literature survey will emphasise on the electrode material since it is related to the energy storage, which is also the primary focus of this work.

2.2 Brief history and development of supercapacitor

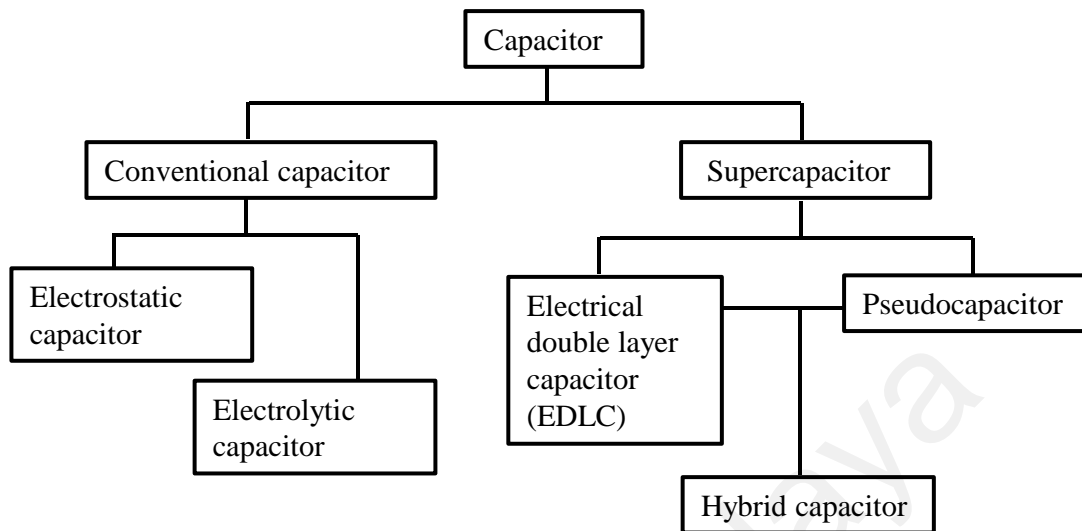


Figure 2.2: Family of capacitor.

The concept of storing electrical energy in the electric double layer formed at solid/electrolyte interface has been realised since the late of 1800s. In the early of 1950, General Electric engineers were working on the porous carbon as the electrode for capacitor. It was not until 1957 that Becker built the first electrical device using the concept of double layer (Becker, 1957). He was impressed by the high capacitance value achieved. However, this device was found impractical that both electrodes needed to be immersed in an electrolyte container. In 1966, Rightmire from Standard Oil Company of Ohio (SOHIO) had subsequently designed and patented a practical electrical device which is feasible to date. It was followed by the invention of an electrolytic capacitor with activated carbon electrodes patented by Boos in 1970. This technology has developed and assembled into present electrochemical capacitor technology.

The failure of SOHIO in commercialising the electrochemical capacitor technology opened an opportunity to Nippon Electric Company (NEC) of Japan who had successfully obtained the second licence after SOHIO and marketed the “supercapacitor”

(Miller, 2007). After licensing the technology of supercapacitor, NEC had rapidly developed and led the technology for many years. They introduced FA series in 1978, FG series, FT series and FC series in 1990s.

After that, the knowledge about supercapacitor has been greatly expanded through the studies made by Conway. In 1999, he devised the term of “supercapacitor” after made tremendous efforts in studying ruthenium oxide electrochemical capacitor. Conway showed that the increased capacitance in supercapacitor is contributed by the surface redox reactions. He explained that the total capacitance of a supercapacitor is provided by the partial electrical charge stored in Helmholtz double layer and also the “pseudocapacitance” resulted from the charge transfer reactions took place between electrode and electrolyte. Conway also described the working mechanisms of pseudocapacitor as redox reactions, intercalation, and underpotential adsorption. In 1993, Dr Alexander Ivanov introduced a large electrochemical capacitor, named as ECOND ‘PsCap’, which could store a large amount of charge (Deshpande, 2015). His presentation showed that large capacitors were used to start 3000 horsepower diesel locomotive engines. His achievement indicated a significant step for capacitor development.

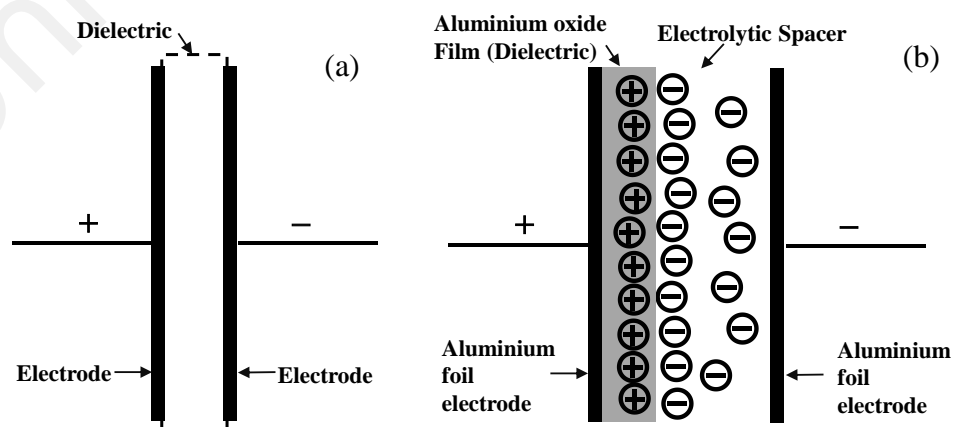


Figure 2.3: Configuration of (a) electrostatic capacitor and (b) aluminium electrolytic capacitor.

In overall, capacitor technology has evolved from electrostatic capacitor to supercapacitor nowadays. **Figure 2.2** shows the general categories of capacitor. Electrostatic capacitor stores charge in the most literal way, that is, accumulates and holds electrical charges inside the electric field between the conductive electrodes (**Figure 2.3 (a)**). The conductive electrodes are separated by a dielectric material or an insulator. The operating voltage of an electrostatic capacitor relies on the strength of the dielectric material. Electrostatic capacitor can offer capacitance less than $10 \mu\text{F g}^{-1}$ and energy density not more than 0.1 W h kg^{-1} (Zhao et al., 2011).

Electrolytic capacitor has similar cell construction with electrostatic capacitor. The difference lies in the presence of conductive electrolyte spacer in an electrolytic capacitor (Sharma & Bhatti, 2010). The capacitance of an electrolytic capacitor is dependent on electrolyte inside the cell. Typically, it can achieve above $1 \mu\text{F}$. This allows it to be applicable in the power supply and digital circuit. There are two types of electrolytic capacitor, determined by the materials used: one is aluminium electrolytic capacitor (**Figure 2.3 (b)**) and second one is tantalum electrolytic capacitor.

Supercapacitor also known as ultracapacitor and electrochemical capacitor. Although the names are coined by different manufacturers, they refer to the same product. The name of 'supercapacitor', which will be used throughout this thesis, was firstly utilised on EC product by NEC. It can be divided into two groups based on charge storage mechanisms, which will be discussed in the following section. The supercapacitor has grew from fractions of farads up to hundred farads. This technology still have long way to go for technical promises. Intense works have been carried out in order to improve the performance of a supercapacitor, as a stand-alone device or a component used complementary with batteries.

2.3 Energy storage principles of supercapacitor

2.3.1 Electric double layer capacitor (EDLC)

Electric double layer capacitor (EDLC) is one type of supercapacitor in which its performance mainly relies on the double layer capacitance. Although it stores charge in a similar way as a conventional capacitor, an EDLC can nevertheless store significantly more charge compared to a conventional capacitor.

The concept of double layer was firstly described by Helmholtz in year 1853. He applied the double layer concept on colloidal suspension by immersing the charged electrodes into an electrolytic solution. The model explains the charged electrodes repelled the co-ions while attracted counter ions of the charge on the electrode. This study is then extended to the surface of metal electrodes. The same phenomenon is observed, that is the electrolyte ions with same charge of charged metal electrode are repelled while ions with opposite charge are attracted to the surface of electrode. This gives rise to the formation of double layer with distance of d . It consists of two layers of opposite charges and locates at the interface between electrode and electrolyte, as depicted in **Figure 2.4 (a)**. Helmholtz model proposed that the integral and differential capacity are identical and constant in value (Srinivasan, 2006). However, this model was found contradict with the experimental result which showed the differential capacity varied with potential. This observation has been taken into account by Louis Georges Gouy and David Chapman, who then formed Gouy-Chapman (G-C) model, **Figure 2.4 (b)** (Chapman, 1913; Gouy, 1910).

By considering the thermal motion of electrolyte ions, G-C model introduces diffuse model of double layer using Maxwell-Boltzmann distribution. This model also reveals the effects of applied potential and the nature of the electrolyte on the differential capacity. On the other hand, G-C model assumes the electrolyte ion as a point charge

and can adsorb limitlessly onto the layer extended from electrode surface. This leads to the infinitely increase in differential capacity with applied potential, which is in fact violated to the experimental data.

Helmholtz model was good to represent the interface between electrode and electrolyte with the condition of very high electrolyte concentration, while G-C model could best describe the high dilution limit (Madou, 2011). By combining Helmholtz model and G-C model, Otto Stern had proposed Stern model (**Figure 2.4 (c)**) (Stern, 1924). This model takes the finite size of an electrolyte ion into account and considers the presence of two electrolyte ions distribution regions. A so-called ‘Stern layer’, a compact layer of ions formed adjacent to the electrode surface and they are confined by outer Helmholtz plane (OHP). Outside this layer, the electrolyte ions are dispersed in electrolyte, as explained in G-C model.

Stern model was further developed by three groups, Esin and Markov, Grahame and Devanathan, that led to the introduction of Grahame model (Grahame, 1947). This model includes a layer consists of dehydrated ions which can specifically adsorbed to the electrode surface closer than the OHP. This layer is named as inner Helmholtz plane (IHP). Thus, there are three regions in Grahame model. Both IHP and OHP are narrow and only in the range of atomic dimension. The diffusion layer is further extended outside OHP.

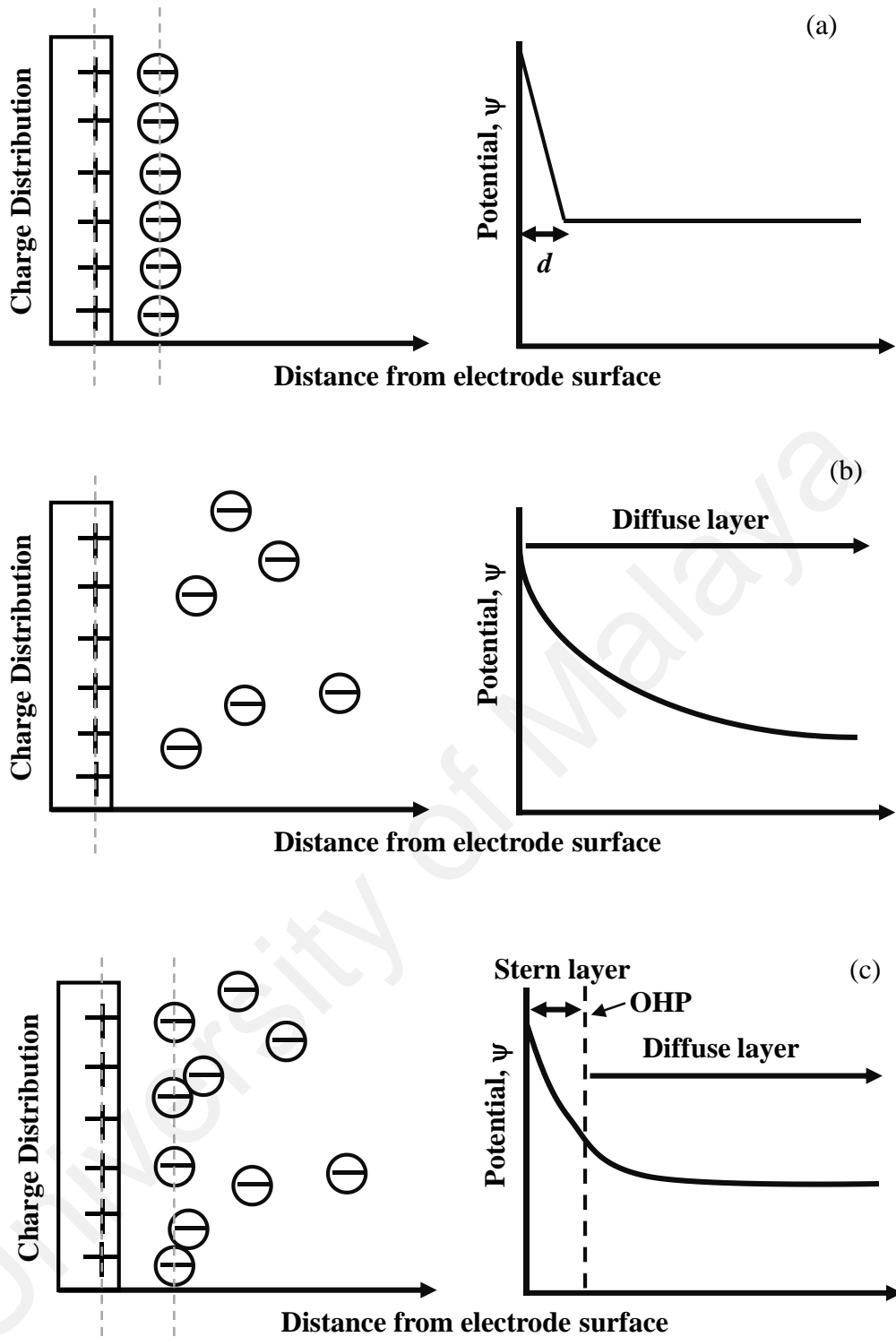


Figure 2.4: Models of the double layer: (a) Helmholtz model, (b) Gouy-Chapman (G-C) model, (c) Stern model and (d) Bockris, Devanathan, Müller (BDM) model.

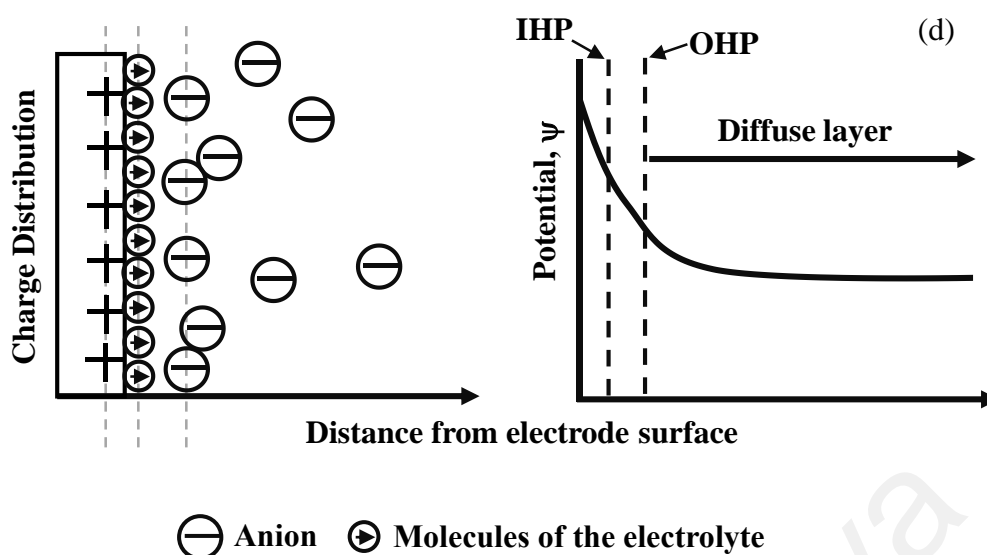


Figure 2.4: Continued.

The specific adsorption is the result of interactions between charged electrode and ions such as electric field forces, dispersion forces and image forces (Srinivasan, 2006). In electrochemistry, the aqueous media are always involved. There are solvents with polar character which can cause the potential drop across the interface between charged electrode and electrolyte. Besides, solvent concentration is non-negligible since it is always higher than solute concentration. John Bockris, Devanathan, and Alexander Müller have identified the role of solvent in the electrolyte. Thus, they covered the participation of solvent molecules at the interface, and proposed Bockris, Devanathan, Müller (BDM) model (**Figure 2.4 (d)**) (Bockris, 1963). In this model, the strong interaction between solvent molecule and charged electrode can cause the fixed alignment of solvent molecules attached to the electrode surface. These solvent molecules formed the first layer inside the IHP and oriented strongly to the electric field depending on the charge. Together with specifically adsorbed ions, small amount of partially solvated ions appear to be the minority in the IHP. However, solvated ions will be outside the IHP. On the other hand, the region extend from OHP remains to be a diffuse zone of ions. As a matter of fact, BDM model has become the most commonly used model nowadays.

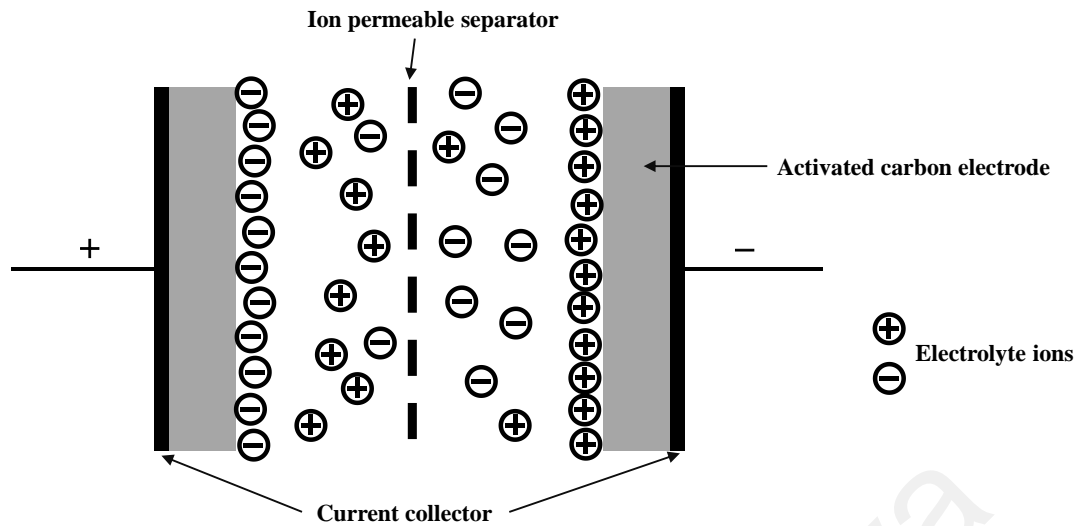


Figure 2.5: Configuration of electric double layer capacitor (EDLC).

EDLC is the third generation evolution of capacitor after conventional capacitor and electrolytic capacitor. It uses carbon as the main electrode material along with either organic or aqueous electrolyte. A basic configuration of EDLC is displayed in **Figure 2.5**. In EDLC, each electrode/electrolyte interface acts like a capacitor. So, the complete cell can be considered as two capacitors in series. The cell capacitance (C_{cell}) for a symmetrical capacitor, with C_1 and C_2 represent capacitances of first and second electrode, is therefore can be expressed as in **Equation 2.3**. On the other hand, the double layer capacitance, C_{dl} , of single electrode is expressed as **Equation 2.4**.

$$C_{cell} = \frac{1}{C_1} + \frac{1}{C_2} \quad (2.3)$$

$$C_{dl} = \frac{\varepsilon A}{4\pi T} \quad (2.4)$$

where ε is the dielectric constant, A (in unit of squared meter) is the surface area of the electrode and T (in unit of meter) is the thickness of double layer.

EDLC's dependence on electrostatic interaction for charge storage enabling it to sustain hundreds or thousands cycles for charging and discharging. In reality, a capacitor encounters internal resistance caused by the electrode, current collector and

dielectric. By considering this factor, a voltage drop is introduced and the resistances are designated as equivalent series resistance (R_{ESR}). Thus, the maximum electrical power (P), which is the maximum rate of energy transfer, can be determined (Equation 2.5).

$$P_{max} = \frac{V^2}{4R_{ESR}} \quad (2.5)$$

2.3.2 Pseudocapacitor

Previous studies about EDLC using carbon electrode had discovered the participation of pseudocapacitance in the charge storage processes. The contribution of pseudocapacitance to the total capacitance is small but significant. It is believed to be caused by the partial charge transfer reactions during chemisorption processes.

In general, pseudocapacitance arises when the reversible redox reactions take place at the interface between electrode and electrolyte (Augustyn et al., 2014). It can also occur when the redox reactions are not restrained by solid state ion diffusions, which lead to the occurrence of reactions near the surface of the electrode. The pseudocapacitive electrode material exhibits similar electrochemical signature as a capacitive electrode (Brousse et al., 2015). In other words, the charge stored in a pseudocapacitive electrode material responds linearly to the potential applied. The main difference between pseudocapacitance and double layer capacitance lies in the charge storage mechanism, that is, the charge storage originates from the electron transfer reactions for pseudocapacitance while double layer capacitance depends on the pure accumulation of electrolyte ions on the electrode surface. The term of ‘pseudocapacitive’ is more appropriate to be used to describe a single electrode material rather than a system (Brousse et al., 2015). This is because we cannot speculate the processes occurred inside a system solely based on the macroscopic behaviour it showed (such as

the galvanostatic charge-discharge behaviour). For system contains electrode materials with both kind of Faradaic and non-Faradaic nature, it is more suitable to be described as 'hybrid system' as the resulted electrochemical performance is contributed by both materials. .

Pseudocapacitance is different from the double layer capacitance that, it is the result of Faradaic processes which involve the electron transfer across the interface between electrode and electrolyte while double layer capacitance is electrostatic in nature (Conway et al., 1997). There are three kinds of pseudocapacitive mechanisms: underpotential deposition, redox pseudocapacitance and intercalation pseudocapacitance (Conway, 1999). Underpotential deposition refers to the formation of monolayer resulted by the adsorption of metal ions on the metal electrode's surface. Redox pseudocapacitance is the product of electrochemical adsorption with charge transfer. Intercalation pseudocapacitance refers to the capacitance contributed by the Faradaic charge transfer reactions took place along with the intercalation of ions into layers or tunnels of a redox active material without crystallographic phase change.

Pseudocapacitive materials can be considered as either intrinsic or extrinsic, yet both of them display the characteristic of capacitive charge storage. As a result of phase transformation during ion storage, extrinsic pseudocapacitive material such as MoO_2 does not display characteristics of capacitive charge storage in bulk state (Kim et al., 2015). The pseudocapacitance is most likely to show when the material is nanostructured. On the contrary, intrinsic pseudocapacitive materials such as MnO_2 and $\text{RuO}_2 \cdot n\text{H}_2\text{O}$ exhibit pseudocapacitive behaviour in a wide range of particle sizes (Ardizzone et al., 1990; Toupin et al., 2004; Zheng et al., 1995).

2.4 Electrode materials for supercapacitor

2.4.1 Carbon

Carbon is one of the most abundant element on Earth. The atoms of carbon can bond in different manners, thus produce different forms of carbon, namely allotropes. There are three well-known crystalline allotropes of carbon: graphite, diamond and fullerenes. They exist as solid under normal conditions. Under normal pressure, carbon presents in graphite form. Hence, graphite is the most thermodynamic stable form of carbon. Graphite is layered and planar in structure. The planes inside, namely graphene sheets, are stacked and loosely bounded by Van der Waals forces with the distance of 0.335 nm. The carbon atoms are arranged in a honeycomb lattice with separation of 0.142 nm in the layer (Delhaès, 2000). The stacking faults give rise to the weak disorder in graphite, leading to the small increase of the interlayer distance. This causes the planes to be uncorrelated with their neighbours and thus each plane has a main finite size.

At very high pressure, carbon will appear as diamond. Diamond has a tetrahedral structure: each carbon atom is surrounded by four other carbon atoms at the corner of a tetrahedron. Compared to graphite which is 2-dimensional in network, diamond has 3-dimensional network with strong covalent sp^3 bonds. A fullerene has an icosahedral structure, with 20 hexagonal and 12 pentagonal rings as the basis. The carbon atoms are bonded to three others. Fullerene is found to present in different forms such as spherical, tube and ellipsoid. Spherical fullerene is called 'Buckminsterfullerene' or 'Bucky ball' while cylindrical fullerene is named carbon nanotube.

Most of the carbon materials obtained through carbonisation process. It is a derivation process using carbon-rich precursors under heat treatment in an inert atmosphere. The heat treatment is called pyrolysis. Carbonisation is important to remove non-carbon elements. Different precursors and processing conditions will

produce crystallites with different sizes and orientations (Pandolfo & Hollenkamp, 2006). The product remained after carbonization, charring and pyrolysis is called char (Rodríguez-Reinoso & Molina-Sabio, 1992). In general, char is relatively low in porosity. It is made up by elementary crystallites with interstices between them. Inside the interstices, there consists of carbon residues which is lacking of organisation that can block the pores. Thus, activation process is employed. This process involves gasification of char using carbon dioxide or steam. It increases the surface area and porosity of char through various carbon precursor and activation conditions. This results in different materials and most of them can be generally referred as activated carbon (AC). AC is the most common electrode material used in commercial EDLC. It is a non-graphitisable carbon. This means that the carbon precursors of AC undergo carbonisation in solid-phase. The most general precursors used for AC production are lignocellulose and coal-based materials.

When the carbon precursors experience high temperature treatment, the macromolecular system decomposes. The decomposition occurs along with the evolution of gases and liquids of low molecular weight. The remaining carbon atoms move in shorter distance within the macromolecular system to gain stability. Thus, the product preserves the structure of precursor but with lower bulk density. During the process of evolution of heteroatoms, shifting of carbon atoms and co-bonding of carbon atoms, the voids are generated and so the porosity is introduced (Marsh & Reinoso, 2006b).

Liquid-phase carbonisation occurs in certain precursors such as graphite and other graphitisable carbons. They become viscous fluid before carbonisation process. The molecular carbons fused during carbonisation and formed ordered structure without porosity (Marsh & Reinoso, 2006a).

Carbons can be found in the form of powder, fibres and woven cloths with specific surface area of about $3000 \text{ m}^2 \text{ g}^{-1}$ (Lokhande et al., 2011). Although carbon behaves predominantly capacitive in charge storage, there is still pseudocapacitance present which is contributed by the surface functional groups on activated carbon. The functional groups participate in the charge-discharge processes and provide pseudocapacitance.

2.4.2 Graphene

Graphene is a 2-dimensional material with single atomic layer of carbon network at where the carbon atoms are bonded by sp^2 -bonding, **Figure 2.6** (Geim & Novoselov, 2007). It offers excellent electronic, thermal and mechanical properties. Thus, graphene is expected to be applied in many technological fields such as supercapacitor, battery and solar cell. The graphene can be synthesised using various approaches such as microwave assisted method, chemical/mechanical exfoliation and sonication (Choucair et al., 2009; Vadukumpully et al., 2009; Wang et al., 2009; Xu et al., 2011). The chemical reduction process from graphite flakes is another technique to produce graphene-like material. This kind of materials is more appropriate to be designated as 'reduced graphene oxide' because it contains defect resulted from the oxidation and reduction processes. The low cost and scalable graphite oxide is always used to prepare reduced graphene oxide for supercapacitor electrodes.

The conventional Hummer's method can be employed to produce reduced graphene oxide from graphite. The steps are basically started by preparing the acid intercalation that causes the oxidation of graphitic flakes, followed by physical agitation to exfoliate the sheets (Allen et al., 2010). The Hummer's method has been modified by many researches in order to increase the quality and quantity of reduced graphene oxide effectively (Chen et al., 2015; Chen et al., 2013; Huang et al., 2011). Hydrazine was

once the highly used reducing agent for the graphene oxide. However, it is hazardous in nature. Hence, greener reducing agents such as sodium nitrate and sodium carbonate are studied (Chen et al., 2013; Jin et al., 2013). The reduced graphene oxide prepared using sodium carbonate exhibited 228 F g^{-1} indicating a green and effective chemical reduction of graphene oxide is achievable.

The key challenge for large scale production of graphene is the aggregation of graphene sheets caused by the Van der Waals interactions during the synthesis process. Since the unique properties of graphene are related to the graphene sheets, the aggregation of graphene sheets is of particular important to get rid of.

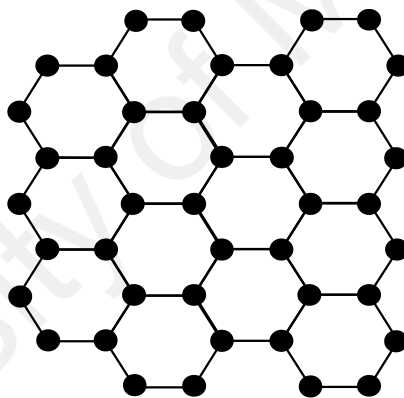


Figure 2.6: Hexagonal lattice of graphene.

Compositing with other materials has been shown to be a good way to overcome the aggregation problems. The composites with metal oxide normally exhibit the morphology of particles anchoring on the reduced graphene oxide sheets (Song et al., 2016; Xu et al., 2016a). The studies have illustrated the effectiveness of preventing aggregations of reduced graphene oxide sheets and also agglomerations of particles. Some composites such as $\text{Ni(OH)}_2\text{-RGO}$ and $\text{ZnCo}_2\text{O}_4\text{-RGO}$ displayed silk-like morphology indicating the graphene oxide flakes are remained after the process (Wang et al., 2016; Zang et al., 2017).

2.4.3 Transition metal oxides

2.4.3.1 Ruthenium oxide

Ruthenium oxide (RuO_2) is the most well-known transition metal oxide to be studied for its pseudocapacitive properties. It is a promising electrode material which possesses high value of electrochemical capacitance, in both crystalline and amorphous hydrous form (Cornell & Simonsson, 1993).

Before the pseudocapacitive properties being discovered, it was mainly studied as chlorine and oxygen evolving anodes due to its electrocatalytic properties (Burke & Healy, 1981; Burke & McCarthy, 1984; Burke & Murphy, 1980; Melsheimer & Ziegler, 1988; Trasatti, 1987). It is not until 1971, the cyclic voltammogram of a RuO_2 film was found similar to the one of carbon-based EDLCs (Trasatti & Buzzanca, 1971). This has motivated the efforts to investigate the pseudocapacitance mechanism of RuO_2 .

At 1995, a high specific capacitance of 720 F g^{-1} achieved by the hydrous ruthenium oxide was reported (Zheng & Jow, 1995). The value was at least two times higher than the highest reported value at that time. They believed the high value of specific capacitance is contributed by the hydrous region within the nanoparticles (Zheng et al., 1995). Besides, they also proposed another three contributions for high specific capacitance achieved: (i) electron hopping between electrode material and current collector, (ii) electron hopping between particles and (iii) electron hopping within $\text{RuO}_x \cdot n\text{H}_2\text{O}$. Since then, $\text{RuO}_2 \cdot x\text{H}_2\text{O}$ has become one of the most promising electrode material for supercapacitor application.

Table 2.1: Literature review on RuO₂-based electrode.

Preparation method	Film properties	Specific capacitance	Reference
Hydrothermal	Hydrous RuO ₂ with MWCNT	1585 F g ⁻¹	(Chaitra et al., 2016)
Facile template method	Hydrous RuO ₂ nanotubes	745 F g ⁻¹	(Wu et al., 2015)
Cathodic deposition	RuO ₂ -CNT with ripple-like morphology	272 mF cm ⁻²	(Wang et al., 2015)
Microwave-hydrothermal	One dimensional RuO ₂ ·1.84H ₂ O	511 F g ⁻¹	(Kim et al., 2015)
Laser scribing method	Graphene-RuO ₂ nanocomposite	1139 F g ⁻¹	(Hwang et al., 2015)
Hydrothermal	RuO ₂ -graphene	528 F g ⁻¹	(Leng et al., 2015)
Solution phase assembly	RuO ₂ -graphene	479 F g ⁻¹	(Deng et al., 2014)
Successive ionic layer adsorption and reaction (SILAR)	PANI-RuO ₂ with nanoparticles grown on nanofibers	664 F g ⁻¹	(Deshmukh et al., 2014)
Hydrothermal	RuO ₂ -reduced graphene oxide (RGO)	521 F g ⁻¹	(Shen et al., 2013)
Electropolymerisation and redox deposition	Nanoscopic RuO ₂ -PANI-carbon double shelled hollow spheres	531 F g ⁻¹	(Zhao et al., 2012)
Inkjet printing	Single-walled carbon nanotube/RuO ₂ nanowire	138 F g ⁻¹	(Chen et al., 2010)
Sol-gel and low temperature annealing	Hydrous RuO ₂ /graphene with particle-attached layered structure	570 F g ⁻¹	(Wu et al., 2010)
Sacrificial template method	Tubular RuO _x ·nH ₂ O	860 F g ⁻¹	(Zhang et al., 2010)
Anodic deposition	Porous RuO ₂	276 F g ⁻¹	(Mondal & Munichandraiah, 2008)
Chemical bath deposition	RuO ₂ thin film	50 F g ⁻¹	(Patake & Lokhande, 2008)

Table 2.1 shows the preparations and electrochemical performances of the RuO₂-based electrodes. RuO₂ was synthesised using different techniques including hydrothermal, laser scribing, sol-gel and deposition. RuO₂ film can be easily produced using deposition method (Mondal & Munichandraiah, 2008; Patake & Lokhande, 2008). The RuO₂ film produced through chemical bath deposition formed a smooth structure while a porous structure was grown when the anodic deposition method was applied. The porous structure was caused by the oxygen evolution during anodic deposition. It is essential for ionic transportation. Hence, the RuO₂ film prepared using anodic deposition would be performed electrochemically better compared to the one synthesised using chemical bath deposition method. On the other hand, a tubular structure of RuO₂ governed by the manganese oxide nanorod which acted as morphology sacrificial template has been found to exhibit higher specific capacitance (860 F g⁻¹) compared with porous RuO₂ (Zhang et al., 2010). This may be caused by the higher active surface area offered by the tubular structure.

RuO₂ is well known for its high cost. However, this does not prohibit researchers from studying further about it. In order to reduce its effective cost, RuO₂ has been combined with other materials such as MWCNT, CNT, graphene and PANI. Carbon materials can act as backbone for RuO₂ particles and offer the conducting pathway for electrolyte ion. For example, the aggregated RuO₂ nanoparticles were found distributed well on the MWCNT. The uniform distribution can be attributed to the oxygen functionalities grown during the functionalisation of MWCNT (Chaitra et al., 2016). The enhanced specific capacitance from 604 to 1585 F g⁻¹ was believed to be contributed by easier penetration of ions through hollow structure of MWCNT compared with RuO₂ itself. On the other hand, the cathodically deposited CNT on 3D silicone microstructure presented ripple-like morphology (Wang et al., 2015). The RuO₂ nanoparticles have

coated well on CNT and hindered the detachment of CNT from the substrate. This porous network was strong in binding and successfully improved the ionic conductivity.

Graphene, as a carbon material that has good conductivity (2000 S cm^{-1}), is another material that is widely studied as composite with RuO_2 . Laser scribing method has been employed to synthesize RuO_2 -graphene (Hwang et al., 2015). The RuO_2 nanoparticles were dispersed well on graphene sheet. The uniform dispersion of RuO_2 on graphene allows the more efficient ionic and electronic transportations. This highly porous graphene with RuO_2 nanoparticles composite has demonstrated a high specific capacitance of 1139 F g^{-1} . The Van der Waals attractions between graphene sheets that can bring to restacking is a challenge to overcome when the graphene is employed. Hence, an optimizing condition is required to prepare RuO_2 -graphene composite. Sodium hydroxide (NaOH) was found to be a better precipitant compared with ammonium carbonate ($(\text{NH}_4)_3\text{CO}_2$) and carbamide or urea ($\text{Co}(\text{NH}_2)_2$) when the hydrothermal method was used (Leng et al., 2015). Different precipitants can result in various morphologies. For instance, $(\text{NH}_4)_3\text{CO}_2$ has led to the formation of an inhomogeneous structure with less pores while $\text{Co}(\text{NH}_2)_2$ produced more homogenous structure with spherical particles. On the other hand, NaOH formed a veil-like morphology. The electrochemical test has shown the better performance of RuO_2 -graphene composite produced with the aid of NaOH , at where the specific capacitance achieved was 528 F g^{-1} . Although the RuO_2 -graphene formed without precipitant also exhibited veil-like morphology, its specific capacitance was only 358 F g^{-1} . This shows the importance of a suitable precipitant for hydrothermal method.

Conducting polymer is another material that can be incorporated with RuO_2 . For example, RuO_2 -PANI composite can be fabricated using successive ionic layer adsorption and reaction (SILAR) (Deshmukh et al., 2014). The RuO_2 nanoparticles were

grown on the PANI nanofibers. The combination of RuO₂ with PANI has led to the production of more porous structure and thus higher active surface area. In order to enhance the backbone for electron transportation, carbon material is again a good candidate to integrate with RuO₂-PANI. A double-shelled carbon sphere could combine first with PANI to form a strong foundation for RuO₂ (Zhao et al., 2012). However, the specific capacitance achieved was only 531 F g⁻¹. It is lower compared with the RuO₂-PANI prepared using SILAR method, which is 664 F g⁻¹. The difference can be attributed to the morphologies formed between them. The RuO₂-PANI was observed to have a more porous structure. It is well-known that higher porosity can optimise the ionic and electronic transportations. Thus, there is no doubt that RuO₂-PANI could achieve higher specific capacitance with its higher porosity structure. From here, the morphology is shown to be a determining factor for the electrochemical performance.

A composite electrode prepared using repetitive impregnations procedure has achieved 1000 F g⁻¹ of specific capacitance (Barranco et al., 2009). It consisted of a ruthenium oxide deposited-amorphous carbon nanofibers structure. The composite electrode showed high porosity of 450 m² g⁻¹. The amorphous carbon nanofibers acted as the backbone for ruthenium oxide and so for charge storage. The repetitive impregnation method has been compared with impregnation technique involved Ru(acac)₃ vapour (Pico et al., 2009). The relationship between the particle size of RuO₂·xH₂O and the pore size of carbon support was also investigated. The repetitive impregnations of carbon with RuCl₃·0.5H₂O was found to produce particles with less crystallinity. In other words, the electrode prepared using this method could achieve higher specific capacitance. Another finding of them revealed the smaller size of particles compared with the pore size of carbon support could lead to higher specific capacitance.

Instead of focusing only on the fabrication of RuO₂-based composite due to its high electrochemical performance, researchers have found alternative transition metal oxide to replace RuO₂·xH₂O.

2.4.3.2 Manganese oxide

Due to its relatively low cost and low toxicity compared with a ruthenium oxide, manganese oxide turns out to be a good replacement for ruthenium oxide. The manganese (Mn) is abundant in nature and appears in the form of ore and native metallic nodules. As the neighbour of iron (Fe) in periodic table, the chemical and physical properties of Mn are found similar to Fe's.

As a transition metal oxide, manganese oxide has seven oxidation states: Mn(0), Mn(II), Mn(III), Mn(IV), Mn(V), Mn(VI) and Mn(VII) (Messaoudi et al., 2001). Similar to ruthenium oxide, the water content in manganese oxide is involved in electrochemical reactivity and thermodynamic stability of each manganese oxide phases (Desai et al., 1985; Lee et al., 1999). The theoretical capacity of MnO₂ is about 1100 C g⁻¹ based on Faraday's law (Pang et al., 2000). In other words, the theoretical specific capacitance of MnO₂ is around 1100 F g⁻¹ in a potential window of 1 V. However, most of the reported specific capacitances of MnO₂ are still far less than the theoretical value. Intense studies have been carried out in order to further enhance the specific capacitance. The common determinant factors for the specific capacitance of manganese oxide film are: (a) proton transportation through the lattice, (b) conductivity and (c) microstructure of the film. Since the water content/proton is vital in charge storage mechanism for manganese oxide film, it is usually prepared using sol-gel method. There are other techniques can be employed to produce manganese oxide film and they are displayed in **Table 2.2**. The manganese oxide film prepared using sol-gel method exhibited porous structure in general. The film is amorphous in nature but

crystallinity can be grown by increasing annealing temperature. The morphology of manganese oxide film can be easily transformed from rod-like structure to cubic-like structure of Mn_3O_4 after annealed at 300 °C (Davis et al., 2011). However, the grain growth upon annealing has decreased the surface area. This can affect the total active area for charge storage. This is clearly shown when the manganese oxide experienced higher annealing temperature. The increase in crystallinity is more noticeable at higher annealing temperature. The transformation of MnO_2 to Mn_3O_4 and then Mn_2O_3 is always obtained when the annealing temperature exceeded 300 °C (Lin et al., 2007; Nagarajan et al., 2006). Nonetheless, the more amorphous manganese oxide film has achieved higher specific capacitance compared to those annealed at higher temperature (Lin et al., 2007; Sarkar et al., 2015). In order to enhance the electrochemical performance of manganese oxide film, the combination with other materials is always a good technique. The addition of meso-carbon microbeads (MCMB) into manganese oxide film was found to be a good way. Compared with the manganese oxide film without MCMB (209 F g^{-1}), the film added with MCMB has obtained higher specific capacitance (350 F g^{-1}) significantly. This enhancement in charge storage performance can be attributed to the higher interfacial surface area offered by MCMB particles (Chen et al., 2009).

Apart from sol-gel method, there are other methods for preparation of manganese oxide-based films. We can also have different technique to fabricate a similar material. For example, layered double hydroxide (LDH), an anionic clay represented by the formula $[\text{M}^{2+}_{1-x} \text{M}^{3+}_x (\text{OH})_2]^{x+} \text{A}^{z-}_{x/z} \cdot m\text{H}_2\text{O}$ where M^{2+} is a divalent cation, M^{3+} is a trivalent cation and A^{z-} serves as any organic or inorganic anion (Cavani et al., 1991). It can be prepared using simple electrodeposition method or urea hydrolysis. Both LDHs showed high specific capacitances in the range of 1000 F g^{-1} . However, different morphologies were obtained due to different preparation method. Electrodeposited

CoMn-LDH appeared as hexagonal platelets-like morphology while NiMn-LDH synthesised using urea hydrolysis method showed nanosheets structure (Guo et al., 2016; Jagadale et al., 2016). Their cycling stabilities were excellent as well. CoMn-LDH retained around 65 % after 5000 cycles while NiMn-LDH preserved more than 90 % after 3000 cycles. The similarity between these two LDHs is the employment of nickel foam as the substrate. The nickel foam is well-known for its good mechanical strength which offers a strong support for LDH formed. Besides nickel foam, gold substrate especially nanoporous gold substrate also acts as a good substrate. The manganese oxide film deposited on the nanoporous gold substrate was grown with porous and aggregated nanosheets structure (Shi et al., 2017). The film deposited at the same current density but using gold substrate was observed to have continuous structure with equiaxed particles. The nanoporous gold substrate has contributed to the electrochemical performance of the manganese oxide film by providing a higher specific surface area than gold substrate, hence higher specific capacitance was expected for former substrate.

Aside from the substrate, the morphology formed also can be governed by the addition of different materials. The introduction of nickel has transformed a rod-like structure into a plate-like structure and thus declined the particle size (Wu et al., 2012). The composite comprised of cobalt and manganese oxide showed a 3-dimensional network with nanoscale fibers while manganese oxide-graphene exhibited a nanoparticle-sheet structure (Chang et al., 2008; Lee et al., 2015). The application of conductive backbone for manganese oxide-based film is found can accomplish the charge storage mechanism by improving the electronic conductivity. The conductive backbones that has been widely studied and reported are MWCNT, graphene and carbon nanofiber (Chen et al., 2016; Hong et al., 2014; Unnikrishnan et al., 2016).

The ternary composite is another widely studied material. An excellent electrochemical performance (2525 F g^{-1}) has been achieved by $\text{Co}_3\text{O}_4\text{-MnO}_2\text{-NiO}$ ternary hybrid nanotubes (Singh et al., 2016). It can be attributed to the well-aligned arrays of nanotubes formed which eases the penetration of electrolyte ions. On the other hand, $\text{Ni(OH)}_2/\text{MnO}_2/\text{RGO}$ prepared using hydrothermal method also exhibited 1985 F g^{-1} of specific capacitance (Chen et al., 2014). The charge storage was facilitated by the porous flower-like structure formed.

University of Malaya

Table 2.2: Literature review on manganese oxide-based electrode.

Preparation method	Film properties	Specific capacitance	Reference
Anodic deposition	Manganese oxide nanostructure grown on nanoporous gold film	432 F g ⁻¹	(Shi et al., 2017)
Electrodeposition	Co ₃ O ₄ -MnO ₂ -NiO nanotubes	2525 F g ⁻¹	(Singh et al., 2016)
Spray pyrolysis	Mn ₃ O ₄ thin film	394 F g ⁻¹	(Yadav et al., 2016)
Urea hydrolysis	Nickel-manganese layered double hydroxide	1511 F g ⁻¹	(Guo et al., 2016)
Electrodeposition	Cobalt-manganese layered double hydroxide	1062 F g ⁻¹	(Jagadale et al., 2016)
Sacrificial reaction	Manganese oxide decorated graphene nanosheets	280 F g ⁻¹	(Unnikrishnan et al., 2016)
Anodic deposition	Mn-Ni oxide	250 F g ⁻¹	(Tahmasebi et al., 2016)
Sol-gel method	Manganese oxide/multiwalled carbon nanotubes (MWCNT)	339 F g ⁻¹	(Chen et al., 2016)
Sol-gel method	Manganese oxide film	360 F g ⁻¹	(Sarkar et al., 2015)
Hydrothermal	Mn ₃ O ₄ -graphene	367 F g ⁻¹	(Lee et al., 2015)
Hydrothermal	Ni(OH) ₂ -MnO ₂ -RGO	1985 F g ⁻¹	(Chen et al., 2014)
Electrospinning	Carbon nanofiber-MnO ₂ core-shell tubular structure	237 F g ⁻¹	(Hong et al., 2014)
Electrospinning	Carbon nanofiber-MnO ₂	311 F g ⁻¹	(Zhi et al., 2012)
Hydrothermal	Nickel-manganese oxide	284 F g ⁻¹	(Wu et al., 2012)
Cathodic deposition	Manganese oxide thin film	365 F g ⁻¹	(Liu et al., 2010)

2.4.3.3 Nickel oxide

Due to its environmental friendliness and natural abundance, nickel oxide is one of the potential electrode materials to be used in supercapacitor. Nickel oxide has multiple oxidation states which favour fast redox reactions and thus can contribute in charge storage processes. Nickel oxide has been widely studied as electrode material for other applications such as battery, fuel cell, gas sensors and electrochromic films (Mamak et al., 2001; Michalak et al., 1999; Poizot et al., 2000; Wang et al., 2015). Although nickel oxide has a high theoretical specific capacitance (3750 F g^{-1}), it is poor in electronic conductivity. It cannot sustain in the repetitive charge-discharge processes because it experiences volume expansion that can destruct the active materials and damage the electrical contact (Zhuo et al., 2013).

Table 2.3 shows some finding of past studies for nickel oxide-based electrode. Even without the additional material, nickel oxide was found to exhibit high specific capacitance of 1337 F g^{-1} (Pei et al., 2016). Solvent was realised to be important in determining the nickel oxide morphology and electrochemical performance. The introduction of ethanol into the deionized water has changed the morphology of nickel oxide gradually. The nanoflakes structure became more fragmented with the higher volume ratio of ethanol to water.

The nickel foam and carbon cloth are always employed as substrate nowadays due to their high electrical conductivity and strong mechanical property. The nickel oxide prepared on nickel foam using hydrothermal method showed specific capacitance of 674 F g^{-1} (Huang et al., 2014). On the other hand, the carbon cloth supported nickel oxide synthesized using chemical bath deposition method displayed 660 F g^{-1} (Zhang et al., 2014). Both nickel oxide films also exhibited high cycling stability. Nickel oxide on nickel foam retained around 93 % after 5000 cycles while the one

deposited on carbon cloth has successfully kept 82 % from its initial capacitance after 4000 cycles. The morphologies formed between them are similar: nanosheets or nanoflakes. Hence, the slight difference in electrochemical performance may attribute to the substrate used.

Chemical bath deposition can also be used to prepare nickel oxide-based composite. For example, nickel-cobalt oxyhydroxide on carbon nanotubes ((Ni, Co) OOH/CNT) has been successfully synthesized using this method (Li et al., 2015). Compared with the electrode consisted only nickel oxide, this electrode exhibited a good specific capacitance of 940 F g^{-1} , which is higher than the carbon cloth-supported nickel oxide prepared using same method (660 F g^{-1}). This (Ni, Co) OOH-CNT possessed a unique core-shell structure. The (Ni, Co) OOH nanoflakes are densely attached on the carbon nanotubes. This special structure allows the easy penetration of electrolyte ions thus lead to a relatively higher specific capacitance.

By using simple electrodeposition technique, a good specific capacitance of 950 F g^{-1} can be achieved (Zhao et al., 2016). The high specific capacitance is contributed by the morphology formed and the substrate used is nickel foam. Graphene acts as the strong binder between nickel oxide and nickel foam that avoids the exfoliation of nickel oxide from substrate. Without additional material, the electrochemical performance of a nickel oxide that is directly electrodeposited on substrate is found to be inferior. For example, the nickel oxide deposited on carbon nanofoam only shows 150 F g^{-1} (Della Noce et al., 2016). The additional material is shown not only acting as the binder, but also guide the formation of a desired morphology.

Other than chemical bath deposition, hydrothermal, and electrodeposition, the solvothermal is also a good method for electrode preparation. $\text{Ni}(\text{OH})_2$ -RGO composite prepared using solvothermal method exhibited 1886 F g^{-1} (Zang et al., 2017). The

composite has an interconnected porous structure. When PANI was added into nickel oxide-graphene composite, the surface of composite was covered uniformly by PANI without changing the morphology significantly (Wu et al., 2016).

Binary oxide of NiCo_2O_4 has been reported with its excellent electrochemical performance and thus receives worldwide attention. It can be prepared using simple technique such as co-precipitation or hydrolysis process. NiCo_2O_4 -graphene oxide composite fabricated using co-precipitation method exhibited 1211 F g^{-1} (Xu et al., 2016c). With the aid of sodium dodecyl sulfate (SDS), the morphology of NiCo_2O_4 -graphene oxide transformed from mesoporous structure to flower-like structure. On the other hand, NiCo_2O_4 -SWCNT prepared using controlled hydrolysis method showed specific capacitance of 1642 F g^{-1} (Wang et al., 2012). The water: ethanol ratio was adjusted in order to find out the best composition of solvent for NiCo_2O_4 -SWCNT electrode. Different water/ethanol ratio led to different morphologies formed. The water: ethanol ratio of 1: 4 was found out to be the optimal condition to produce the electrode with better electrochemical performance. The well separated nanowires structure formed is believed to contribute in the charge transfer reactions.

Table 2.3: Literature review on nickel oxide-based electrode.

Preparation method	Film properties	Specific capacitance	Reference
Solvothermal	Ni(OH) ₂ -RGO	1886 F g ⁻¹	(Zang et al., 2017)
Hydrothermal and <i>in situ</i> chemical oxidative polymerization	Nickel oxide coated graphene-PANI	1409 F g ⁻¹	(Wu et al., 2016)
Microwave	Nitrogen-doped mesoporous carbon-nickel cobalt layered double hydroxide	2498 F g ⁻¹	(Xu et al., 2016b)
Co-precipitation	Nickel cobalt oxide-graphene oxide	1211 F g ⁻¹	(Xu et al., 2016c)
Hydrothermal	NiO nanomaterial	1337 F g ⁻¹	(Pei et al., 2016)
Electrodeposition	NiO-RGO	950 F g ⁻¹	(Zhao et al., 2016)
Anodic deposition	NiO _x on carbon nanofoam	150 F g ⁻¹	(Della Noce et al., 2016)
Alternating voltage approach	Nickel oxide quantum dots embedded with graphene	1181 F g ⁻¹	(Jing et al., 2015)
Chemical bath deposition	Nickel-cobalt oxyhydroxide/oxide on carbon nanotubes	940 F g ⁻¹	(Li et al., 2015)
Chemical bath deposition	NiO nanoflake/carbon cloth	660 F g ⁻¹	(Zhang et al., 2014)
Hydrothermal	NiO nanosheets on Ni foam	674 F g ⁻¹	(Huang et al., 2014)
Electrodeposition	Manganese-nickel oxide film on graphite sheet	424 F g ⁻¹	(Lee et al., 2014)
Electrodeposition	Nickel-cobalt hydroxide coated on NiCo ₂ O ₄	2.17 F cm ⁻²	(Huang et al., 2013)
Controlled hydrolysis process	NiCo ₂ O ₄ -single wall carbon nanotubes (SWCNT)	1642 F g ⁻¹	(Wang et al., 2012)
Chemical precipitation method	Porous nickel oxide-mesoporous carbon	2570 F g ⁻¹	(Zhang et al., 2010)

2.4.4 PEDOT: PSS (Conducting polymer)

Conducting polymer is a subset of organic polymer that shows conducting or semiconducting properties. Its conductivity is offered by the Π electron delocalisation along the polymer backbone in its conjugated bond system. In other words, polymer has alternating single and double bond allowing the electron to freely move from one end to another. This provides a unique optical and electrical properties for the polymer.

Polymer was once considered as electrically insulating material. In 1963, B. Bolto et al. had found out that the behaviour of polymer similar to semiconductor when they studied about the electronic properties of polypyrrole (Bolto et al., 1963). Only until 1977, the semiconducting properties of polymer was finally revealed through the doping process which occurred accidentally (Shirakawa et al., 1977). It is now known that, the process of doping has converted the insulating polymer into an ionic complex. This ionic complex is composed of a polymeric cation (or anion) and a counterion. The counterion can be the oxidised form of a reducing agent, or the reduced form of an oxidising agent. The usage of a reducing agent is known as n -type doping, while that of an oxidising agent is referred as p -type doping. The charging processes during the n - and p -type doping are shown as **Equation 2.6** and **Equation 2.7** (Snook et al., 2011).



In general, the synthesis of polymer starts with the polymerisation of monomer to form oligomer which is low in molecular weight. Next, the oligomer goes through oxidation at potentials lower than the monomer's oxidation potential to produce polymer. Typically, there are two approaches to synthesise conducting polymer, namely chemical polymerisation and electrochemical polymerisation. Chemical polymerisation

involves chemical oxidants such as ferric chloride, ferric nitrate and ammonium persulfate during the oxidation process (Frackowiak et al., 2006; Jurewicz et al., 2001; Lee et al., 2011). The resulted conducting polymers show high conductivity and good stability in aqueous solution (Peng et al., 2008). In the case of electrochemical polymerisation, it is always carried out in three-electrode configuration that consists of working, counter and reference electrodes. The monomer solution acts as the electrolyte. A potential applied at the working electrode allowing the oxidation to occur and the resulted polymer will be electrodeposited on the electrode (Gurunathan et al., 1999; Peng et al., 2007).

Due to its wide conductivity range and flexibility, conducting polymer turns out to be a potential electrode material for energy storage system. Polyaniline, polypyrrole and derivatives of polythiophene are the most widely studied conducting polymers as the electrode materials for supercapacitor (Frackowiak et al., 2006; Khomenko et al., 2005; Lota et al., 2004). Conducting polymer undergoes fast redox reactions in the bulk of the material to provide capacitive response and charge storage. The advantages possessed by conducting polymer are sufficient to counteract its drawback, which is the low rate of charge-discharge. The low rate of charge-discharge is caused by the slow diffusion of ions within the bulk of conducting polymer. However, conducting polymer-based electrodes can be modified and designed into desired nanostructures for maximum capacity uptake. This has led to the intense studies on the nanostructured conducting polymer (Shi et al., 2015; Yin & Zheng, 2012).

Poly (3, 4-ethylenedioxythiophene)-poly (styrenesulfonate) (PEDOT: PSS) is a water soluble conducting polymer and can disperse nanomaterials in water (Hou et al., 2010). It contains a conducting polythiophene derivative that is bound to a PSS polyanion electrostatically. Hence, PEDOT: PSS has high stability, high flexibility and high

electrical conductivity. A uniform and well-connected PEDOT: PSS film can be easily prepared using spin coating technique (Cheng et al., 2016). Besides, spray deposition integrated with secondary doping treatment also could produce a high quality of PEDOT: PSS film (Higgins & Coleman, 2015).

Due to its high conductivity, PEDOT: PSS can be combined with metal oxides such as manganese oxide in order to overcome their poor conductivity. PEDOT: PSS-MnO₂ composite electrode prepared using freeze drying method showed structure with interconnected macropores and exhibited 1068 F g⁻¹ (Ranjusha et al., 2014). Without manganese oxide, PEDOT: PSS film was revealed as a smooth surface. The addition of manganese oxide increased the roughness of the film. However, the sponginess was lost when the amount of manganese oxide exceeded 10 wt. %. Hence, an optimal amount of manganese oxide needs to be considered in order to produce a PEDOT: PSS-manganese oxide film. Other than manganese oxide, nickel oxide and cobalt oxide are also potential metal oxides to be combined with PEDOT: PSS. A ternary oxide of manganese, nickel and cobalt was found to have poor conductivity although the electrochemical performance was improved. Compositing this ternary oxide with PEDOT: PSS was proven to increase the conductivity (Yin et al., 2016). This composite electrode exhibited a good specific capacitance of 1234 F g⁻¹ which is higher than the manganese-nickel-cobalt ternary oxide (638 F g⁻¹) prepared using hydrothermal method (Li et al., 2014).

Another common material to be combined with PEDOT: PSS is carbon material for example reduced graphene oxide, multi-walled carbon nanotubes (MWCNT) and single-walled carbon nanotubes (SWCNT). A RGO-PEDOT: PSS film presented high flexibility and conductivity. It can be bent and rolled while maintaining its electrochemical performance (Liu et al., 2015). The addition of PEDOT: PSS has

prevented the restacking of graphene sheets and thus increased the active surface area. A composite consisted of MWCNT and PEDOT: PSS prepared using 'dip and dry' technique possessed a structure of PEDOT: PSS wrapped on the MWCNT (Karade & Sankapal, 2016). This structure retained the mesoporous network of MWCNT and increased the surface area at the same time. Another PEDOT: PSS-MWCNT composite fabricated directly from electrochemical polymerization showed a 3-dimensional porous microstructure (Zhou et al., 2015). The bundles of MWCNT were found to be encapsulated by the PEDOT: PSS and formed the porous structure. On the other hand, the PEDOT: PSS-SWCNT composite also displayed a similar morphology although different methods were employed (Antiohos et al., 2011).

University of Malaya

Table 2.4: Literature review on PEDOT: PSS-based electrode.

Preparation method	Film properties	Specific capacitance	Reference
Dip coating and electrodeposition	Ag-doped PEDOT: PSS/PANI	643 F g ⁻¹	(Patil et al., 2016)
Spin coating	PEDOT: PSS film	28 F g ⁻¹	(Cheng et al., 2016)
Solvothermal	Ni-Mn-Co ternary oxide-PEDOT: PSS	1234 F g ⁻¹	(Yin et al., 2016)
Dip and dry coating technique	PEDOT: PSS encapsulated MWCNT	235 F g ⁻¹	(Karade & Sankapal, 2016)
Spin coating and vapour phase polymerization	PEDOT: PSS-MnO ₂ -PEDOT	391 F cm ⁻³	(Chen et al., 2016)
Reflux	PEDOT: PSS-NiFe ₂ O ₄ -RGO	1090 F g ⁻¹	(Hareesh et al., 2016)
Bar-coating method	RGO-PEDOT: PSS	448 mF cm ⁻²	(Liu et al., 2015)
Screen printing	RuO ₂ -PEDOT: PSS/RGO	820 F g ⁻¹	(Cho et al., 2015)
Spray deposited	PEDOT: PSS film	41 F cm ⁻³	(Higgins & Coleman, 2015)
Electrochemical polymerization	MWCNT-PEDOT: PSS	98 mF cm ⁻²	(Zhou et al., 2015)
Hydrothermal and heating	MnO ₂ -RGO-PEDOT: PSS	169 F g ⁻¹	(Yan et al., 2014)
Freeze drying	MnO ₂ embedded PEDOT: PSS	1068 F g ⁻¹	(Ranjusha et al., 2014)
Sonication and heating	PEDOT: PSS-SWCNT	133 F g ⁻¹	(Antiohos et al., 2011)

From the studies above, we realised the preparation methods applied are usually hydrothermal although there are many other ways to be employed. In early days, researchers adopted conventional method for electrode preparation. This method involves the mixing of active material, binder (such as carbon black, nafion and PVDF) and additives with an organic solvent to form a slurry. The slurry is then coated on a current collector followed by a heat treatment. However, this method can bring about the electrical contact resistance between current collector and electrode material. Consequently, electronic and ionic transportation are hindered. In order to minimise the contact resistance, electrode materials are more likely to be synthesised directly onto the substrate nowadays. This can result in better electrochemical performance and therefore higher specific capacitance.

In this study, electrodeposition method is applied throughout the experiments. The details of electrodeposition technique will be discussed in Section 2.6.

2.5 Electrolyte

As one part of a supercapacitor, the electrolyte located inside the separator or in between active material, also play an important role in electrochemical performance. There are certain requirements for an electrolyte to be used in supercapacitor system such as high electrochemical stability, wide potential window and low resistivity (Wang et al., 2012). In general, there are three types of electrolyte can be used in supercapacitor: aqueous electrolyte, organic electrolyte, and ionic liquids.

Typically, aqueous electrolyte offers higher capacitance for the supercapacitor compared with the organic electrolyte because the former has a higher ionic concentration. For metal oxide-based electrode, since the participation of electrolyte cations other than proton is noticed during the charge storage process, the choice for electrolyte has expanded into the usage of mild electrolyte from the concentrated H_2SO_4

(Lee et al., 1999). One of the advantages of using aqueous electrolyte is that, it can be prepared and used easily without any special treatments or conditions. However, aqueous electrolyte has a narrow potential window. Due to the decomposition potential of water (1.23 V) and some kinetic factors, the practical upper operating voltage of aqueous electrolyte is about 1.4 V (Conway et al., 1997). Although the operating voltage of organic electrolyte is higher (3.5 V or more), the low conductivity affects the power performance of a supercapacitor (Conway, 1999). Examples of organic electrolytes are propylene carbonate (PC) and acetonitrile. Compared with acetonitrile, PC is more environmental benign.

Ionic liquid (IL) is a molten salt. More accurately, it refers to the salt that melts below 100 °C (Ohno & Fukumoto, 2008). For those melt at room temperature, it is more appropriate to be called as 'room temperature ionic liquids'. Ionic liquid has unique properties for instance non-flammability, high chemical stability and low vapour pressure. The properties of ionic liquid are strongly relied on the type of anion and cation. Among the ionic liquids, imidazolium, pyrrolidinium and aliphatic quaternary ammonium salts are the most widely studied IL for supercapacitor application (Mousavi et al., 2016; Sato et al., 2004). ILs offer a wide potential window. For instance, a mixture of N-methyl-N-propylpiperidinium bis(fluorosulfonyl)imide (PIP₁₃-FSI) and N-butyl-N-methylpyrrolidinium bis(fluorosulfonyl)imide (PYR₁₄-FSI) provide wide potential window up to 3.5 V (Tsai et al., 2013). However, a wide potential window does not promise a higher specific capacitance. In a study comparing the electrochemical performances of the reduced graphene oxide in aqueous and IL-based electrolytes, it has exhibited higher specific capacitance in H₂SO₄ (348 F g⁻¹) compared with the value of 158 F g⁻¹ achieved in 1-butyl-3-methylimidazolium hexafluorophosphate (BMIPF₆) (Chen et al., 2011). Nevertheless, wider potential window recommends higher power and energy density. For example, although the

smaller anion of BF_4^- in BMIBF_4 provided better ionic transportation, its lower potential window of 3 V has limited its power density when it was compared with BMIPF_6 which has 4 V of potential window (Chen et al., 2012). However, the toxicity and the flammability of ILs when they are used near heat sources are still the challenges for commercialization (Fox et al., 2008; Liaw et al., 2012).

2.6 Electrodeposition

Electrochemical deposition, or electrodeposition for short, is the production of film resulted from the oxidation/reduction of dissolved species in a solution. As this technique allows the synthesis of a metal oxide, alloy, and nanostructured material with good control in thickness, it has been widely employed in industry for coating purpose.

At standard conditions of pressure, temperature and concentration the oxidation and reduction rates are equal. This brings about the standard electrode potential. The electrode potential E can be related to the standard electrode potential through the Nernst equation (**Equation 2.8**):

$$E = E^0 + \frac{RT}{nF} \ln \frac{[Ox]}{[red]} \quad (2.8)$$

where R = standard gas constant ($\sim 8.31 \text{ J K}^{-1} \text{ mol}^{-1}$),

T = absolute temperature (K),

n = number of electrons transferred,

F = Faraday constant, $9.648 \times 10^4 \text{ C mol}^{-1}$.

When the electrode potential is made relatively more negative to the standard reduction potential, the rate of electron transfer of the reduction process increases thus leads to the increases in the reduction current.

2.6.1 General principle of electrodeposition

Faraday's Law of electrolysis is the basic of electrodeposition which relates time, current flow and equivalent weight of the metal with the weight of deposit. It allows us to estimate the weight deposited on a working electrode since the weight of deposit is proportional to the number of moles of electrons transferred while $I \cdot t$ represents the total charge required for the process. **Equation 2.9** shows the relationship between all related parameters:

$$W = \frac{I t E_q}{F} \quad (2.9)$$

where W = weight of deposit (g)

I = current flow (A)

t = time (s)

E_q = equivalent weight of deposit

F = Faraday constant, $9.648 \times 10^4 \text{ C mol}^{-1}$.

In general, the principle of electrodeposition is simple. It is originated from the oxidation or reduction of the species in a solution. When the reduction occurs, the consumption of active species at the working electrode induces the formation of concentration gradient outside the electrode surface. The random movement of ions down a concentration gradient in order to equalise the concentration difference is termed as diffusion. If the solution is left unstirred, the diffusion layer will extend into the solution. As a result, thermal and vibration movement can participate the mass transfer processes. It is then can be deduced that, the current is limited either by the kinetics of the electrode reactions or by the mass transfer of species towards the electrode surface. The electron transfer reaction can be simplified as $O + ne^- = R$ where 'O' represents the reactant in the electrolyte while 'R' indicates the product after

reactions. Before the current is applied, there is an initial potential (open circuit potential). The concentration of 'O' at the electrode surface is the same as in the bulk of the electrolyte. Once the reducing current applied causes the reduction of 'O' to 'R', the surface concentration of 'O' starts to decrease and thus results in the gradient of concentration between the electrode surface and bulk electrolyte. More 'O' diffuses from bulk electrolyte to the electrode surface in order to maintain the applied current until the surface concentration of 'O' is depleted. Since the applied current can no longer be supported by this electron transfer reaction, the potential changes to another redox potential for next electron transfer reaction.

2.7 Summary

- This chapter starts with the basis of a capacitor from general principles to important related variables such as capacitance, potential difference and charge.
- The history and development of capacitor from electrolytic capacitor to supercapacitor are presented. The supercapacitor is classified into two groups based on two different charge storage mechanisms: electric double layer capacitor (EDLC) and pseudocapacitor. EDLC depends on the electrostatic interaction between charges for storage purpose while pseudocapacitor relies on the redox reactions or charge transfer reactions.
- The evolution of double layer concept is presented. From early Helmholtz model, the concept of double layer has been slowly developed through Gouy-Chapman model, Stern model, Grahame model and Bockris, Devanathan, Müller (BDM) model.

- This chapter is then continued with the detailed introduction of pseudocapacitor. The difference between EDLC and pseudocapacitor is shown.
- As the determinant factor for specific capacitance, the electrode materials studied for supercapacitor application are introduced. The carbon material is the main electrode material for an EDLC while transition metal oxide or conducting polymer is employed in a pseudocapacitor. The combination of carbon material with either transition metal oxide or conducting polymer leads to the formation of a hybrid capacitor.
- Since this thesis mainly focus on transition metal oxide-based electrode materials, several types of transition metal oxides (ruthenium oxide, manganese oxide and nickel oxide) are reviewed. Besides, the graphene, as the carbon material along with PEDOT: PSS as the conducting polymer are reviewed as well.
- As one part of a supercapacitor, the electrolytes such as organic, aqueous and ionic liquid are explained in brief.
- The general principle of electrodeposition is introduced briefly in the last section.

The next chapter will elaborate the general application of electrodeposition and the preparations of three electrodes with different combinations of materials. The fabricated electrodes are examined by field emission scanning electron microscopy (FESEM), transmission electron microscopy (TEM) and X-ray diffraction (XRD). The electrochemical performance of the electrode is characterised cyclic voltammetry (CV), galvanostatic charge-discharge (GCD) and frequency response analysis (FRA).

CHAPTER 3: EXPERIMENTAL METHOD

3.1 Introduction

There are three main sections in this chapter. The first one is about some details of electrodeposition, which is the technique employed for electrode preparation throughout the thesis. After that, materials used will be presented followed by the preparation of the composite electrodes. Once the composite electrodes is prepared, they will be subjected to few characterisations. The details about each characterisation techniques will be evaluated in the third section.

The occurrence of electrodeposition in an aqueous solution relies on the oxidation or reduction of the active species inside a solution. The electrodeposition can happen in either oxidizing condition or reducing condition in the solution depending on the composition of deposition electrolyte. For electrodeposition of metal oxide, it is mostly carried out in an alkaline solution with metal complexes inside.

Generally, there are two kinds of electrodeposition techniques: constant potential and constant current. Constant potential technique controls the potential of the working electrode while the current is the measured parameter. On the other hand, the constant current technique measures the potential of the working electrode while controlling the current flows. The advantage of using constant current technique is that, the ohmic drop, which is the product of current and solution resistance, remains constant. Hence, it can be corrected by a constant potential offset. Chronopotentiometry is one of the constant current techniques. It has been applied to investigate the adsorption behaviour of electroactive species on the electrode surface in the early days (Anson, 1961; Herman & Bard, 1963). In chronopotentiometry, the current steps from zero to some finite values instantaneously. The measured potential is changed due to the ohmic drop once the current is applied. In addition, the solution is unstirred throughout the experiment.

The advantages of using electrodeposition technique are: (a) it can be carried out at low temperature and atmospheric pressure, (b) it does not produce side product, (c) the experimental setup is simple and (d) the film properties can be controlled by varying the experimental conditions such as concentration of the deposition electrolyte, applied electrical conditions and solvent.

3.2 Composite electrode preparation

In general, all composite electrodes were prepared using electrodeposition method. The electrodeposition was carried out using chronopotentiometry technique with a constant current density (2 mA cm^{-2}) in two-electrode configurations. This current density is chosen because higher current density at 3 mA cm^{-2} and above can cause over oxidation of manganese ions while the stabilizing current density is found occurred around 1 mA cm^{-2} (Shinomiya et al., 2006). The stainless steel and carbon rod were acted as working electrode and counter electrode respectively. The electrodeposition duration was the variable parameter. The weight of the deposited composite film was estimated using CPA Analytical Balance CPA225D. On the other hand, the post-heating temperatures were different for each composite electrode systems. The details were specified accordingly in the following section.

3.2.1 Reduced graphite oxide-manganese oxide

The reduced graphite oxide was prepared using simplified Hummer's method (Huang et al., 2011). Since the detailed explanation was shown in the literature, we only demonstrated procedures here. Firstly, 3 g of graphite flakes is added into a solution consisted of 360 mL of H_2SO_4 and 40 mL of H_3PO_4 . After the colour of solution changed to black, 18 g of KMnO_4 was added gradually. This solution was left stirring for 3 days. The solution was noticed to be appeared in dark brown after 3 days. 30 % H_2O_2 was added into the solution until the colour of solution changed to light

yellow. Then, the stirring was stopped and the solution was left for one day. After settled down, the solution was centrifuged at 7000 rpm in order to separate out the excess acid. The second stage of centrifugation was carried out with the addition of HCl at 7000 rpm. At last, the solution was centrifuged with deionised water at 11500 rpm. The product here is termed as graphite oxide. The graphite oxide was then reduced using L-ascorbic acid as evaluated in other literature (Zhang et al., 2010). The final product was mixed with 0.01 M $\text{Mn}(\text{CH}_3\text{COO})_2 \cdot 4\text{H}_2\text{O}$ and acted as electrolyte for electrodeposition.

The electrodeposition durations studied for reduced graphite oxide-manganese oxide composite electrode were: 10, 13, 15 and 18 mins. The samples for this system were designated as 'RM' and this name was used throughout the thesis. The names for each electrodes were tabulated in **Table 3.1**. The electrodes were rinsed with distilled water and heated at 100 °C for 3 hours before undergo any characterisations.

Table 3.1: Name of samples in reduced graphite oxide-manganese oxide composite electrode system.

Electrodeposition duration, t / mins	Name of sample
10	RM 10
13	RM 13
15	RM 15
18	RM 18

3.2.2 Manganese-nickel oxide

The electrolyte for electrodeposition of second system, which is manganese-nickel oxide composite electrode was composed of 0.01 M $\text{Mn}(\text{CH}_3\text{COO})_2 \cdot 4\text{H}_2\text{O}$, 0.25 M $\text{Ni}(\text{CH}_3\text{COO})_2 \cdot 4\text{H}_2\text{O}$ and 0.8 M H_2SO_4 . The electrodeposition duration was varied to be 10, 13, 15 and 18 mins. The details of the name given for this system are given in **Table 3.2**. After the as-prepared electrode was rinsed with distilled water, it was heated at 300 °C for 6 hours.

Table 3.2: Designation of samples for manganese-nickel oxide composite electrode system.

Electrodeposition duration, t / mins	Name of sample
10	MN 10
13	MN 13
15	MN 15
18	MN 18

3.2.3 Manganese oxide-PEDOT: PSS

The electrodeposition was carried out in an electrolyte consisted of 0.01 M Mn (CH₃COO)₂·4H₂O and 1 mL PEDOT: PSS. The deposited film in this system was found weak in adhesion for longer electrodeposition duration such as 10 mins. Hence, the electrodeposition was achieved in a relatively shorter duration compared with former two composite electrode systems. The electrodeposition durations for this system were 10, 20, 30, 40, and 50 seconds. The electrode was rinsed with distilled water followed by post-heating at 60 °C for 1 hour. The description of samples for this system was given in **Table 3.3**.

Table 3.3: Sample names for manganese oxide-PEDOT: PSS composite electrode system.

Electrodeposition duration, t / s	Name of sample
10	MP 10
20	MP 20
30	MP 30
40	MP 40
50	MP 50

3.3 List of chemicals and materials

Materials and chemicals utilised for electrode preparations were mentioned concisely in the previous sections. In **Table 3.4**, the details of manufacturer and specification for each chemicals are shown.

Table 3.4: Information of chemicals and materials in the experiment.

Chemical/ Material	Manufacturer	Details
Graphite flakes	Nippon Graphite Industries, Ltd	Model: CB-100
Potassium permanganate	Bendosen	Assay: min. 99 %
L-ascorbic acid	UNILAB	Assay: min. 99 %
Sulphuric acid	Friendemann Schmidt	95–97 %
Ortho-Phosphoric acid	Friendemann Schmidt	Grade: AR Assay (acidimetric): min 85 %
Hydrogen peroxide	Friendemann Schmidt	Grade: AR Assay (permanganometric): min. 30 %
Hydrochloric acid	UNIVAR	Assay: 36 % w/w min
Manganese (II) acetate tetrahydrate	Fluka	Assay: ≥ 99.0 % (KT)
Nickel (II) acetate tetrahydrate	Fluka	Assay: ≥ 99.0 % (KT)
Poly (3, 4-ethylenedioxythiophene): polystyrenesulfonate	Sigma-Aldrich	High-conductivity grade 1.1 % in H ₂ O

3.4 Characterisations

3.4.1 Field emission scanning electron microscopy (FESEM)

Field emission scanning electron microscopy (FESEM) is used to visualise the topographical and elemental information of a sample. It allows us to examine the structure of material in nanometer scale resolution. FESEM was utilised to observe the morphology of the composite electrode in this thesis.

The FESEM instrument used was Jeol JSM-7600F field emission scanning electron microscopy. A High Power Optics irradiation system is adopted to carry out high accuracy, high resolution and high speed of elemental analysis. The composite electrode was cut into desired size to fit the specimen stub. The morphology of composite electrode was observed under different magnifications such as 50k, 100k and 200k.

3.4.2 Transmission electron microscopy (TEM)

The working principle of a transmission electron microscopy (TEM) is similar to a light microscope. Instead of light, TEM makes use of electron during the inspection on microstructure of material. Due to the much smaller wavelength of electron compared with light, the optimal resolution achievable by a TEM is better than a light microscope. In other words, TEM is able to uncover the finest details of microstructure.

The TEM instrument used was Jeol-2100F transmission electron microscopy. The composite film was scraped from the substrate (stainless steel). In order to make the scrap thinner, it was taken for sonication. It is important to remember that, TEM sample must be thin enough in order to transmit adequate electrons for image formation with minimum energy loss. TEM measurement was carried out in different magnifications for example 5k, 20k and 40k.

3.4.3 X-ray diffraction (XRD)

X-ray diffraction (XRD) is a non-destructive analytical method to inspect material properties such as structure, phase composition and texture. In this work, it is used to detect the changes in properties of the composite electrode with various electrodeposition durations. Since different post-heating temperature is applied for each composite electrode, the impact of post-heating temperature on the structure of material can be identified.

The XRD instrument used in this work was D8-advance X-ray diffraction XRD Bruker AXS with monochromatised radiation of CuK_α . The operating voltage and current were 40 kV and 40 mA respectively. Due to the strong reflection peaks of stainless steel, the composite film was scraped from the stainless steel for XRD measurement in this work. The scrape-off film did not receive any extra treatment

before the measurement. The XRD result was displayed in the plot of scattered intensity versus Bragg angle 2θ . The measurement was recorded from 2θ of 5° to 80° .

3.4.4 Electrochemical tests

3.4.4.1 Cyclic voltammetry (CV)

Cyclic voltammetry (CV) is an electroanalytical technique employed to investigate the electrochemical reactions. It allows us to observe the redox behaviour in a given potential range. At the same time, it provides information about the kinetics of heterogeneous electron transfer reactions and adsorption processes.

CV contains an electrolytic cell, a current-to-voltage converter, a potentiostat and a data acquisition system. The electrolytic cell is made up of working electrode, counter electrode and reference electrode. The potential applied on the working electrode is varied linearly with time, with the assistance from reference electrode in maintaining the potential to be constant. The electricity from the signal source is conducted between counter electrode and working electrode.

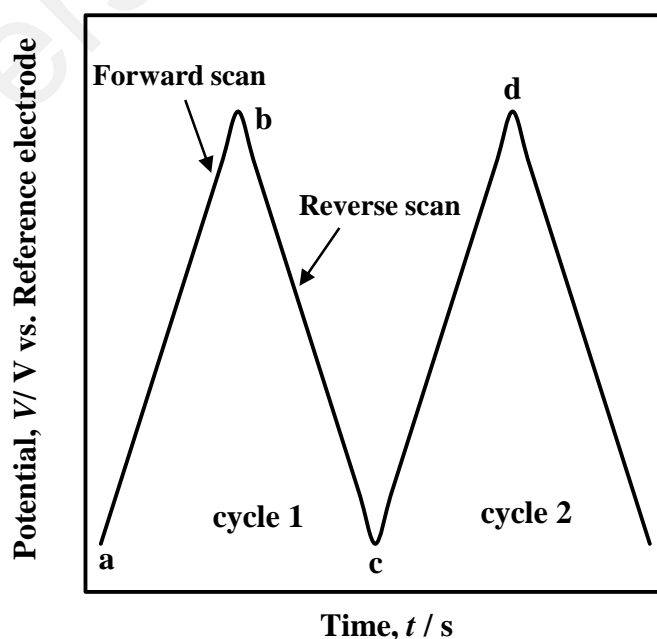


Figure 3.1: Excitation signal of CV.

In CV, a potential is applied on the working electrode, which is immersed in an unstirred electrolyte, and the current response is measured. In order to maintain a constant potential, the potential of the working electrode is measured against a reference electrode such as Ag/AgCl reference electrode and saturated calomel electrode (SCE). This gives rise to an excitation signal as shown in **Figure 3.1**. During the forward scan, the potential starts at a given potential value and ends at another desired potential value. The potential extrema b is called the switching potential. This is where the potential is adequate for oxidation or reduction to occur. The reverse scan starts from b to c . This cycle is repeatable with various scan rates. The scan rate is given by the slope of the excitation signal (Kissinger & Heineman, 1983).

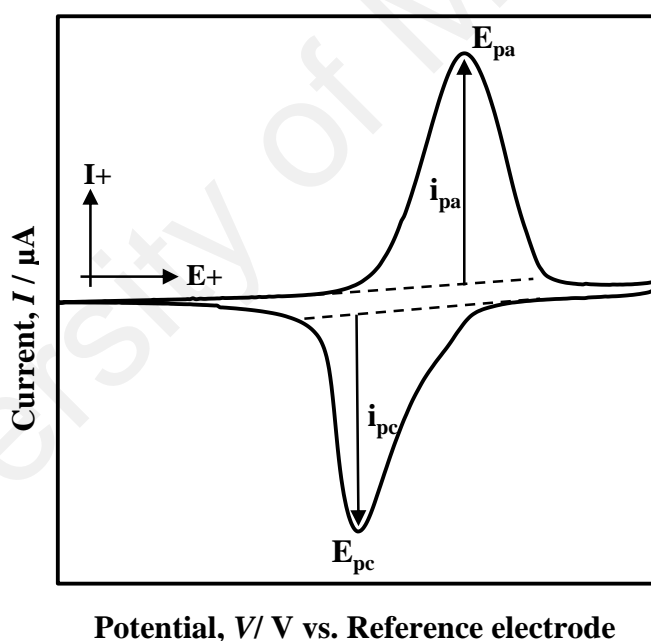


Figure 3.2: A typical cyclic voltammogram.

The result is in the form of cycle between potential and current, with potential on x -axis while current response on y -axis. The general form of cyclic voltammogram is shown **Figure 3.2**. The important parameters for CV are anodic peak potential E_{pa} , anodic peak current i_{pa} , cathodic peak potential E_{pc} and cathodic peak current i_{pc} . The peak potentials, E_{pa} and E_{pc} can be directly read from the voltammogram. For estimation

of peak current values, i_{pa} and i_{pc} , an extrapolation of the baseline current is needed as shown in **Figure 3.2**.

The voltammetric charge integrated from the positive and negative sweep of cyclic voltammetry curve is directly related to the electroactive sites of redox reactions. This can be used to estimate the specific capacitance (C_{sp}) of the electrode, as shown in **Equation 3.1**, with Q as the voltammetric charge, v is the scan rate and m is the mass loading of composite film.

$$C_{sp} = \frac{Q}{v \cdot m} \quad (3.1)$$

$$C_{sp} = \frac{I}{v \cdot m} \quad (3.2)$$

The asymmetrical shape of cyclic voltammetry curve has to be taken into consideration that the sum of anodic and cathodic voltammetric charges are replaced by the integral area of cyclic voltammetry curve I , as shown in **Equation 3.2**.

In this work, the CV measurement is carried out in a three-electrode configuration, where the composite electrode acted as the working electrode, platinum, and Ag/AgCl electrode are used to serve as the counter electrode and reference electrode respectively. Different scan rates (1, 5, 10, 15 and 20 mV s^{-1}) are applying on the system and the corresponding electrochemical behaviour is studied.

3.4.4.2 Galvanostatic charge-discharge (GCD)

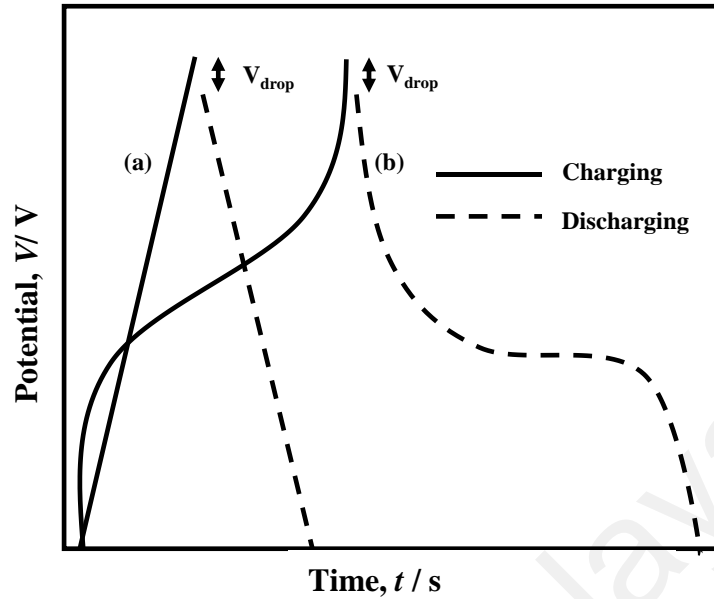


Figure 3.3: GCD plots of (a) EDLC and (b) pseudocapacitive materials.

Galvanostatic charge-discharge (GCD) is a standard technique used to test the performances of the energy storage devices such as battery and supercapacitor. In industry field, it is mainly applied for cycle stability test. The measurement is carried out at constant current until a desired voltage is reached. A repeating loop of charging and discharging is called a cycle. **Figure 3.3** displays the GCD plots of EDLC and pseudocapacitive materials. EDLC shows linearity during charge-discharge while pseudocapacitive material exhibits non-linearity due to the redox reactions. In the beginning of discharging process, there is a voltage drop caused by the internal resistance of the device. It can be expressed as in **Equation 3.3**.

$$R = \frac{V_{drop}}{i} \quad (3.3)$$

The specific capacitance C_{GCD} can be estimated using discharging curve of GCD, as shown in **Equation 3.4**. The C_{GCD} obtained can be used to evaluate the specific energy E and specific power P as expressed in **Equation 3.5** and **Equation 3.6** respectively.

$$C_{GCD} = \frac{i \cdot \Delta t_d}{m \cdot \Delta V} \quad (3.4)$$

$$E = \frac{1}{2} C_{GCD} (\Delta V)^2 \quad (3.5)$$

$$P = \frac{I \Delta V}{m} \quad (3.6)$$

Where i/m represents the current density ($A g^{-1}$), m is the weight of the composite electrode, Δt_d is the discharging time, ΔV is the potential difference of discharge, E is the energy density ($W h kg^{-1}$) and P is the power density ($W kg^{-1}$).

3.4.4.3 Frequency response analysis (FRA)

FRA allows us to explore the electrode structure, especially the interface between electrode and electrolyte. This can be done by investigating the alternating current generated in response to the alternating voltage applied on the electrode. The results obtained are the impedance behaviours as a function of frequency where $\omega = 2\pi f$. The resulting impedance behaviour is displayed as a Nyquist plot. It is a plot containing imaginary impedance (Z'') versus real impedance (Z'), which are the resolved components of $|Z|$ as a function of voltage. Each point on the plot is reacted correspondingly to the frequency applied.

In **Figure 3.4**, when a sinusoidal signal with small amplitude and fixed voltage of V_s is imposed on the voltage V of a system, the angular frequencies ω of the sinusoidal signal are carried out (Taberna & Simon, 2013). The resulting signal of current I is then measured. The linear relationship between I and V is remained when the signal is sufficiently small. It can be expressed as $V = IZ$. This equation is similar to Ohm's law, instead of resistance R , the impedance Z is used here. The frequency dependent I and V are shown as **Equation 3.7** and **Equation 3.8** respectively. The expression of impedance $Z(\omega)$ is shown as **Equation 3.9**, resulted from the ratio of $V(\omega)$ over $I(\omega)$.

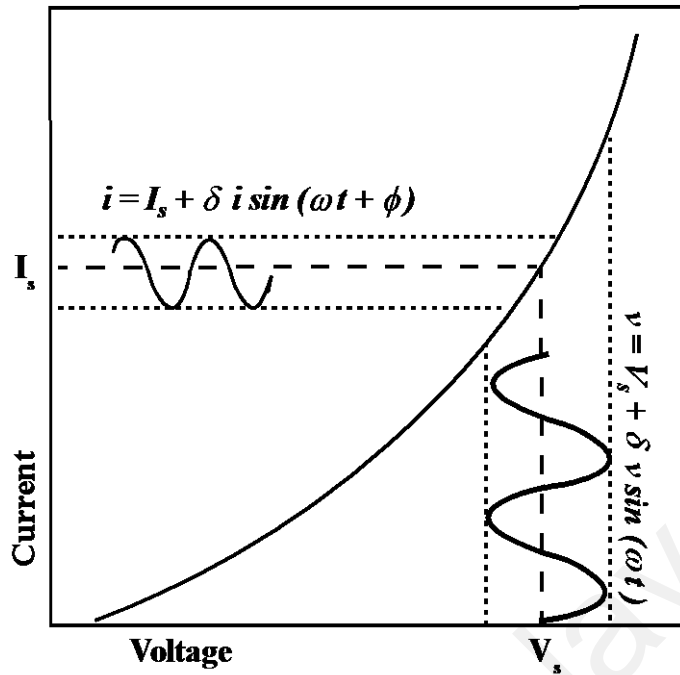


Figure 3.4: Stationary polarisation curve (black bold line). The measurement of resulting current when a sinusoidal voltage is imposed over a steady voltage.

$$I(\omega) = \delta I e^{[j(\omega t + \phi)]} \quad (3.7)$$

$$V(\omega) = \delta V e^{j\omega t} \quad (3.8)$$

$$Z(\omega) = \frac{\delta V}{\delta I} e^{-j\phi} = \frac{\delta V}{\delta I} (\cos \phi - j \sin \phi) = Z' + jZ'' \quad (3.9)$$

where δI is amplitude of current signal, δV is amplitude of voltage signal, t is time and ϕ is phase angle.

By using FRA, the capacitance as a function of frequency can be known from the imaginary component of the response, Z'' since $Z'' = 1/j\omega C$. Besides, the complex nature of the electrode/electrolyte interface can be interpreted. The observed frequency response can be fitted with an expected equivalent circuit model consisting of some simple elements. The most basic elements for the equivalent circuit are ohmic resistance component, R and pure capacitance component, C . The R is frequency independent, $Z' = R$ with zero phase angle. The C has an imaginary impedance which is frequency dependent, $Z'' = 1/j\omega C$ with a phase angle of 90° .

For supercapacitor, the electrode/electrolyte interface is always described. The evaluation of the interface is always inclusive of a solution resistance R_s , charge transfer resistance R_{ct} , double layer capacitance C_{dl} and pseudocapacitance C_{ϕ} .

University of Malaya

CHAPTER 4: CHARACTERISATIONS OF REDUCED GRAPHITE OXIDE- MANGANESE OXIDE COMPOSITE ELECTRODE SYSTEM

4.1 Introduction

Graphene sheet, as a single layer of sp^2 hybridised carbon atoms, has attracted worldwide interest in the development of advanced materials due to its excellent electrical conductivity and mechanical strength (Gómez-Navarro et al., 2007). However, it is not easy to obtain graphene sheets. There are several methods developed for graphene preparation such as micromechanical exfoliation of graphite, chemical vapour deposition (CVD) and chemical reduction of exfoliated graphite oxide (Juang et al., 2010; Novoselov et al., 2004; Stankovich et al., 2007). Although the micromechanical exfoliation of graphite is the most effective method to produce high quality of graphene, it is low-yield and thus limits the mass production (Novoselov et al., 2004). It turns out that the chemical reduction of exfoliated graphite oxide (GO) is a promising methodology. Before the exfoliation and reduction processes take place, an oxidation process is first carried out onto the graphite. GO is the product consists of multi-layered of carbon atoms resulted from this oxidation process.

During the oxidation process, the basal plane of GO are decorated with the epoxide and hydroxyl groups. At the same time, the edge atoms interact with the carbonyl and carboxyl groups (He et al., 1998). The exfoliation process of GO produces graphene oxide which contains only few layers of carbon atoms. It can be carried out via sonication method or mechanical stirring. In order to restore the properties of graphene, the graphene oxide is subjected to chemical reduction. Nevertheless, a perfect restoration of graphene structure is hard. The remains of defects are always detected. Hence, the material produced from this process is more appropriate to be termed as 'reduced graphene oxide'.

It is common to employ reduced graphene oxide as the electrode material for supercapacitor application. In our work, we explored the potential of reduced graphene oxide (RGO) prepared from the reduction of graphite oxide without exfoliation process. We investigated the combinational effect of RGO and manganese oxide prepared by electrodeposition method, at the same time we studied the effect of electrodeposition duration on the electrochemical performance of the prepared composite electrode.

This chapter will present the characterisation analysis of this composite electrode according to the field emission scanning electron microscopy (FESEM), X-ray diffraction (XRD), cyclic voltammetry (CV), galvanostatic charge-discharge (GCD) and frequency response analysis (FRA).

4.2 Reduced graphene oxide (RGO)

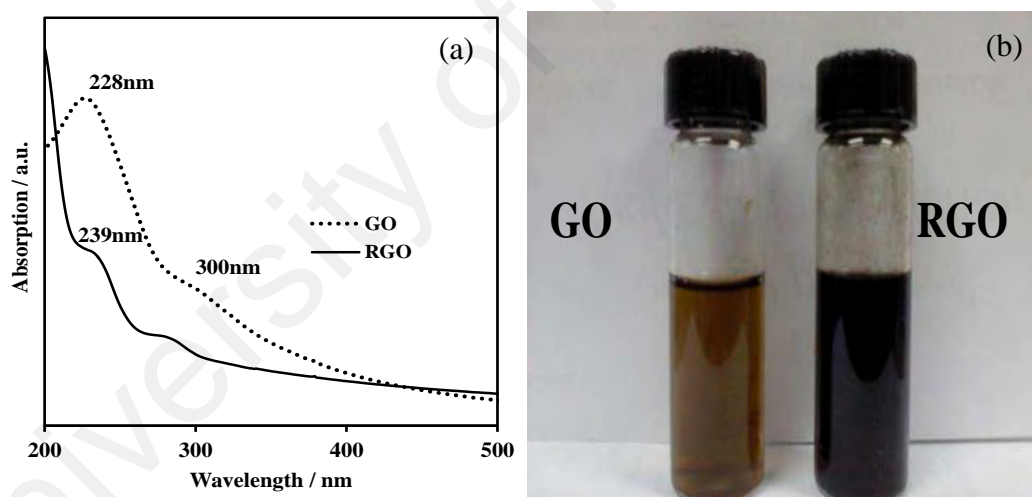


Figure 4.1: (a) UV-VIS spectra of GO and RGO and (b) the images of GO (left) and RGO (right).

UV-VIS measurement and optical observation are used to examine the production of RGO. **Figure 4.1 (a)** displays the evolution of UV-VIS spectra of GO solution while the corresponding images of GO and RGO are presented in **Figure 4.1 (b)**. The GO shows main absorbance peak at around 228 nm, which is attributed to the $\Pi-\Pi^*$ transitions of C=C and a broad hump at around 300 nm attributed to the $n-\Pi^*$ transition of C=O (Li et al., 2008). The GO solution exhibits brown colour. After reduction, the

solution turns to dark brown indicating the successful reduction by L-ascorbic acid. This is consistent with the UV-VIS spectra which also reveals the red-shift to 239 nm of RGO. The red-shift demonstrates the de-oxygenation and the restoration of Π -conjugation within RGO (Kumar et al., 2014). The UV-VIS result suggests the similar structure of GO and RGO in this study (Marcano et al., 2010).

4.3 Field emission scanning electron microscopy (FESEM)

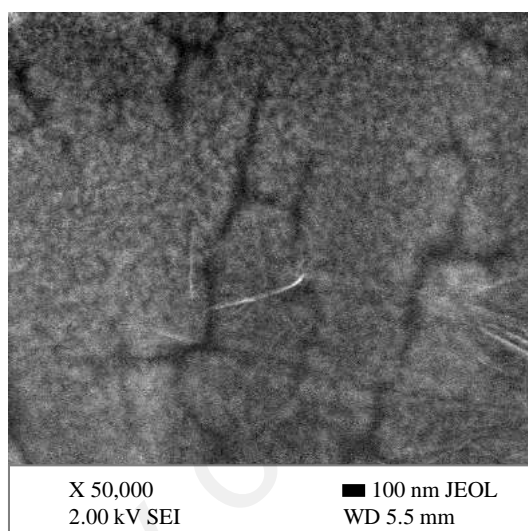


Figure 4.2: FESEM image of composite film deposited at 10 mins.

The images of RGO-manganese oxide composite were characterised using FESEM. In overall, the substrate is well covered by deposit which exhibited rough surface. The amount of composite film deposited is in the range of 0.1–0.3 mg. **Figure 4.2** displays the FESEM image of composite electrode deposited at 10 mins. From the image, one can realise the formation of a closely packed structure with the presence of crack that is resulted from the post-heating treatment. The morphology is irregular, causes the unavailability to estimate grain size. Higher magnification does not help to reveal the morphology details as the image appeared to be very unclear. Nevertheless, higher magnification is used to inspect the morphology of composite electrode obtained at longer deposition duration.

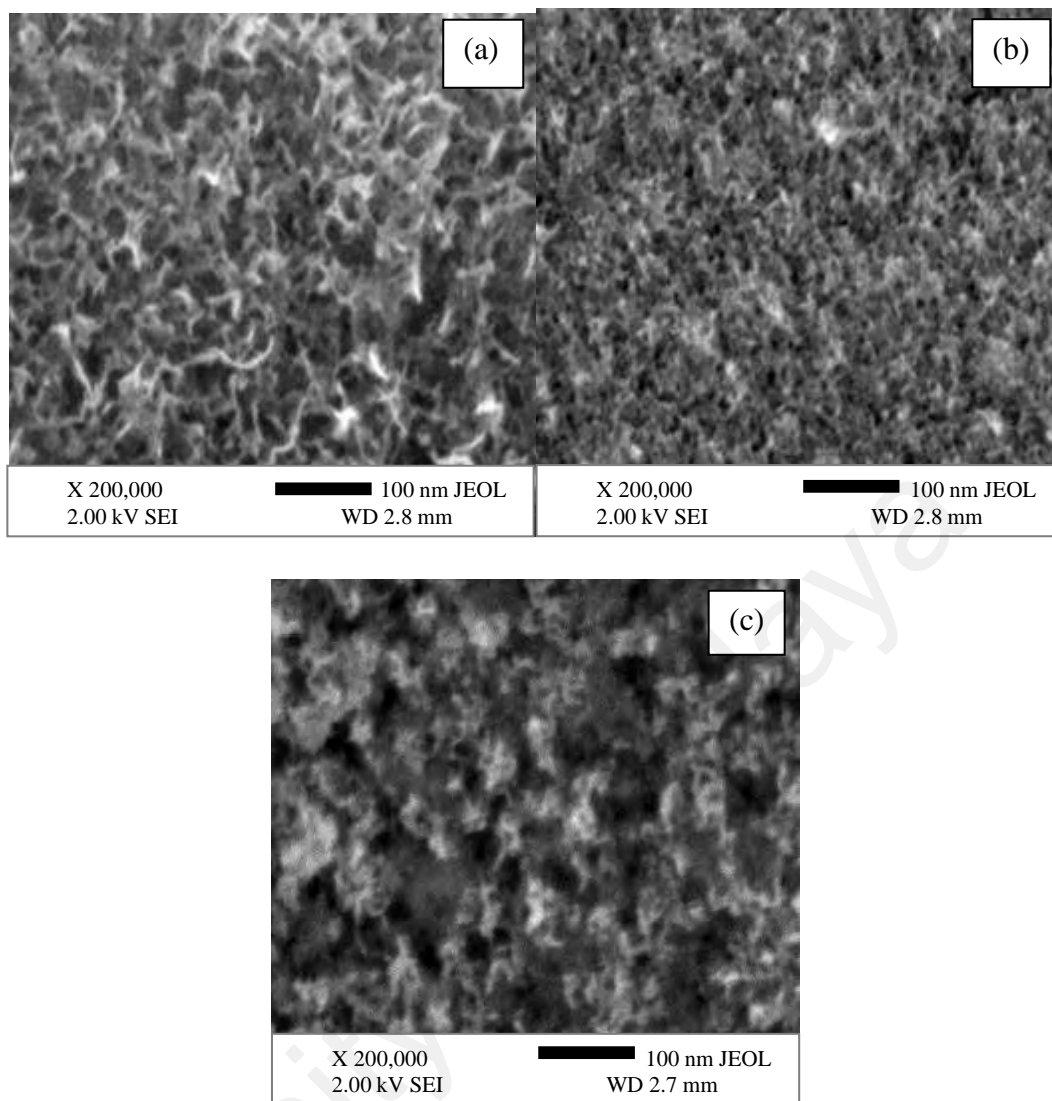


Figure 4.3: FESEM images of RGO-manganese oxide deposited at (a) 13 mins, (b) 15 mins and (c) 18 mins at 200k of magnification.

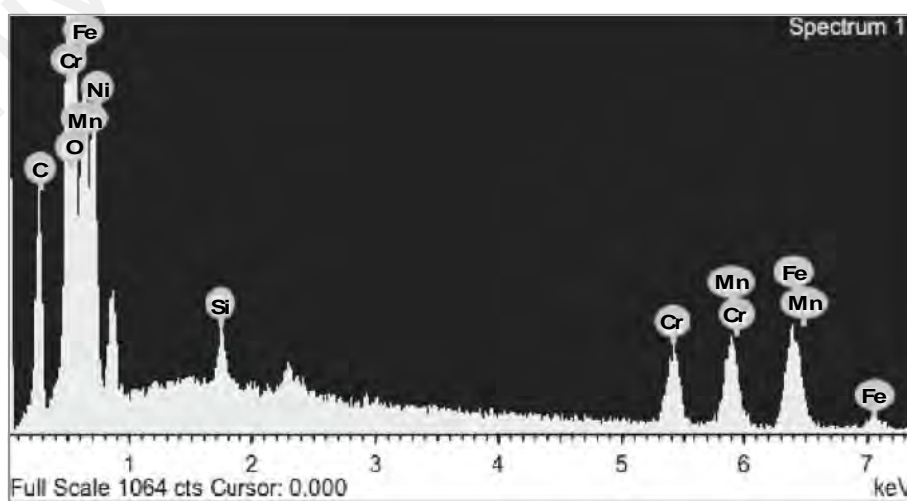


Figure 4.4: EDX analysis of composite electrode.

As shown, a flaky structure is developed at 13 mins of deposition (**Figure 4.3 (a)**). The vertically grown structure offers opportunities for the penetration of electrolyte ions. When the deposition duration was extended to 15 mins, the structure aggregated due to more deposit was accumulated on the top as shown in **Figure 4.3 (b)**. At 18 mins of deposition duration, the structure is further agglomerated without changing the morphology significantly (**Figure 4.3 (c)**). The effect of agglomeration on the electrochemical performance of the composite electrode is noticed during the electrochemical tests. The elemental analysis by EDX reveals the presences of manganese (Mn), oxygen (O) and carbon (C) originated from the composite electrode, **Figure 4.4**. The signals of iron (Fe), chromium (Cr) and silicon (Si) can be contributed by the stainless steel and sample holder.

4.4 XRD study

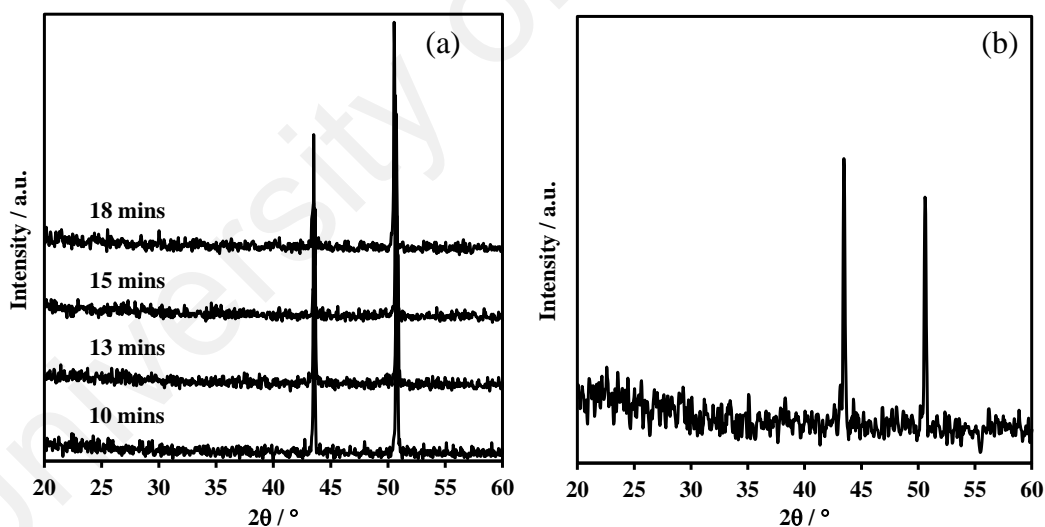


Figure 4.5: XRD pattern of (a) composite electrodes, (b) bare stainless steel and (c) scraped off composite films.

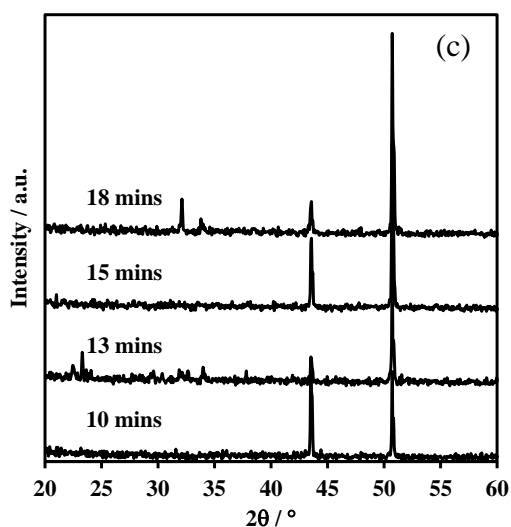


Figure 4.5 (c): Continued.

The X-ray diffraction patterns of composite electrodes prepared at different durations and bare stainless steel are shown in **Figure 4.5 (a)** and **(b)** respectively. Two peaks are detected for both deposited and bare stainless steels. In order to find out the crystalline phase of composite film, the film is scraped off from the stainless steel and examined using XRD again. The result is displayed in **Figure 4.5 (c)**. Two peaks are noticed in **Figure 4.5 (c)** which is similar to **Figure 4.5 (a)**. This shows that the diffraction peaks of composite film located near to diffraction peaks of stainless steel. The poor crystallinity of composite film causes its diffraction peaks to be hidden by strong peaks of stainless steel. Although there are two peaks noticeable for the composite film, it is insufficient to determine the lattice structure of the composite film formed. Furthermore, a deposited film is usually exhibited amorphousness in nature (Hu & Tsou, 2002; Jacob & Zhitomirsky, 2008). As the structure cannot be ascertained, the chemical formula of the composite film formed cannot be verified. Nevertheless, previous studies confirmed the formation of manganese oxide that prepared in similar ways though different types of manganese oxide can be formed (Nagarajan et al., 2006; Wei et al., 2007). Hence, the composite film here is straightforwardly named as ‘RGO-manganese oxide’.

4.5 Electrochemical performance

4.5.1 Cyclic voltammetry (CV)

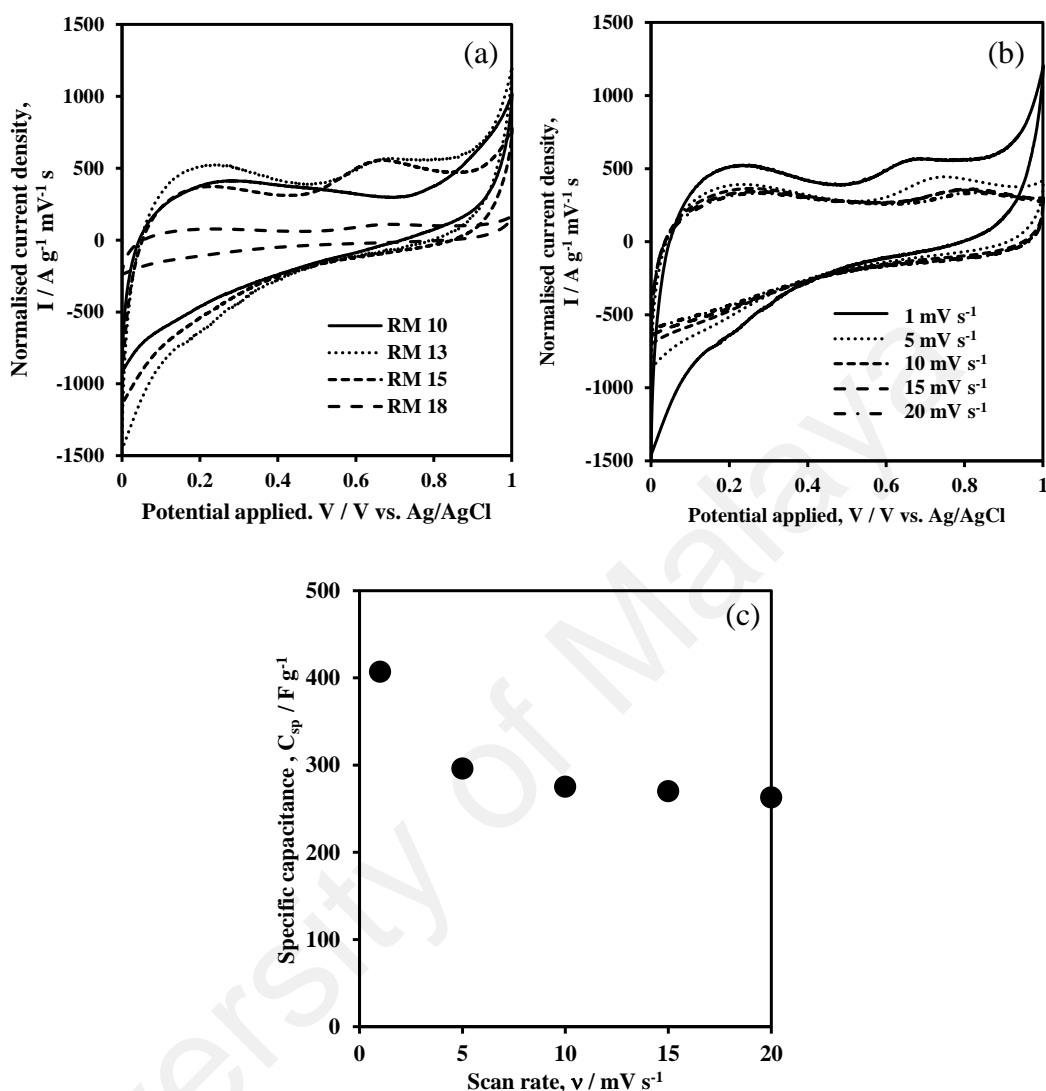


Figure 4.6: (a) CV curves of composite electrodes at 1 mV s⁻¹, (b) CV curves of RM 13 at different scan rates, and (c) graph of specific capacitance against scan rate (RM 13).

To characterise the electrochemical properties of the composite electrode, cyclic voltammetry measurement was performed in 1 M Na₂SO₄. The potential window is restricted within 0.0 to 1.0 V in order to avoid the occurrence of oxygen evolution reaction due to the decomposition of water in the electrolyte. The cyclic voltammogram of composite electrodes prepared at various deposition durations is displayed in **Figure 4.6 (a)**. In overall, the CV curves exhibit a nearly rectangular shape indicates the dominance of surface pseudocapacitance. This is reasonable since the morphology

formed is flaky in structure as shown in FESEM, the charge transfer reactions mostly take place on the surface of the composite film. On the other hand, a broad hump is observable near 0.8 V. The presence of hump recommends the occurrence of insertion of electrolyte ions into the composite film. However, the hump is absent in CV curve of RM 10. This can be related to the morphology of RM 10 which is compact and exposing the surface of the film to the electrolyte. The movement of electrolyte ions are restricted onto the surface of composite film and cannot penetrate deeper into the film. In spite of that, the hump is clearly seen on CV curves of RM 13, RM 15 and RM 18. This depicts the fact that insertion of electrolyte ions has taken place in these composite electrodes.

Table 4.1: Specific capacitances estimated for composite electrodes deposited at different durations.

Deposition duration, t / mins	Specific capacitance, C_{sp} / F g ⁻¹
10	325
13	407
15	336
18	69

It is noted that the normalised current density of RM 13 is the highest at the same scan rate of 1 mV s⁻¹. This suggests that RM 13 possesses the highest specific capacitance. By using **Equation 3.2**, the specific capacitance of RM samples deposited at different durations are evaluated, as shown in **Table 4.1**. A remarkable increase in specific capacitance from 325 to 407 F g⁻¹ is detected when the deposition is prolonged from 10 to 13 mins. It is around 25 % of increment from 325 F g⁻¹. The enhancement of specific capacitance can be attributed to the evolution of morphology from compact structure to a more flaky porous structure. The significant increasing in specific capacitance proposes the importance of porous structure compared to compact structure. However, the specific capacitance decreases from 407 to 336 F g⁻¹ for the composite

electrode deposited at 15 mins and further reduces abruptly to 69 F g^{-1} when the composite electrode was prepared at 18 mins. Similar to RM 10, the drop of specific capacitance for composite electrode prepared at 15 mins can be understood through the formation of structure. From **Figure 4.3 (b)**, one can notice the agglomeration of structure when the deposition is extended from 13 to 15 mins. The agglomeration of deposits occurred horizontally and distributed on the surface of the composite film. Instead of evolving into a more advantageous structure, the agglomeration diminishes the porous structure. When the deposition is carried out for 18 mins, the deposits are further accumulated onto the film vertically forming the island-like structure as observed in **Figure 4.3 (c)**. Although a porous structure can be formed as the bigger pores are noticeable, the greater amount of electrolyte ions that diffuse near to the surface of film may hinder each other from further interaction by contrast. This causes the higher charge transfer resistance and will be discussed in the following section.

Since RM 13 is shown to be the best composite electrode, further evaluation is carried out on RM 13. The CV curves of RM 13 at different scan rates are shown in **Figure 4.6 (b)**. As the scan rate increases from 1 to 20 mV s^{-1} , the shapes of the CV curves are not altered significantly indicating good rate of capability of this composite electrode (Lu et al., 2011). The specific capacitance for each scan rate is estimated again using **Equation 3.2**. **Figure 4.6 (c)** displays the variation of specific capacitance with scan rate. RM 13 reaches the highest specific capacitance of 407 F g^{-1} at 1 mV s^{-1} . When the scan rate increases to 5 mV s^{-1} , the specific capacitance decreases to 296 F g^{-1} . Further increasing in scan rate leads to a gradual drop in specific capacitance, that is 275 F g^{-1} , 270 F g^{-1} and 263 F g^{-1} at 10 mV s^{-1} , 15 mV s^{-1} and 20 mV s^{-1} respectively. The good performance of this composite electrode, RM 13, can be attributed to its structure. Herein, the reduced graphite oxide-manganese oxide deposited directly on stainless steel and formed a flaky porous structure at 13 mins of

deposition. There are several benefits regarding to this: (1) the direct contact between composite film and stainless steel is advantageous for electron transportation which ensures their participation as much as possible, (2) the open space produced from porous structure is not only favourable for adsorption of electrolyte ions on the surface, but also the insertion of ions into deeper sites of the film and (3) the amorphousness of the composite film facilitates more proton transportation as the charge storage mechanism of manganese oxide depends on both electrolyte ions and proton (Lu et al., 2011; Toupin et al., 2004).

4.5.2 Galvanostatic charge-discharge (GCD)

The galvanostatic charge-discharge (GCD) test has been carried out for all composite electrodes in order to further evaluate the electrochemical performance. To focus on the effect of deposition duration on capacitive performance of composite electrode, the corresponding discharging curves of composite electrodes deposited at different durations are shown in **Figure 4.7 (a)**. Based on the figure, the distinction between RM 13 and other samples is clearly observed. It is obvious to see that RM 13 has relatively better capacitive performance as it can sustain the charge for longer time. However, composite electrodes deposited at 10, 15 and 18 mins show very fast discharging time. Since all the samples have identical charge-discharge curves shape, the full GCD curve of RM 15 is chosen to represent other samples (**Figure 4.7 (b)**). It is well known that the charge-discharge curve of EDLC exhibits linear behaviour revealing the double layer effect. As a hybrid composite electrode, GCD curves of RM 15 exhibit non-linear behavior indicating the participation of charge transfer reaction. The charge curve is symmetry to its discharge counterpart in the whole potential region. At higher current, the discharging time is even faster. This shows that composite electrodes prepared at 10, 15 and 18 mins are not good enough for supercapacitor application.

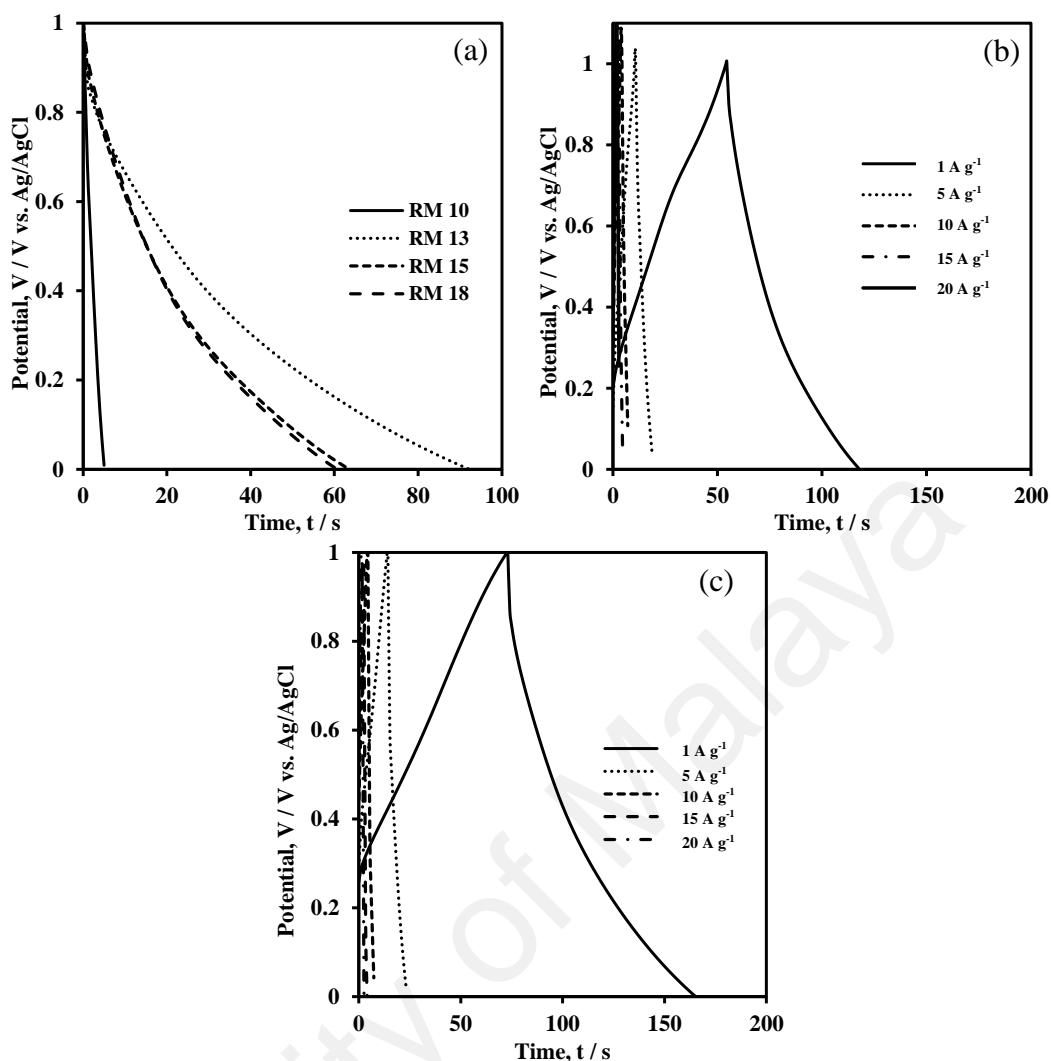


Figure 4.7: Galvanostatic (a) discharging curves of composite electrodes at various deposition duration and charge-discharge curves of (b) RM 15 (c) RM 13 at different current densities.

The GCD curves for RM 13 measured in between 0 – 1 V at different currents are shown in **Figure 4.7 (c)**. The non-linear behavior of GCD curve is observed, as explained in **Figure 4.7 (b)**. According to **Equation 3.4**, the specific capacitance estimated for RM 13 in this test is 498 F g^{-1} at 1 A g^{-1} . This value is higher than 407 F g^{-1} which is obtained at 1 mV s^{-1} in CV test. This suggests that the time given may not enough for complete charge transfer reactions to occur at 1 mV s^{-1} in CV measurement. In this case, lower scan rate can offer even higher specific capacitance. Since GCD test can provide more precise information about the charge storage, we take into account the specific capacitance derived from here instead of the one estimated

from CV. Nevertheless, CV is important to evaluate the electrochemical activity of active species in the solution or on the film.

4.5.3 Frequency response analysis (FRA)

The fundamental behaviour of the composite film was examined using Frequency Response Analysis (FRA). **Figure 4.8 (a)** presents the Nyquist plot of the composite film performed at the frequency range of 0.1 Hz to 100 kHz in 1 M Na₂SO₄. The Nyquist plot consists of a high frequency intercept on the real axis, a semicircle, and a linear region at low frequency range. The leading resistance in the high frequency region represents the equivalent series resistance R_{ESR} , which is the combination of electrolyte resistance, resistance of the composite film, and contact resistance at composite film/stainless steel interface. The R_{ESR} obtained by composite electrodes deposited at 10, 13, 15 and 18 mins are small, which is in between 1 – 1.2 Ω . On the other hand, by evaluating the diameter of the semicircle, the charge transfer resistance R_{ct} can be found. The visual observation shows that the composite film has a small R_{ct} . The R_{ct} estimated are 1.3, 2.4, 3.1 and 4.8 Ω for composite electrodes deposited at 10, 13, 15 and 18 mins respectively. As mentioned earlier, the R_{ct} can be related to the electrochemical performance. The very low specific capacitance of RM 18 can be caused by agglomeration of structure that leads to the relatively higher R_{ct} . The flaky porous structure owned by RM 13 and RM 15 possesses lower R_{ct} as expected. Lower frequency region, basically referred to the straight line after the depressed semicircle, indicates the diffusion condition of the charges. Ideal capacitor will have a vertical straight line. However, as hybrid composite electrode is produced in this work, an inclined straight line should be observed, as obtained in this work.

The behaviour of the composite electrode in the electrolyte was simplified using equivalent circuit, as shown in **Figure 4.8 (b)**. Higher frequency region show us the solution resistance indicated as R_s . The resistive element in the loop represents R_{ct} . The

capacitive element C indicates the participation of double layer effect. The CPE is used to describe the diffusion process of the charges. In general, CPE can be induced by diffusion-limited condition, geometric factors, crystallographic heterogeneity and sluggish processes for example adsorption of anions.

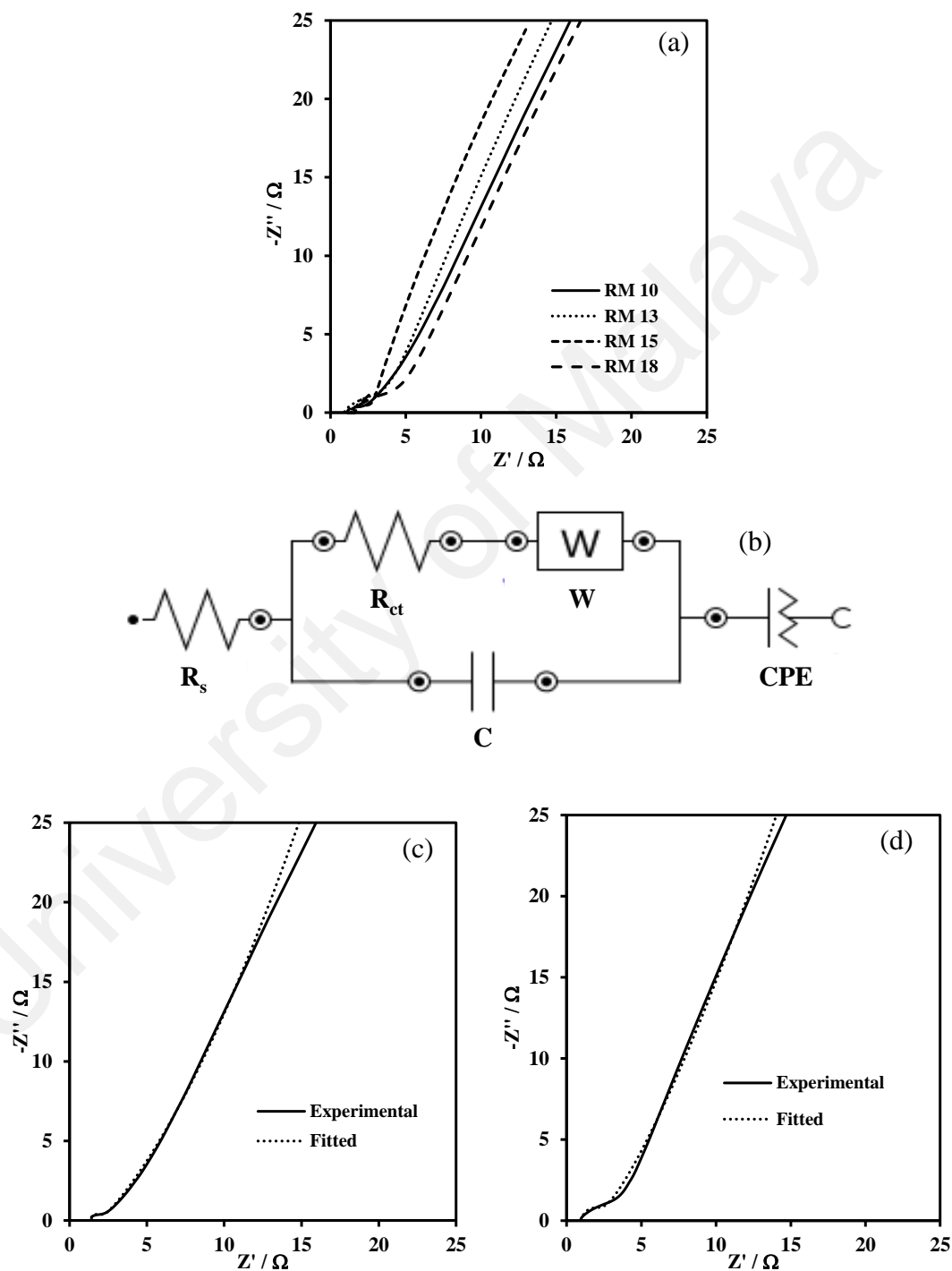


Figure 4.8: Impedance test result of composite electrode deposited at different durations (a) Nyquist plot, (b) equivalent circuit and fitted Nyquist plot at (c) 10 mins, (d) 13 mins, (e) 15 mins and (f) 18 mins.

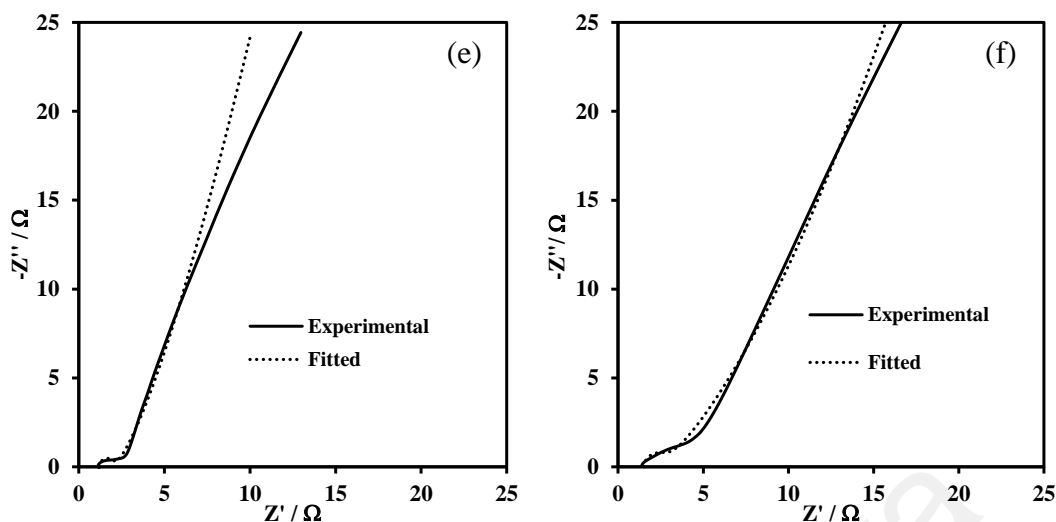


Figure 4.8: Continued.

4.6 Cycle stability

In order to examine the long term stability, at the same time inspect the changing in electrochemical activity of RM 13, this composite electrode undergoes CV measurement at 10 mV s^{-1} for 1000 cycles. The result is shown in **Figure 4.9 (a)**. Instead of dropping rapidly, the capacitance is noticed to reduce gradually during the cycling. The capacitance retention remains quite stable during 200th to 650th cycles. It is found that RM 13 can retain around 83 % after 500 cycles and 78 % after 1000 cycles. There is no increasing in specific capacitance during the cycling process as observed in other studies. This shows that no activation process during the stability test.

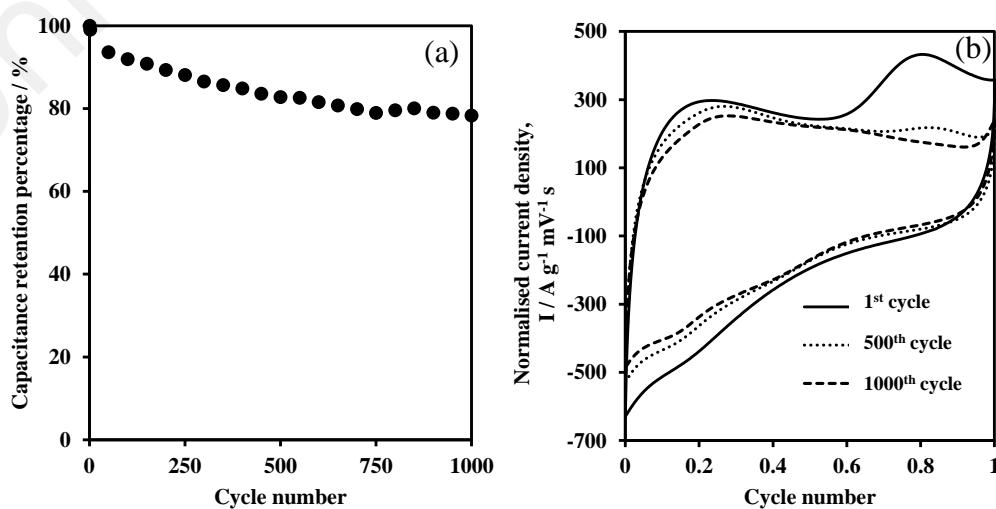


Figure 4.9: (a) Capacitance retention percentage and (b) normalised current density as a function of cycle number for RM 13.

As shown in **Figure 4.9 (b)**, the deviation of 500th cycle and 1000th cycle from first cycle is noticed indicating the degradation has occurred inside the composite film. The degradation is caused by the partial dissolution of composite film after long cycling as indicated by the decreasing in CV curve area (Francois Beguin, 2009). Besides, the disappearance of redox peak at 500th cycle and 1000th cycle shows the reduced interaction between electrolyte ions and composite film thus leads to less charge transfer reactions. In overall, RM 13 can retain about 78 % of initial capacitance after 1000 cycles.

4.7 Summary

- Amorphous composite electrode consists of RGO and manganese oxide has been fabricated using electrodeposition technique.
- The effect of deposition duration on the electrochemical performance of composite electrode has been evaluated based on FESEM, XRD, CV, CD and FRA.
- 13 mins was found to be the optimal deposition duration for this composite electrode. A flaky porous structure was formed which is ease for penetration of electrolyte ions.
- RM 13 can attain 78 % of initial capacitance after 1000 cycles. Unavoidable partial dissolution of composite film was recognised from CV curve during the cycling test.

CHAPTER 5: CHARACTERISATIONS OF MANGANESE-NICKEL OXIDE COMPOSITE ELECTRODE SYSTEM

5.1 Introduction

The nickel oxide is widely studied as spinel type nickel cobalt oxide ($\text{Ni}_x\text{Co}_{3-x}\text{O}_4$, $0 < x \leq 1$) due to its promising electrochemical activity (Du et al., 2013; Yuan et al., 2012). However, there is not many reports on manganese-nickel oxide composite electrode. In this chapter, we have incorporated nickel oxide with manganese oxide to form a composite electrode. We have studied about the effect of deposition duration on the composite electrode and determined the optimal electrodeposition duration. The material characteristics of manganese-nickel oxide composite electrode are examined using field emission scanning electron microscopy (FESEM), transmission electron microscopy (TEM), X-ray diffraction (XRD), cyclic voltammetry (CV), galvanostatic charge-discharge (GCD) and frequency response analysis (FRA).

5.2 Field emission scanning electron microscopy (FESEM)

Figure 5.1 (a)-(d) display the surface morphologies of manganese-nickel oxide composite electrodes deposited at different durations (10, 13, 15 and 18 mins). The images show that deposited composite film has fully covered the stainless steel substrate. There is no distinct boundary found between two compositions indicating they are well interconnected. The spongy-like structure formed at 10 mins of deposition duration slowly transformed into a more homogeneous film at longer deposition duration.

To study the interior structures of composite film, the composite film was scraped off from the stainless steel for the TEM analysis. The results are shown in **Figure 5.2**.

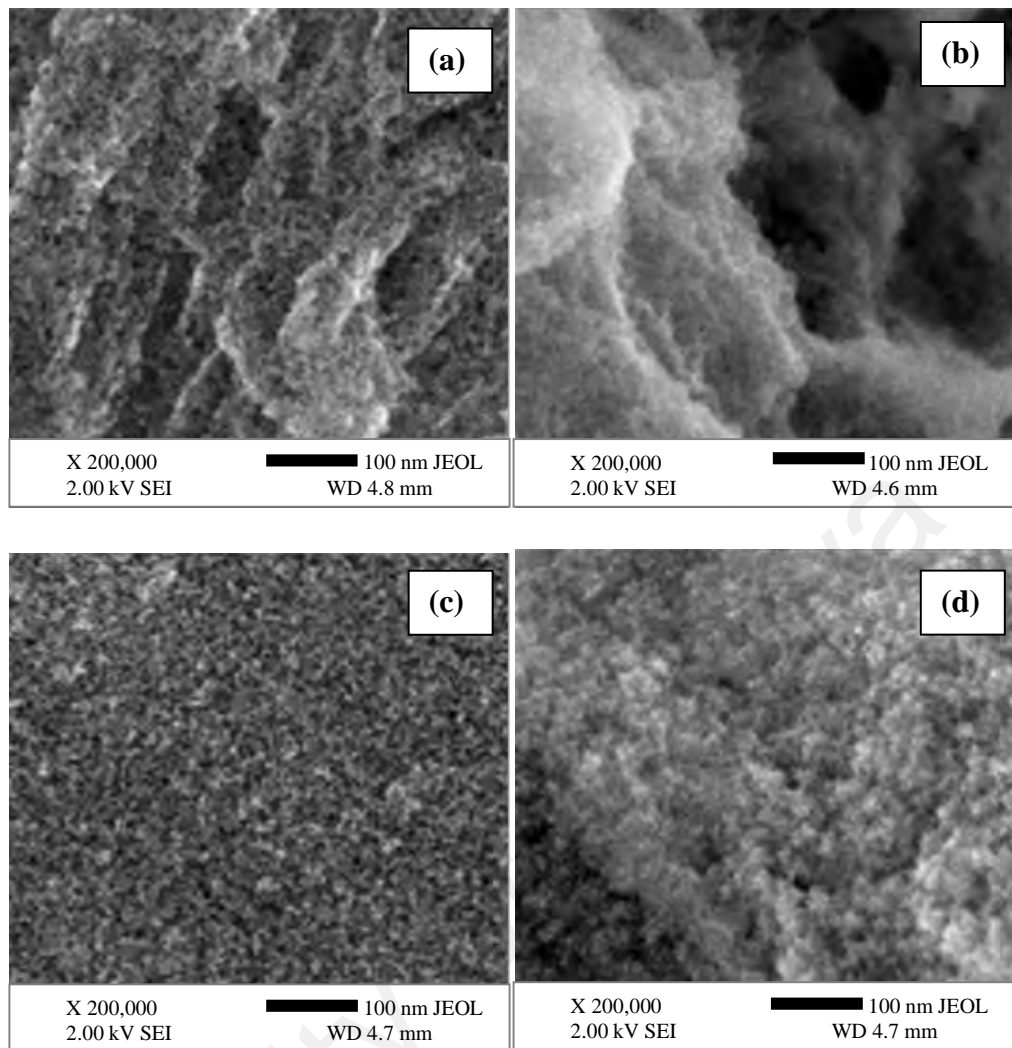


Figure 5.1: FESEM images of composite films deposited at (a) 10 mins, (b) 13 mins, (c) 15 mins and (d) 18 mins.

5.3 Transmission electron microscopy (TEM)

TEM image disclosed the porous network in the composite film. The composite remained interconnected after being scraping off suggesting the excellent interconnection between the nanoparticles. The presence of dark spots resulted from the particle aggregation is observed in **Figure 5.2 (a), (c) and (d)** while it appears to be more well-distributed in **Figure 5.2 (b)**.

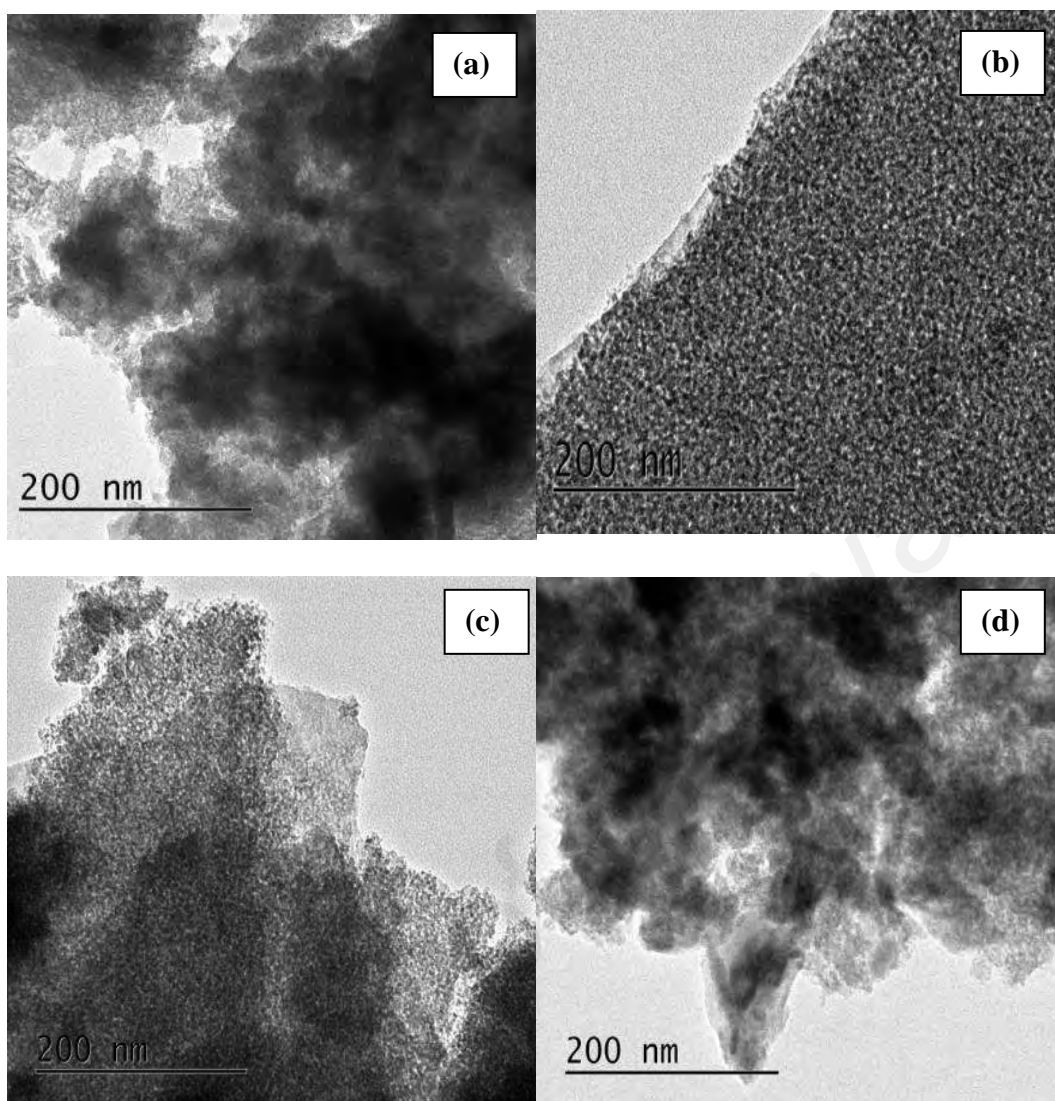


Figure 5.2: TEM images of composite films deposited at (a) 10 mins, (b) 13 mins, (c) 15 mins and (d) 18 mins at 40k magnifications.

In overall, the spongy porous structure can retains electrolyte ions and ensures the occurrence of Faradic reactions. From the morphological studies, short deposition duration (10 mins) is found insufficient to form a uniform structure while relatively longer deposition duration (15 and 18 mins) can lead to particle aggregation. FESEM and TEM results show that 13 mins is optimal to form a uniform and homogenous structure.

5.4 X-ray diffraction (XRD)

The crystallinity of the composite film is analysed using X-ray diffraction (XRD).

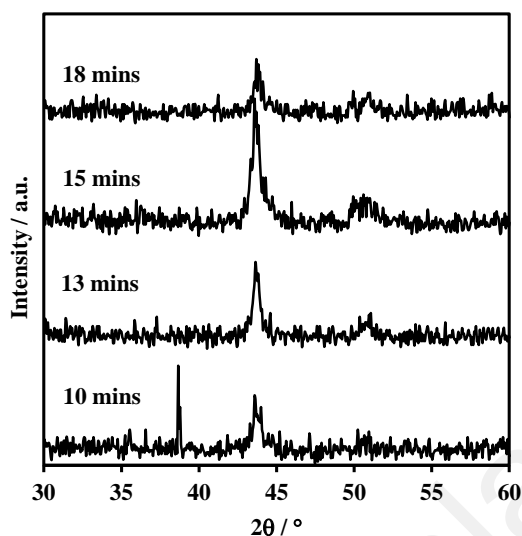


Figure 5.3: XRD patterns of composite film deposited at different durations.

In **Figure 5.3**, XRD pattern corresponding to the composite films deposited at various durations is shown. They exhibited similar patterns with two broad peaks at around $2\theta = 44^\circ$ and $2\theta = 51^\circ$ detected. The broad peaks observed cannot be resolved well indicating the formation of non-stoichiometry composite film. There is no discernible diffraction peaks regarding to manganese oxide and nickel oxide were found. This suggests that the components exist in the form of composite. The absence of specific diffraction peaks of manganese oxide and nickel oxide along with the formation of weak peak implies the amorphous nature of the deposited composite film. There is neither manganese/nickel metal nor crystalline manganese/nickel oxide are formed. The amorphous composite film is more favourable compared to crystalline due to its more flexible interaction of electrolyte ions with the electroactive sites (Zheng, 1999).

5.5 Electrochemical performances

5.5.1 Cyclic voltammetry (CV)

The specific capacitance of manganese oxide is dependent on its crystal structure which can be determined by the post-heating temperature. It is known that, the

pseudocapacitance of oxide material can be influenced by the water content (Zheng et al., 1995). The post-heating temperature of 400 °C could cause the loss of water content inside manganese oxide and thus led to decrease in specific capacitance (Reddy & Reddy, 2004). Hence, in this work, we heated the as-prepared composite electrode at 300 °C in order to retain the water content inside the composite.

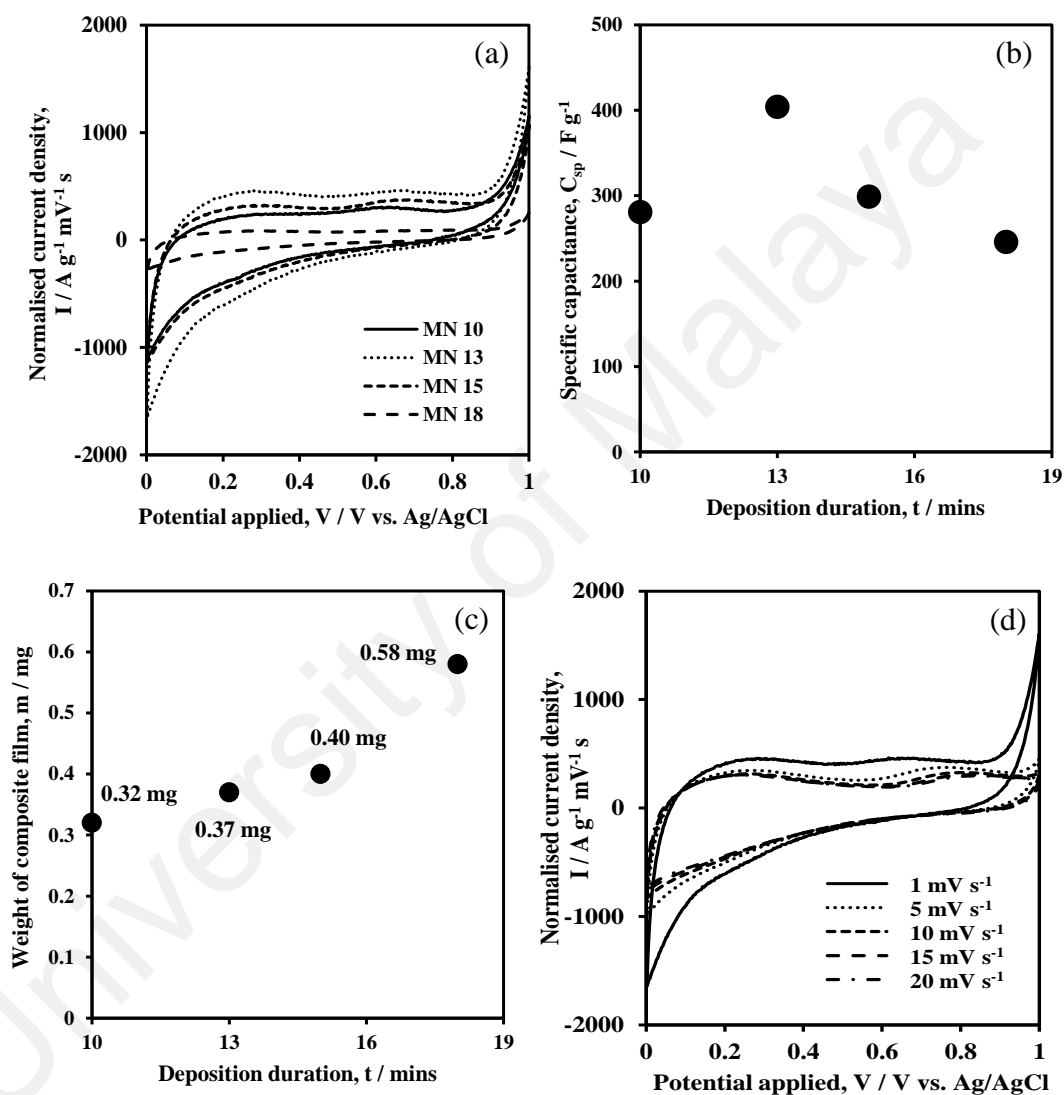


Figure 5.4: (a) CV curves of composite films deposited at different deposition durations at 1 mV s^{-1} , (b) specific capacitances obtained at various deposition durations, (c) composite film weights varied with deposition durations and (d) normalized CV curves of composite film deposited at 13 mins for different scan rates.

The CV test is measured from 0.0 to 1.0 V versus Ag/AgCl in 1 M Na₂SO₄ electrolyte using three-electrode configuration. The result is displayed in **Figure 5.4 (a)**. In overall, the CV curves show rectangular shape. A broad oxidation peak in the potential range of 0.6 – 0.8 V is observed in all CV curves. The rectangular envelope of CV curves clarifies the predominance of surface pseudocapacitance in the overall charge transfer reactions. The presence of broad peak illustrates the insertion of electrolyte ions into the composite film. The areas of CV curve is found to increase significantly from 10 mins to 13 mins of deposition duration. However, the CV curves area dropped gradually with longer deposition durations (15 and 18 mins). This can be related to the rate capability or ionic motion in the composite film. Higher rate capability results in better ionic motion and thus wider area of CV curve.

The rate capabilities of the composite films deposited at different durations can be investigated by estimating the specific capacitance C_{sp} achieved by each composite electrodes. This can be done by examining the discharging part of CV curve. The result is demonstrated in **Figure 5.4 (b)**. The specific capacitance increased from 281 F g⁻¹ (10 mins) to 404 F g⁻¹ (13 mins). After that, it reduced to 299 F g⁻¹ (15 mins) and further dropped to 246 F g⁻¹ (18 mins). So, the highest specific capacitance has been achieved by composite film deposited at 13 mins.

In general, the weight and thickness of the composite film increase with longer deposition duration. However, an accurate film thickness measurement is hard due to the spongy-like with porosity structure. Hence, the deposited film weight is considered instead of the film thickness. **Figure 5.4 (c)** shows the variation of film weight (mg) with the deposition duration. The weight of the composite film is increased with longer deposition duration. Nevertheless, the specific capacitance does not increase accordingly after 13 mins of deposition duration. The maximum weight obtained at longest deposition duration which is 18 mins in this study is 0.58 mg. The weight of

composite film for highest specific capacitance (404 F g^{-1}) is 0.37 mg deposited at 13 mins. A higher composite film weight does not ensure a better electrochemical performance. Instead, the relatively heavy loaded composite film (0.58 mg) showed a significantly reduced charge storage ability (246 F g^{-1}). This is because the redox reactions only take place on the surface and sub-surface of the bulk material. Hence, the redox reactions proceed slower with a higher film weight which has a higher ionic transportation resistance and poorer rate capability. As a consequence, the specific capacitance decreases at longer deposition duration.

Table 5.1: Specific capacitances obtained at different scan rates for 13 mins-deposited composite film.

Scan rate, $\nu / \text{mV s}^{-1}$	Specific capacitance, $C_{sp} / \text{F g}^{-1}$
1	404
5	298
10	264
15	252
20	246

The capacitive behavior of 13 mins-deposited composite film is further evaluated using different scan rates. The CV curves obtained are shown in **Figure 5.4 (d)** while the specific capacitances C_{sp} estimated are tabulated in **Table 5.1**. A purely capacitive region is identified at the cathodic scan between 0.5 and 0.8 V . This region is found not affected by the scan rate indicating it is not diffusion limited and thus it can be corresponding to the double layer capacitance. The broad peak at $0.6 - 0.8 \text{ V}$ is scan rate-dependent implying the redox reaction is diffusion controlled.

The CV curve becomes more depressed with increasing scan rate. This results in the decreasing of specific capacitance. The value of specific capacitance obtained is dependent on the amount of electrolyte ions near the electroactive sites of composite film. Due to the shorter diffusion time supplied by the higher scan rate, the electrolyte ions near the film surface experience depletion/saturation during the reduction/oxidation

processes. This causes the increase in ionic resistance thus produces lower specific capacitance value. In contrast, electrolyte ions are able to interact with more inner electroactive sites at relatively low scan rate (1 mV s^{-1}) thus contributes to higher capacitance value.

5.5.2 Galvanostatic charge-discharge (GCD)

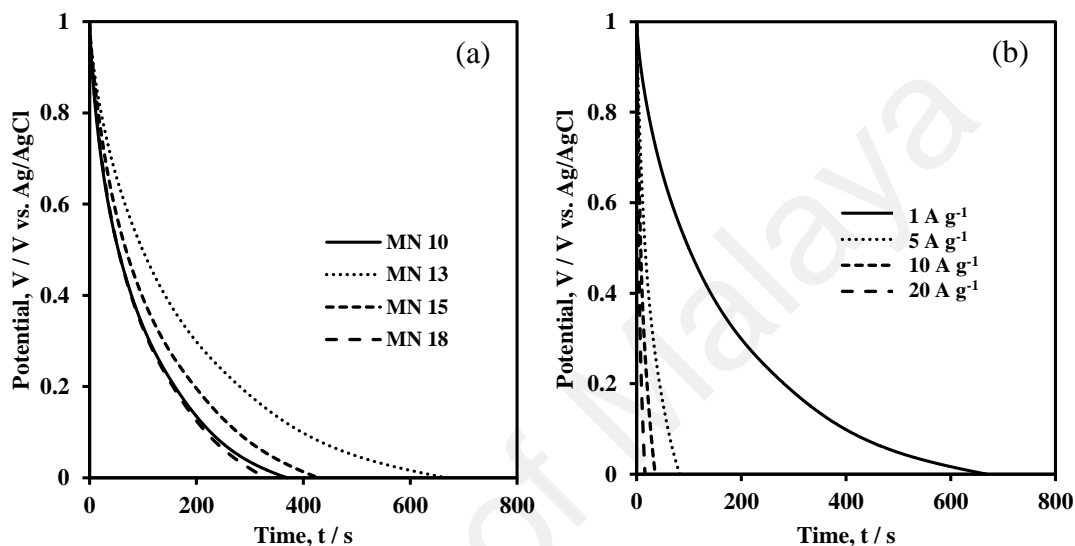


Figure 5.5: Discharging curve of composite films deposited at (a) different durations at 1 A g^{-1} and (b) 13 mins at various current densities.

Figure 5.5 (a) shows the discharging curves of all composite electrodes at 1 A g^{-1} . As a pseudocapacitive material, the discharging curves are deviated from a straight line that represents the behaviour of an ideal capacitor. The curved line is resulted from the redox activity in the composite electrodes. The discharging time depicts the total time required to unload the charges stored. Higher charge storage is expected to spend more time for discharging. The composite film deposited at 13 mins is found to consume longest time for discharging. The specific capacitance C_{GCD} also can be calculated from discharging curve obtained from GCD. The values of specific capacitance estimated from CV and GCD are shown in **Table 5.2**. The C_{GCD} estimated is consistent with the order indicated by CV. 13 mins is found to be the optimal deposition duration to prepare a composite electrode with the highest charge storage. **Table 5.3** displays the specific

energy and specific power values derived from C_{GCD} at 1 A g^{-1} . As shown, 13 mins-deposited composite film possessed the highest specific energy while 10 mins-deposited composite film owned the lowest. **Figure 5.5 (b)** demonstrates the discharging curve of 13 mins-deposited composite film at different current densities. The specific capacitances at various current densities are estimated using **Equation 3.4**. The highest specific capacitance obtained is 670 F g^{-1} at current density of 1 A g^{-1} . The specific capacitance decreases with higher current density due to the increase in voltage drop and inadequate active material took place in charge transfer reactions (Xiong et al., 2015). When current density is higher than 10 A g^{-1} , the specific capacitance decreases gradually indicating stable ionic and electron transportation at relatively higher current density. This shows that spongy-like structure allows good ion diffusion and electron transportation at high current density.

Table 5.2: Specific capacitances obtained from CV and GCD at various deposition durations.

Deposition duration, t / mins	$C_{sp} / \text{F g}^{-1}$ at 1 mV s^{-1}	$C_{GCD} / \text{F g}^{-1}$ at 1 A g^{-1}
10	281	371
13	404	670
15	299	430
18	246	330

Table 5.3: Specific energy and specific power estimated from C_{GCD} at 1 A g^{-1} for composite film deposited at different durations.

Deposition duration, t / mins	Specific energy, $E / \text{W h kg}^{-1}$	Specific power, $P / \text{W kg}^{-1}$
10	51.19	996.69
13	92.61	997.60
15	59.40	997.28
18	45.58	997.27

5.5.3 Impedance Analysis and Cycle Stability

Figure 5.6 (a) displays the Nyquist plots of composite films deposited at various durations. The Nyquist plot can be divided into three regions: high frequency, high-to-medium frequency and low frequency. The high frequency region involves the ohmic resistance which consists of the electrolyte resistance contact resistance at film/substrate interface and intrinsic resistance of the substrate. The high-to-medium frequency region contains a depressed semicircle resulted from the charge transfer reactions. The sloping straight line that can be related to diffusive resistance is observed in the low frequency region.

Figure 5.6 (b) presents the equivalent RC circuit model proposed to analyse the impedance data of the composite film while **Figure 5.6 (c)-(f)** show the fitted Nyquist plots built according to the proposed equivalent circuit. The model is constructed by a solution resistance R_s , charge transfer resistance R_{ct} , capacitive element C_{dl} , Warburg element W and constant phase element CPE . From the equivalent circuit proposed, the ac behaviour of the composite film can be evaluated as following. At a very high frequency, only the outer most surface of the film is accessible for the electrolyte ions. The impedance is purely ohmic and represented by R_s . The R_s is small for all composite films with 10 mins-deposited composite film possessed the highest R_s . When the frequency is decreased, the impacts of composite film porosity and thickness on the electrolyte ion penetrations into the deeper electroactive sites are revealed. In this part, the impedances of RC elements cannot be neglected. The charge transfer resistance R_{ct} is assigned to the resistance encountered by electrolyte ions when they penetrate into deeper site of the composite film. It is associated to the diameter of the depressed semicircle. The fitted values of R_{ct} along with R_s are shown in **Table 5.4**.

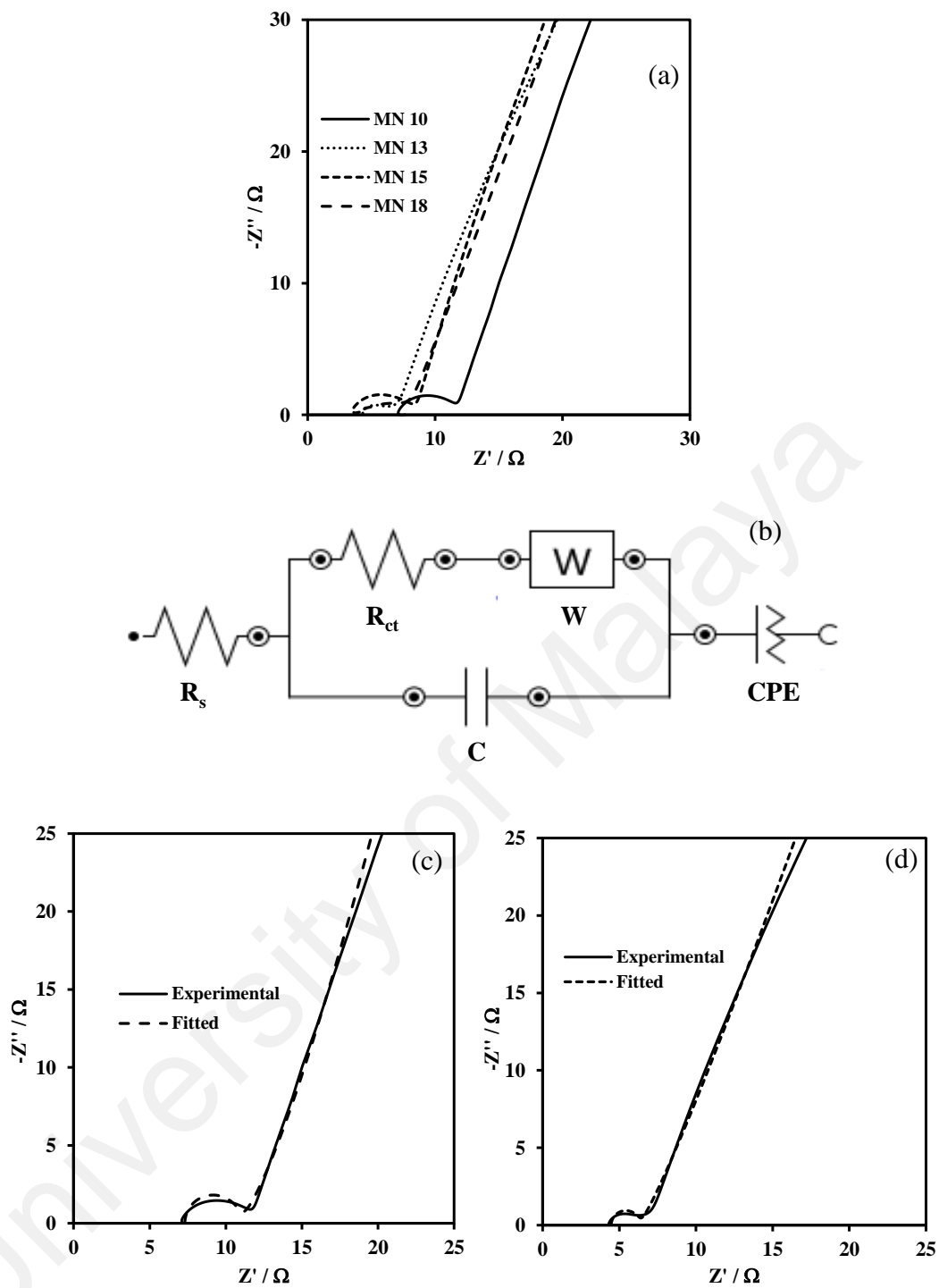


Figure 5.6: (a) Nyquist plots for composite film deposited at different durations, (b) corresponding equivalent circuit, and Nyquist plot with fitted impedance curves at different deposition durations: (c) 10 mins, (d) 13 mins, (e) 15 mins and (f) 18 mins.

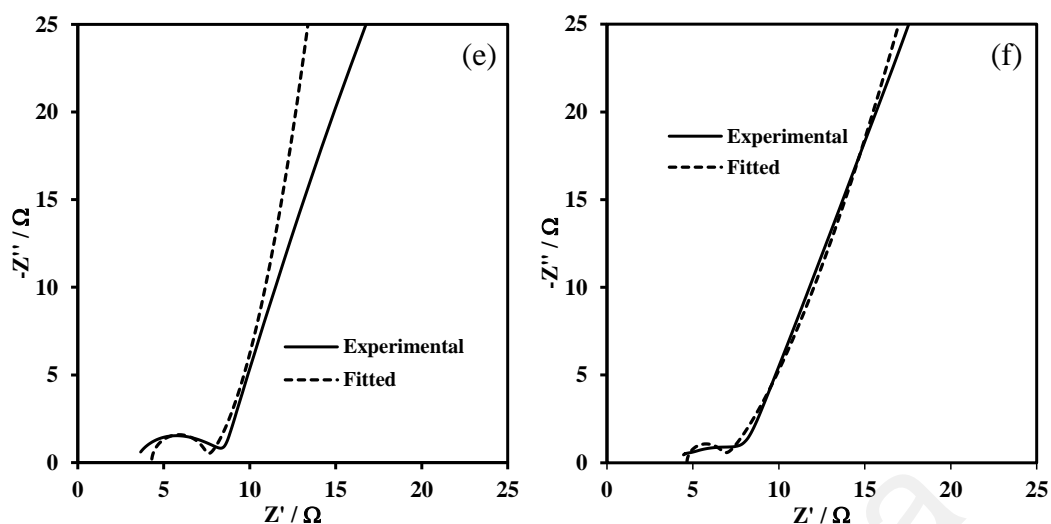


Figure 5.6: Continued.

Table 5.4: Fitted values of equivalent circuit components for Nyquist plots at different deposition duration.

Electrodeposition duration, t / mins	Ohmic resistance, R_s / Ω	Charge transfer resistance, R_{ct} / Ω
10	7.31	3.53
13	4.47	1.79
15	4.3	3.09
18	4.65	2.04

The 13 mins-deposited composite film is recognized to have the lowest R_{ct} . This can be accountable to the highest charge storage ability owned by this composite electrode. The capacitive element C_{dl} shows the presence of double layer capacitance in the composite electrode. It originates from the migration of charges at the outer surface of the film surface at high frequency. However, the formation of depressed semicircle implies the dominance of charge transfer reactions over the double layer capacitance for charge storage process. This charge transfer reaction is diffusion controlled as indicated by the presence of Warburg element W . At low frequency, RC elements has reached their maximum values and the impedance plot should exhibit as a vertical line. However, due to the non-ideal capacitive behaviour possessed by the composite film, a sloping straight line is observed. The constant phase element CPE is used to model this

behaviour. At the same time, it is accounted for the low frequency Faradaic impedance regarding to the inhomogeneity of the composite film.

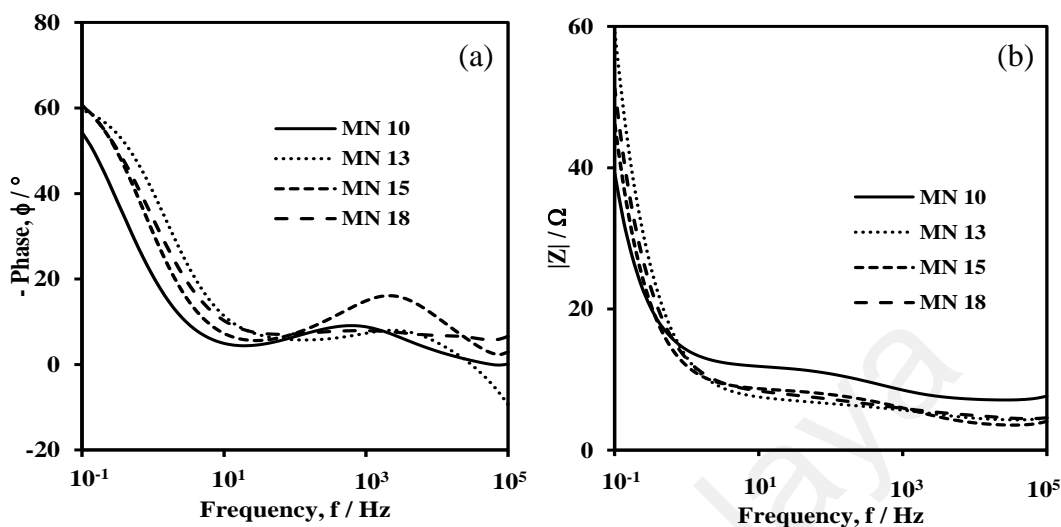


Figure 5.7: Bode plots of (a) phase angle versus frequency (in logarithmic scale) and (b) absolute impedance $|Z|$ versus frequency (in logarithmic scale).

Figure 5.7 (a) demonstrates the Bode plot of frequency dependence of phase angle Φ . Like the Nyquist plot, the Bode plot also can be divided into three region: high frequency, medium frequency and low frequency region. The phase angles are near zero at high frequency. The capacitor response frequency is the frequency when $|\Phi = 45^\circ|$. The higher frequency value signifies the better capacitive behaviour performed by an electrode. The frequency $f_{\Phi=45^\circ}$ ranges from 3 to 9 Hz for composite films deposited at different durations. The composite film deposited at 13 mins has the highest value of capacitor response frequency. This suggests that it has the best capacitive behaviour. On the other hand, the Faradaic pseudocapacitance is revealed by the $|\Phi_{0.1Hz} < 90^\circ|$ at low frequency. **Figure 5.7 (b)** displays the Bode plot of frequency dependence of absolute impedance $|Z|$. The plot exhibits a slope near to -1 at low frequency region, indicating the typical capacitive behaviour.

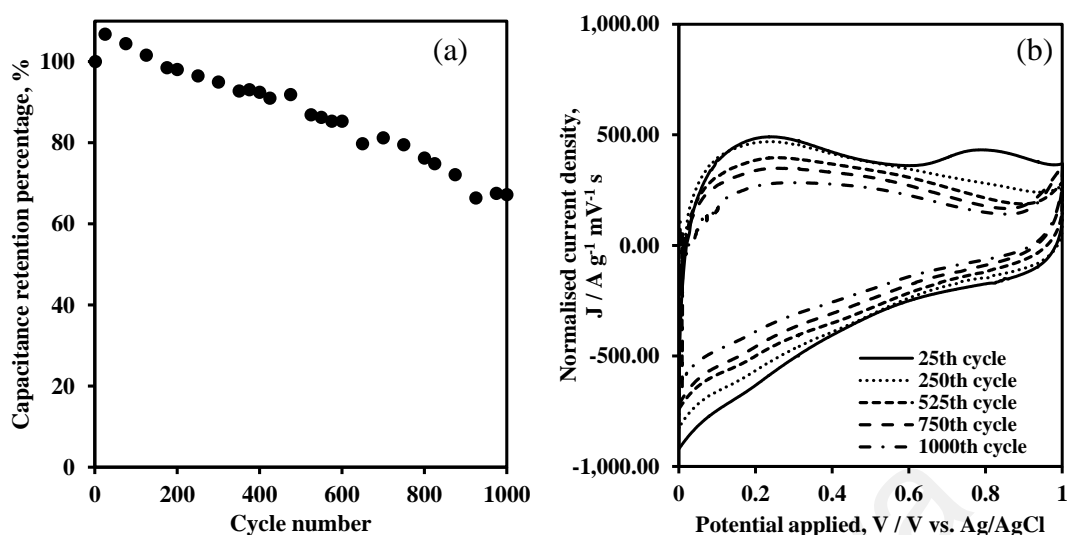


Figure 5.8: (a) Capacitance retention test of 13 mins-deposited composite film for 1000 cycles at 10 mV s^{-1} and (b) CV curves at different cycle numbers.

Figure 5.8 (a) shows the capacitance retention test result over 1000 cycles for the 13 mins-deposited composite film. The specific capacitance is increased during the initial cycling as indicated by the incremental capacitance retention percentage in the beginning. This is caused by the activation process occurred on the composite film. During the initial cycling, the activation process opens up more electroactive sites on the composite film. This increases the occurrence of redox reactions which then results in higher specific capacitance. However, the specific capacitance reduced gradually after that. This composite film can retain 67 % of the original capacitance over 1000 cycles. The CV curves at different cycle numbers are exhibited in **Figure 5.8 (b)**. The change in CV shapes from 25th to 250th cycle is noticeable. The oxidation peak is vanished at 250th cycle. It can be attributed to the chemical degradation and partial dissolution of films upon cycling (Pang et al., 2000). However, the further cycling (250th to 1000th) has only caused the net loss in CV areas without significant alterations in CV shapes. This kind of changes is believed to be induced by the further dissolution of composite film.

5.6 Summary

- The electrodeposition of manganese-nickel oxide film has been carried out in a bath containing manganese acetate and nickel acetate.
- The composite film formed is amorphous in nature regardless of the deposition duration. There is no specific diffraction peaks regarding to either manganese oxide or nickel oxide being detected. Hence, the components are expected to exist in the form of composite.
- The morphological and microstructural studies revealed the spongy-like structures of all composite films deposited at various durations. The homogeneity of 13 mins-deposited composite film was observed. The uniformity of this composite film offers the lowest charge transfer resistance and increases the opportunity for the redox reactions between electrolyte ions and electroactive sites on the film. It also has the behaviour closest to the ideal capacitor as suggested by Bode plot.
- 13 mins-deposited composite film has achieved the highest specific capacitance (404 F g^{-1}). It preserved 67 % of the initial capacitance after 1000 cycles. The degradation of the capacitance can be caused by the dissolution of films upon cycling. This study proves that amorphous composite film also can exhibit good electrochemical performance.

CHAPTER 6: CHARACTERISATIONS OF MANGANESE OXIDE-PEDOT: PSS COMPOSITE ELECTRODE SYSTEM

6.1 Introduction

As a redox material, the conducting polymer is widely studied as an electrode material employed in supercapacitor application. Unlike transition metal oxide, the charge transfer reactions occur through the volume of the conducting polymer (Rudge et al., 1994). In other words, conducting polymer-based supercapacitor is capable to achieve higher energy density. The electronic conductivity of conducting polymer was firstly reported in 1963 (Bolto et al., 1963). However, the application of conducting polymer is limited by its stability because the conductivity must be practically not influenced when it is heated at 120 °C over 1000 hours (Heywang & Jonas, 1992). Since then, many efforts have been spared to develop conducting polymer-based product which is low-cost and stable for application.

The poly (3, 4-ethylenedioxythiophene) (PEDOT) is a promising electrode material for supercapacitor. Although it was found to be insoluble initially, it is high in conductivity (ca. 200 S cm⁻¹) and stability in thin oxidised film (Kvarnström et al., 1999; Pei et al., 1994). The insolubility drawback has been overcome by combining PEDOT with water-soluble poly (styrene sulfonic acid) (PSS) to form PEDOT: PSS. The PEDOT: PSS film can undergo heating of 100 °C in air over 1000 hours without dramatic change in conductivity (Groenendaal, 2000). Hence, the integration of PEDOT: PSS with manganese oxide is expected to improve the conductivity of the manganese oxide. In one-step deposition, manganese oxide and PEDOT: PSS were deposited onto stainless steel under galvanostatic control that is 2 mA cm⁻². The characterisation results are shown in the following section.

6.2 Field emission scanning electron microscopy (FESEM)

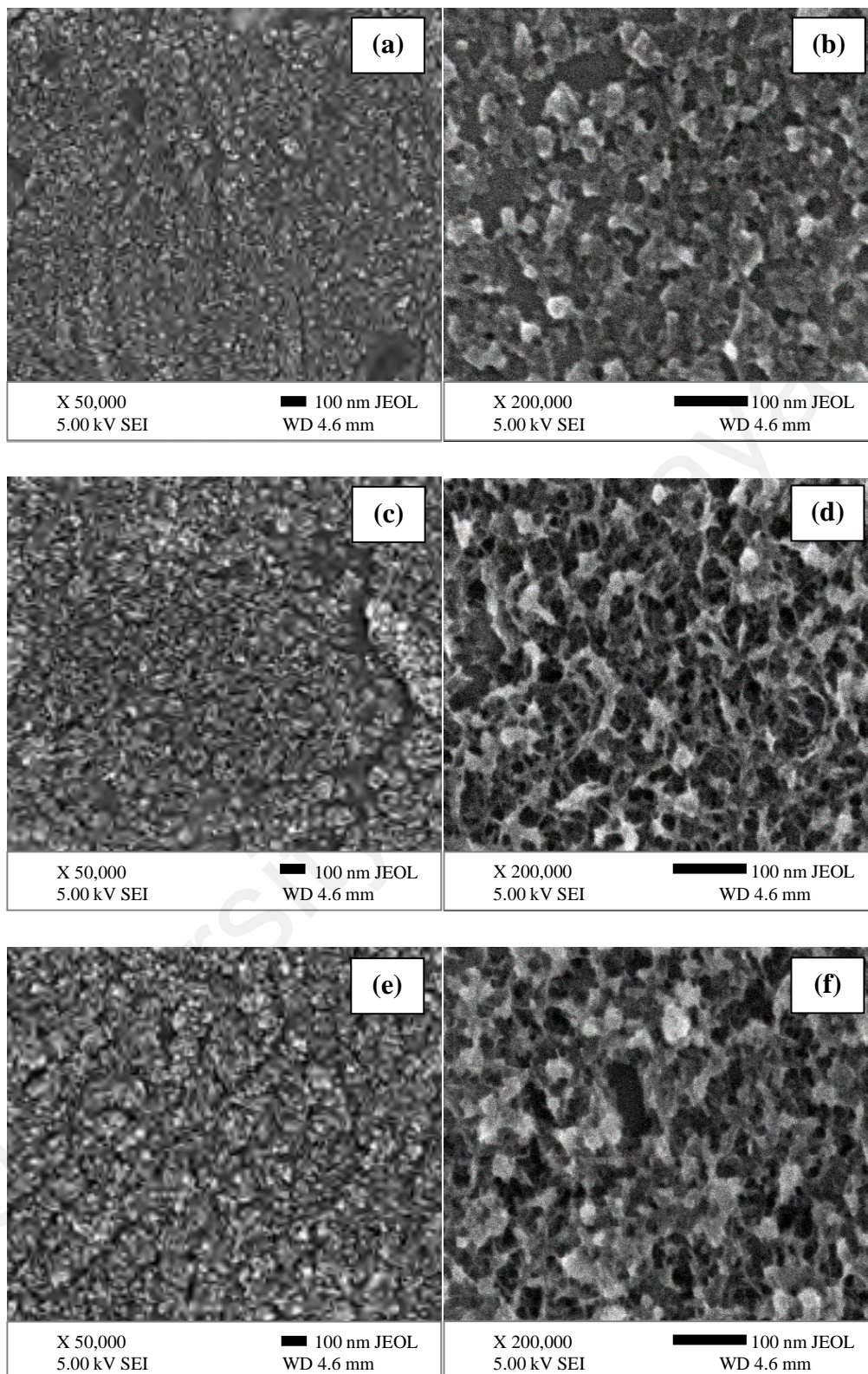


Figure 6.1: Morphologies of composite films deposited at different durations: (a, b) 10 s, (c, d) 20 s, (e, f) 30 s, (g, h) 40 s and (i, j) 50 s.

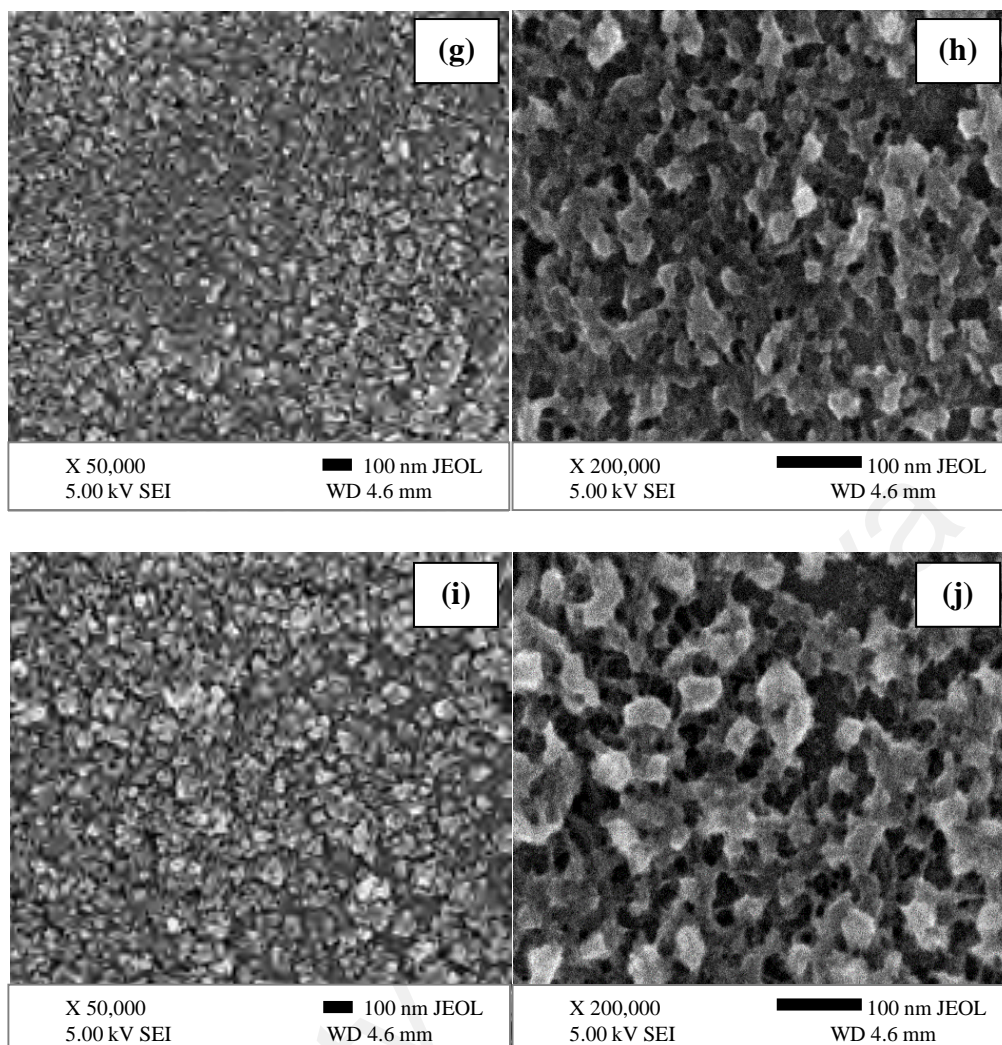


Figure 6.1: Continued.

In the solution containing PEDOT: PSS and Mn^{2+} , PEDOT: PSS and Mn^{2+} incorporate through electrostatic interaction and attach on the stainless steel to form a composite film. **Figure 6.1** shows the FESEM images of manganese oxide-PEDOT: PSS composite film deposited at various duration in 50k and 200k of magnifications. As shown, the morphology becomes rougher with longer deposition duration. The images obtained at higher magnification present the changes in particles with deposition duration. The particle size grows when the deposition extends from 10 s to 50 s. At 10 s, the globular morphology is irregular and inhomogeneous. However, the changes is detected when the deposition duration increases to 20 s. The morphology transforms to be a fibrous structure that forms open pores which eases the ionic

transportation. Further accumulation of deposits resulted from longer deposition time has led to structure aggregation. The effect of this transformation of structure on electrochemical performance is investigated using cyclic voltammetry and galvanostatic charge-discharge.

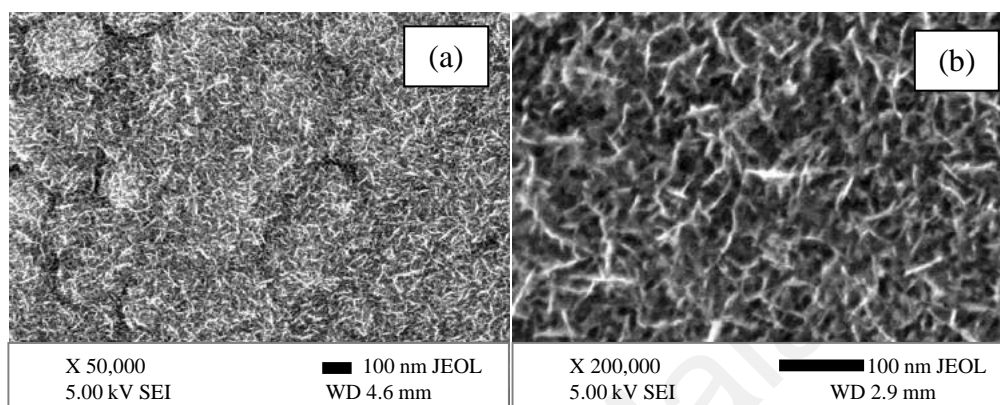


Figure 6.2: FESEM images of manganese oxide deposited at 40 s without PEDOT: PSS with magnification of (a) 50k and (b) 200k.

Figure 6.2 shows the morphology of manganese oxide film formed at 40 s of deposition without PEDOT: PSS. The images display a distinct structure compared with **Figure 6.1 (g)** and **(h)**. Without the addition of PEDOT: PSS, the film exhibits a flaky structure as shown at 200k of magnification, **Figure 6.2 (b)**. Lower magnification of 50k reveals the formation of bigger spherical structure, **Figure 6.2 (a)**. The formation of different morphologies directly indicate the influence of addition of PEDOT: PSS onto the structure. The morphology more likely to form a particle-like structure with the aids from PEDOT: PSS. On the other hand, manganese oxide film tends to form a flaky structure under the same experimental conditions. The effect of morphology on electrochemical performance of the film is evaluated in the following section.

6.3 Transmission electron microscopy (TEM)

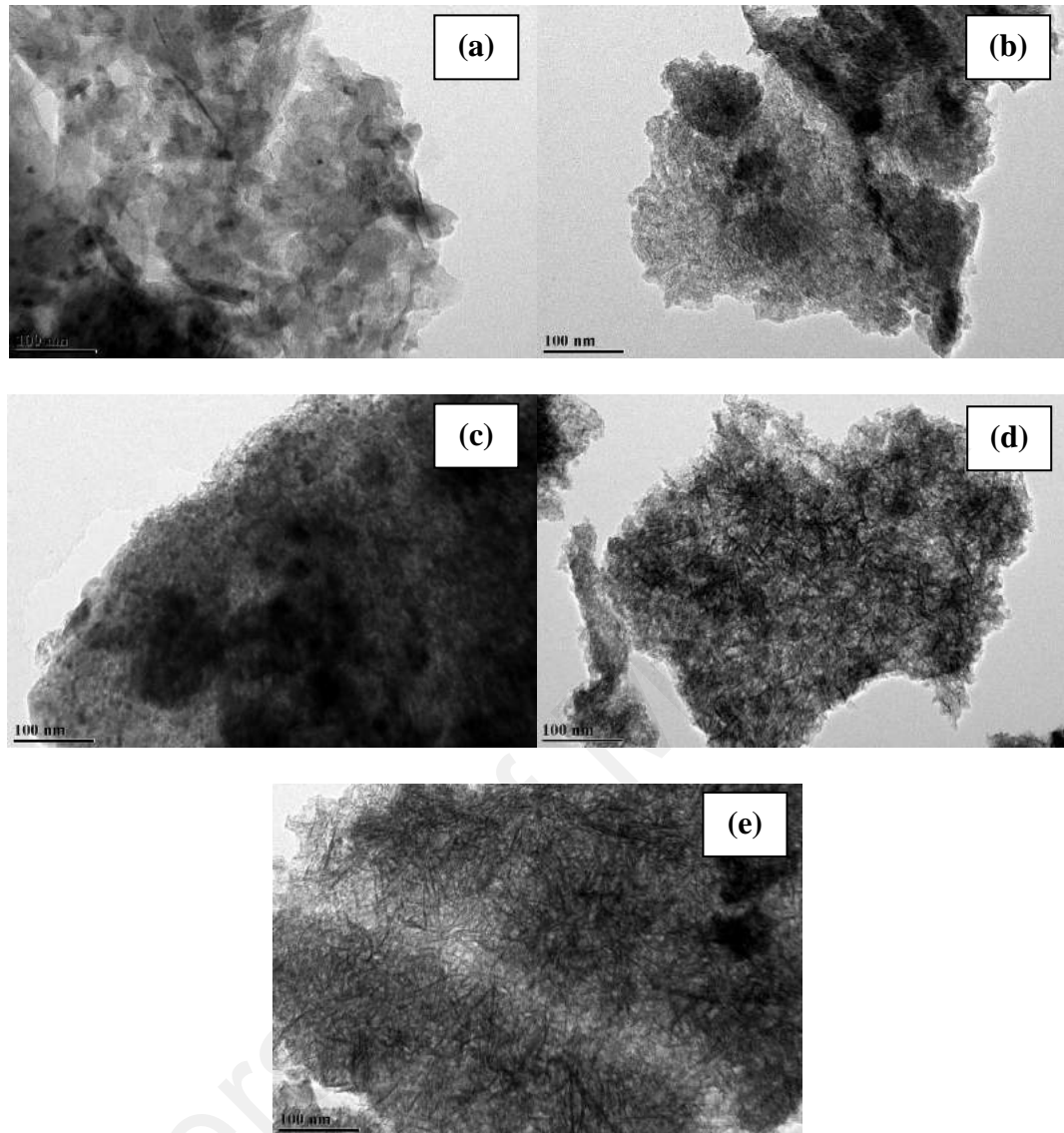


Figure 6.3: TEM images of composite film deposited at (a) 10 s, (b) 20 s, (c) 30 s, (d) 40 s and (e) 50s.

The composite film is scrapped from the stainless steel for microstructure examination. The result is displayed in **Figure 6.3**. In general, the composite films remain the assembly of structure as in FESEM after scrapping implying the good cohesiveness of the film. The darker region shows the aggregated part while brighter region relates to the porous section. **Figure 6.3 (a)** reveals the closed structure of 10 s-deposited composite film compared to other composite films. **Figure 6.3 (c) and (d)**

clearly show the porous structure owned by composite film deposited at 40 s and 50 s respectively.

6.4 X-ray diffraction (XRD)

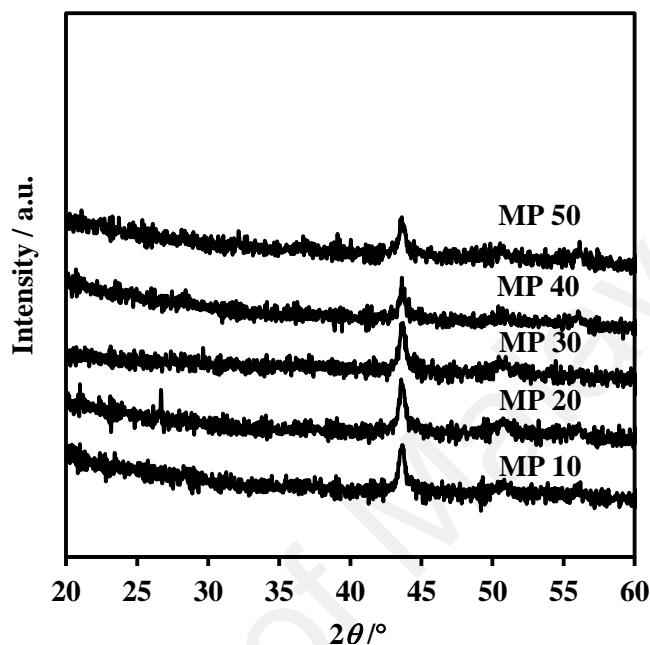


Figure 6.4: XRD patterns of composite films deposited at various duration.

All films exhibit to be amorphous as shown in **Figure 6.4**. This is expected since most of the films prepared using electrodeposition method show amorphousness. On the other hand, the composite film in this study was annealed at relatively low temperature that is 60°C . It has been shown that manganese oxide annealed up to 400°C will still present as amorphous. The amorphousness will transform to more crystalline when the annealing temperature reaches temperature of 500°C and above (Kandalkar et al., 2011; McNally et al., 2005). There is no significant changes detected between the XRD patterns. This implies that the variation of deposition duration does not notably alter the structure of the composite film given the condition that they are annealed at same temperature. Furthermore, a small sharp peak at about 43° is noticed in all diffractograms. However, due to the weak crystallinity, the crystal structure and the peak are unable to be recognised and resolved.

6.5 Cyclic voltammetry (CV)

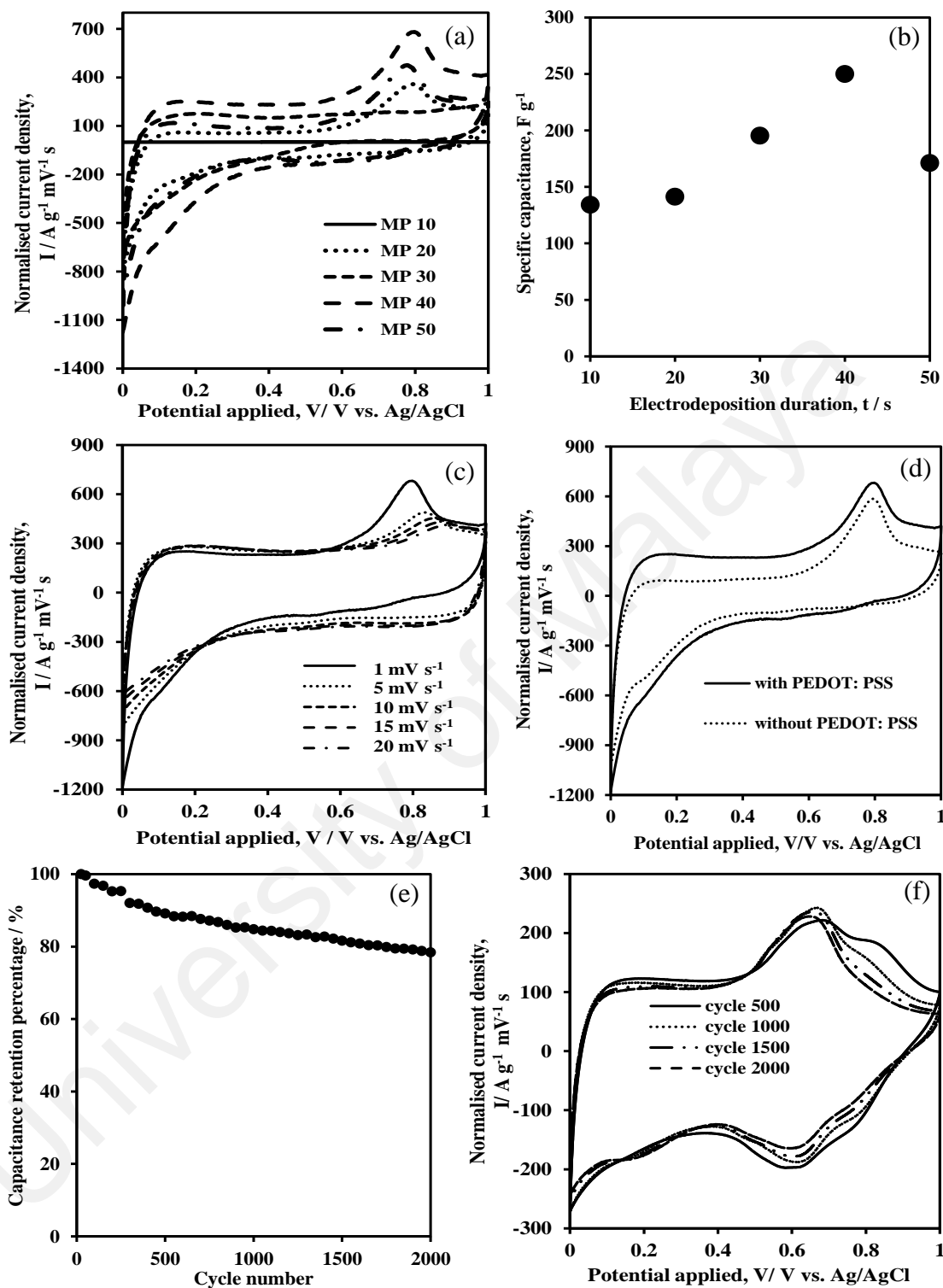


Figure 6.5: (a) Cyclic voltammetry curves of composite electrode at various deposition durations at 1 mV s⁻¹, (b) relationship between specific capacitance and deposition duration, (c) cyclic voltammetry curves of MP 40 at different scan rates, (d) comparison of cyclic voltammetry curves between film with and without PEDOT: PSS, (e) cycle stability test and (f) cyclic voltammetry curves at different cycles during stability test.

Figure 6.5 (a) depicts the cyclic voltammetry curves for composite electrode prepared at different deposition durations in a potential window of 0 to 1 V at 1 mV s^{-1} . A redox peak is clearly seen from the figure. From **Figure 6.5 (d)**, the redox peak can be assigned to the redox activity occurred on manganese oxide as the peak is still clearly shown when the film is prepared without PEDOT: PSS. The discharging curves are used to evaluate the specific capacitances obtained at different deposition durations. The estimated specific capacitances are 134 F g^{-1} , 141 F g^{-1} , 195 F g^{-1} , 250 F g^{-1} and 171 F g^{-1} for 10 s, 20 s, 30 s, 40 s and 50 s respectively. The results are displayed in **Figure 6.5 (b)**. The specific capacitance increases gradually with the deposition durations until 40 s of deposition duration. The specific capacitance is shown decreased as much as 31.6 % for composite electrode deposited at 50 s. This can be caused by the bulk structure resulted from the accumulation and aggregation of deposits which can inhibit the ionic transportation. As 40 s-deposited composite electrode obtains the highest specific capacitance, its capacitive behaviour is further studied by varying the scan rate.

The corresponding relationship between electrochemical performance and scan rate is illustrated in **Figure 6.5 (c)**. The overall cyclic voltammetry curves are similar for all scan rates, which is rectangular shape of curve accompanied with a redox peak. A small shift of redox peak is observed for scan rates of 5, 10, 15 and 20 mV s^{-1} . Besides, the curve exhibits to be more rectangular compared to curve at 1 mV s^{-1} . This shows that the charge transfer reactions are took place more often through insertion/de-insertion processes at relatively low scan rate of 1 mV s^{-1} . In other words, the reaction is diffusion-controlled. At higher scan rate, the charge transfer reactions are limited on the surface of the composite film. This also leads to the decreasing of specific capacitance with the increasing of scan rate.

Figure 6.5 (d) displays the cyclic voltammetry curves of manganese oxide film with and without PEDOT: PSS. The redox peak is observed on both curves. Thus, it can be attributed to the redox activity occurs on manganese oxide. The cyclic voltammetry curve for film with PEDOT: PSS is observed to be larger compared to the one without PEDOT: PSS. The specific capacitance is enhanced for around 30 % when the PEDOT: PSS is integrated with manganese oxide, which is increased from around 193 to 250 F g⁻¹. The addition of PEDOT: PSS is found not to greatly improve the achievable specific capacitance. Instead of offering more charge storage sites, PEDOT: PSS provides a conductive pathway for ionic and electronic transportation through the SO₃H groups in PSS (Liu, 2008).

In order to examine the redox activity of the film along with the cycle stability, the 40 s-deposited composite electrode is tested in 1 M Na₂SO₄ at 10 mV s⁻¹ for 2000 cycles. The related capacitance retention percentage with cycle number is shown in **Figure 6.5 (e)**. After first 1000 cycles, the composite film is found to retain 84.8 % of original specific capacitance. The next 1000 cycles has led to the further decreasing in capacitance. The composite film retained 78.4 % after 2000 cycles. To investigate the redox activity during the stability test, the cyclic voltammetry curves at 500th, 1000th, 1500th and 2000th cycle are recorded and shown in **Figure 6.5 (f)**. The appearances of the curves are similar in general. The current density decreased slightly when the cycle numbers increased from 500th to 2000th. This shows the gradual decreasing in specific capacitance with the cycle numbers. The decline in the capacitance value can be caused by two aspects: (1) the dissolution of film during the cycling process and (2) the PEDOT: PSS cannot afford to sustain the repeated charging-discharging process. As repeated swelling and shrinking can lead to degradation of the conducting polymer, the PEDOT: PSS undergoes unavoidable deterioration during the cycling test (Antiohos et al., 2011). On the other hand, in overall, the capacitance retention of around 78 % after

2000 cycles is remarkable. This can be attributed to the interconnected structure of the film which supports the ionic and electronic transportation. On the other hand, the water content of manganese oxide is believed to have contributed to the good stability and specific capacitance of the film because the water plays important role in charge storage mechanism for manganese oxide (Chang et al., 2004; Toupin et al., 2004).

6.6 Galvanostatic charge-discharge (GCD)

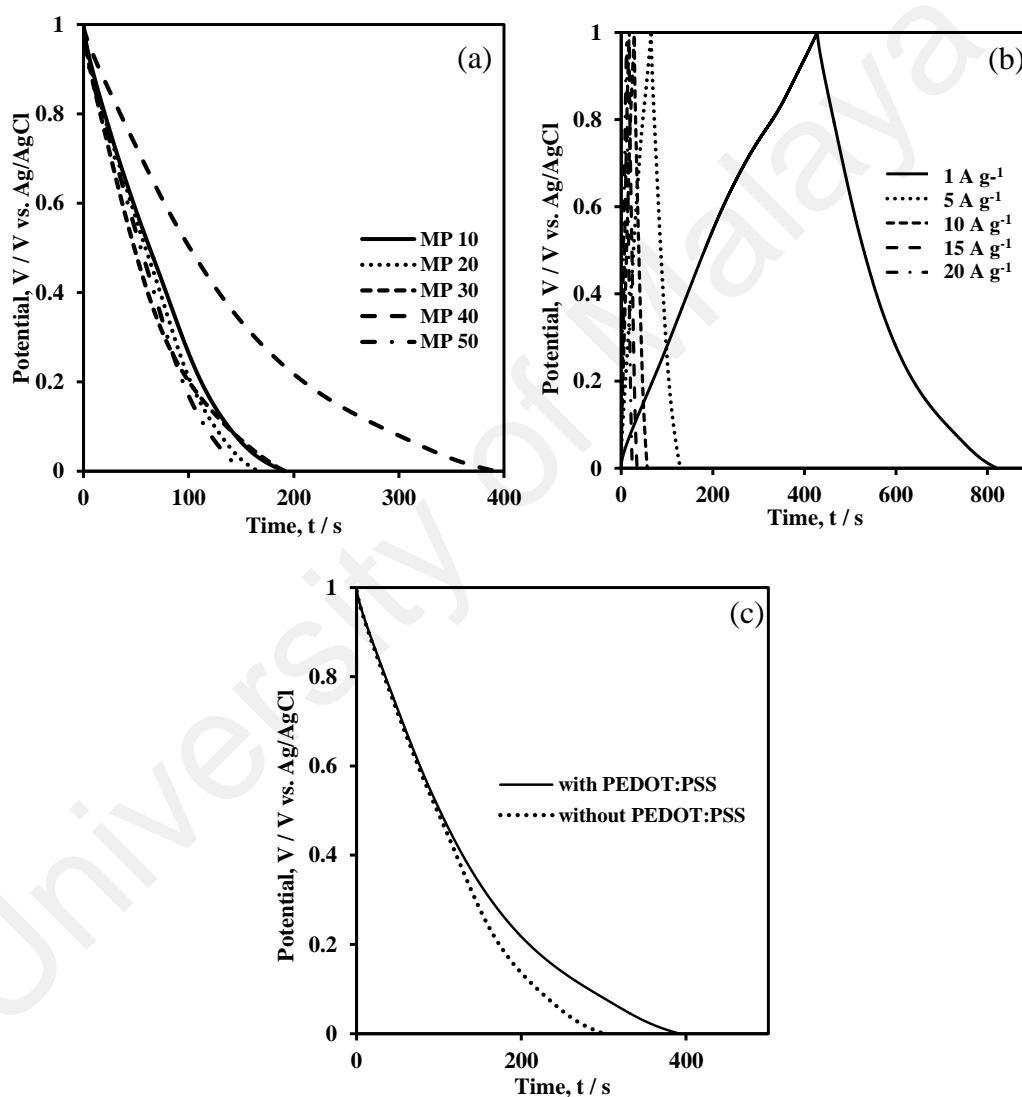


Figure 6.6: Galvanostatic (a) discharging curves of composite electrodes prepared at different deposition durations, (b) charge-discharge curves of 40-s deposited composite electrode at various current densities and (c) discharging curves of film with and without PEDOT:PSS.

The galvanostatic discharging curves of the electrodeposited composite films measured at 1 A g^{-1} in $1 \text{ M Na}_2\text{SO}_4$ are illustrated in **Figure 6.6 (a)**. The non-linearity of the curve indicates the participation of redox reactions in the composite film. The potential drops for all the curves have been measured. They are $6.7 \text{ m}\Omega$, $14.3 \text{ m}\Omega$, $15.6 \text{ m}\Omega$, $6.41 \text{ m}\Omega$ and $33.0 \text{ m}\Omega$ for 10, 20, 30, 40 and 50 s respectively. The potential drops are small for all composite films. Besides, the discharging curves shown has uncovered that 40 s-deposited composite film owns the highest charge storage. This result is consistent with the cyclic voltammetry test result. The specific capacitances at different deposition durations are derived from the discharging curves. The trend of the specific capacitance is similar to the one obtained from cyclic voltammetry at where the specific capacitance increases gradually from 10 s until 40 s and then drops when the deposition duration exceeds 40 s. The highest specific capacitance estimated is 394 F g^{-1} achieved by 40 s-deposited composite film. **Figure 6.6 (b)** depicts the galvanostatic charge-discharge profile of 40 s-deposited composite film at various current densities. The composite electrode shows the highest specific capacitance at 1 A g^{-1} and decreases with higher scan rate. However, the specific capacitance drops dramatically at 5 A g^{-1} and above. This indicates the low rate capability of this composite electrode. The enhancing effect on electrochemical performance due to the addition of PEDOT: PSS is shown in **Figure 6.6 (c)**. The little improvement on electrochemical performance contributed by the PEDOT: PSS is clearly noticed from this figure. It is again important to emphasise that PEDOT: PSS acts as conducting backbone instead of electroactive sites in this study.

6.7 Frequency response analysis (FRA)

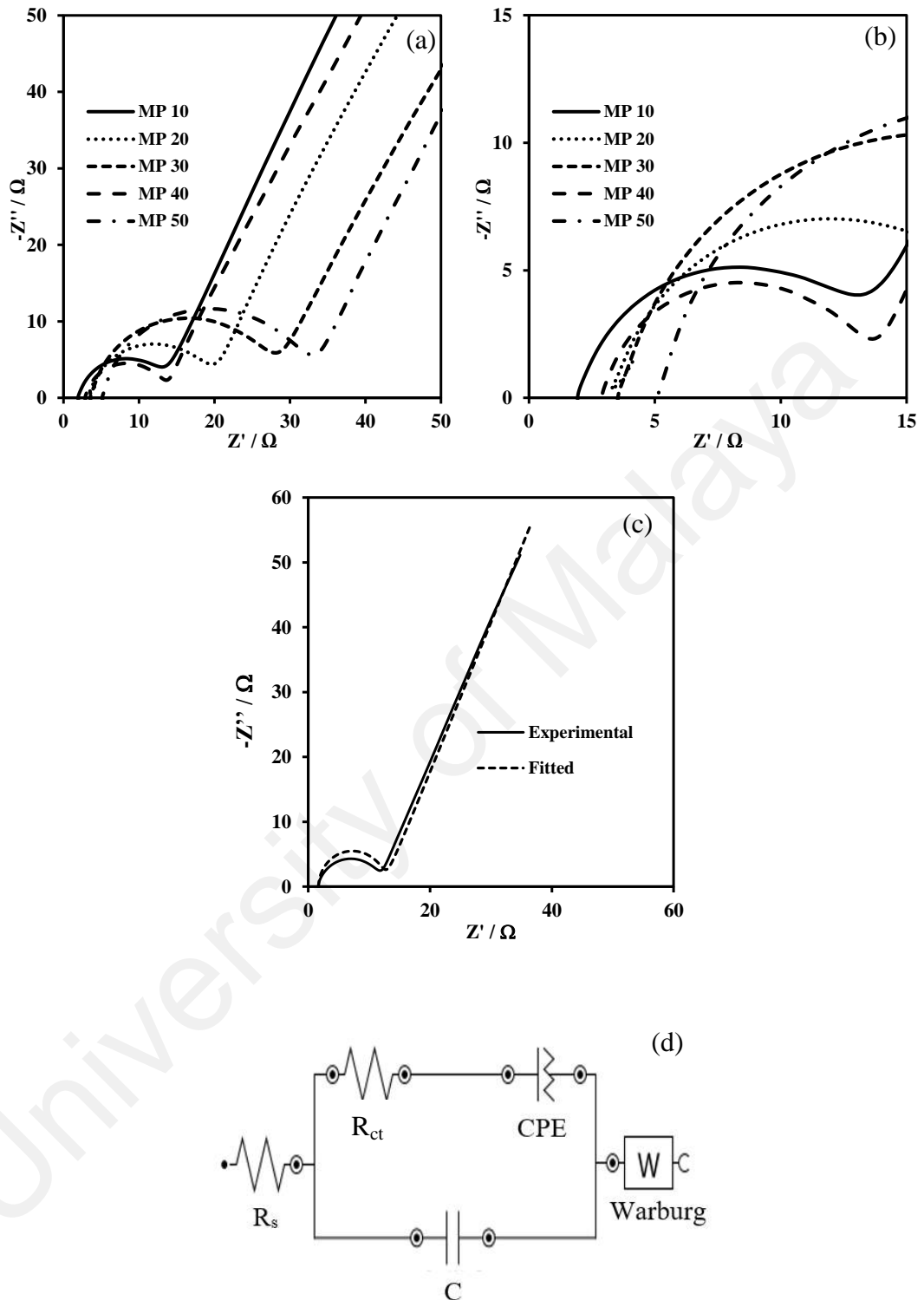


Figure 6.7: (a, b) Nyquist plots of the composite films deposited at different durations, (c) Nyquist plots of experimental and fitted data of 40 s-deposited composite electrode, (d) equivalent circuit of deposited composite film, Bode plots of (e) phase angle versus frequency (in logarithmic scale) and (f) absolute impedance $|Z|$ versus frequency (in logarithmic scale).

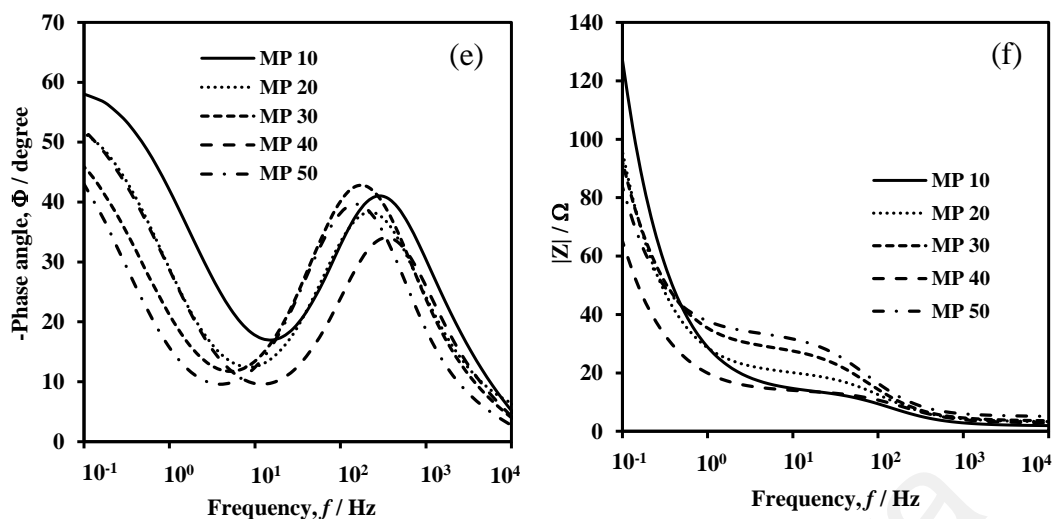


Figure 6.7: Continued.

The impedance spectrum (0.1 Hz to 100 kHz) displayed in **Figure 6.7 (a)** consists of: (a) x -intercept in high frequency region, (b) a depressed semicircle and (c) a sloping straight line. In high frequency region, the x -intercept represents the combinational resistances R_s encountered in the electrolyte, substrate, and at the film/substrate interface (Gamby et al., 2001). **Figure 6.7 (b)** reveals the position of x -intercept at high frequency region and a depressed semicircle that can be accounted as charge transfer resistance R_{ct} . It can be seen that the composite films prepared at different deposition durations exhibit different R_s and R_{ct} values. The overall resistance can be estimated by adding both R_s and R_{ct} . Thus, the resistances encountered by composite film deposited at 10, 20, 30, 40 and 50 s are 14.20, 14.15, 29.40, 14.00 and 34.40 Ω . It is noticeable that 40 s-deposited composite film possesses the lowest resistance. The relatively lower resistance explains the better ionic and electronic transportation inside this composite electrode.

The low frequency region in the impedance spectrum describes a sloping straight line which demonstrates the capacitive behaviour and the diffusion resistance encountered by the electrolyte ions. The ideal capacitor responds as a vertical straight line in low frequency region during impedance test. In other words, it is expected that the

composite electrode in this study should not exhibit a vertical straight line in low frequency region as the composite is made up from redox materials. Apart from this reason, the formation of deviated straight line can also be contributed by the uneven porous structure of the film (Gamby et al., 2001).

The impedance spectrum of the composite film has been analysed further using equivalent circuit model carried out by Nova 1.10. **Figure 6.7 (c)** displays the combination plot of fitted and experimental impedance data of 40 s-deposited composite film. The corresponding equivalent circuit is illustrated in **Figure 6.7 (d)**. This circuit is found to fit the most and the circuit proposed is reasonable. The equivalent circuit is composed of solution resistance R_s , parallel resistance or charge transfer resistance R_{ct} , constant phase elements CPE , capacitive element C and finite length Warburg impedance element W . The R_s corresponds to the x -intercept in high frequency region as explained before. The depressed semicircle is described by R_{ct} , CPE and C . As a capacitive element, C uncovers the participation of double layer capacitance in the composite film. At the same time, the presence of CPE indicates the non-ideal capacitive behaviour possessed since pseudocapacitance behaviour is dominant in this composite film. The W element refers to the diffusion resistance and the highly distributed capacitance within the hydrous manganese oxide inside the composite film.

Figure 6.7 (e) and **(f)** present the Bode plots. **Figure 6.7 (e)** shows the frequency-dependence of phase angle Φ . The Bode plot of phase angle can be related to Nyquist plot by examining the absolute phase angle. The absolute phase angle is found to deviate from 90° which is in other words, $|\Phi_{0.1Hz} < 90^\circ|$. This verifies the sloping straight line in the low frequency region of Nyquist plot, which is also an indication of Faradaic pseudocapacitance (Ding et al., 2013). The frequency when $|\Phi = 45^\circ|$ is named as capacitor response frequency. A better capacitive behaviour will be exhibited by

higher value of frequency (Sugimoto et al., 2005). In this study, the $f_{\Phi=-45^\circ}$ ranges from 0.1 to 0.7 Hz for composite film deposited at 10 to 50 s. On the other hand, the capacitive behaviour is also shown through Bode plot of absolute impedance $|Z|$, **Figure 6.7 (f)**. The presence of capacitive behaviour is revealed by the slope near to -1 at low frequency region in the spectrum.

6.8 Summary

- A manganese oxide-PEDOT:PSS composite film was prepared using electrodeposition technique in this study.
- The composite film formed was amorphous in nature and remained the amorphousness throughout the different deposition durations.
- The morphology was found to evolve from globular to fibrous structure with longer deposition duration.
- The electrochemical tests revealed that 40 s-deposited composite film achieved the highest specific capacitance of 250 F g^{-1} at 1 mV s^{-1} and 394 F g^{-1} at 1 A g^{-1} . It has the lowest total resistance and a good cycle stability at where it retained 78.4 % of initial specific capacitance after 2000 cycles.

CHAPTER 7: DISCUSSIONS

Due to its environmental benign, low-cost and natural abundance, the manganese oxide is one of the most promising electrode materials. It can exist in various form of oxides such as MnO , MnO_2 , Mn_3O_4 and Mn_2O_3 . There are different approaches to fabricate manganese oxide for example hydrothermal, sol-gel and chemical bath deposition (Aref & Tang, 2014; Chen et al., 2009; Qiu et al., 2011). Due to the morphology-dependent behaviour, the electrochemical performance of manganese oxide-based film can be determined by the preparation method. In this thesis, the manganese oxide acts as the primary material. It was compositing with carbon material, secondary transition metal oxide and conducting polymer to produce three types of hybrid electrode materials. The composite electrodes prepared are reduced graphite oxide (RGO)-manganese oxide, manganese-nickel oxide and manganese oxide-PEDOT: PSS composite electrode which named as RM, MN and MP, respectively. All the samples are prepared using electrodeposition method. The approach employed to carry out electrodeposition is chronopotentiometry technique. Hence, it is essential to present a plausible deposition mechanism for the composite electrodes in this study. Before we proceed to the deposition mechanism, there are some assumptions should be made: (1) the concentration of reactants is not varied with distance from the electrode surface before electrolysis and (2) the mass transport is determined by the linear diffusion based on the concentration gradient (Paunovic, 1967). The deposition mechanism is illustrated in **Figure 7.1**.

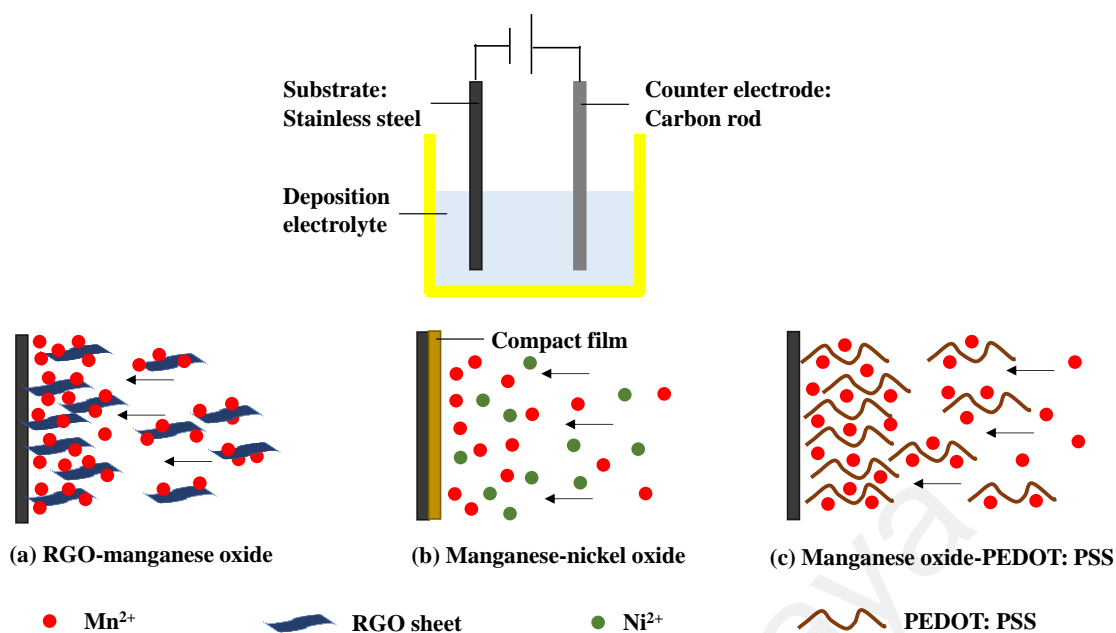


Figure 7.1: Deposition mechanisms of (a) RGO-manganese oxide, (b) manganese-nickel oxide and (c) manganese oxide-PEDOT: PSS.

Before the electrodeposition takes place, the equilibrium is reached as $O + ne^- \rightleftharpoons R$ at which O and R represents the reactant and product deposited respectively. As the reaction starts, $O + ne^- \rightarrow R$, the reactants at the electrode surface are consumed and reduced. A concentration gradient is arose due to the depletion of reactants. Consequently, the linear diffusion is promoted and in turns encourages the mass transport. In overall, the proposed mechanism following is made by considering the participation of semi-infinite linear diffusion with the usage of a planar electrode (which is stainless steel in this thesis) in an unstirred electrolyte.

The deposition mechanism of manganese oxide has been studied extensively (Biswal et al., 2015; Clarke et al., 2006; Fleischmann et al., 1962). In general, the deposition mechanism of manganese oxide involves the initial oxidation of manganese ions, adsorption and precipitation to solid phase, and dehydration process to form manganese oxide (Clarke et al., 2006). To understand the deposition mechanism of manganese oxide-based composite film, it is essential to realise the reactant species in the deposition electrolyte. As the manganese (II) acetate tetrahydrate was used throughout

the thesis, the Mn^{2+} ion was participated in the deposition process. Based on the reaction mechanisms proposed by previous studies (Reaction 7.1 to 7.4), the deposition mechanisms of composite electrodes in this thesis are thus suggested (Kao & Weibel, 1992; Paul & Cartwright, 1986).



As shown above, the adsorbed Mn^{2+} will transform into intermediate Mn^{3+} . At neutral or low acidic medium, the intermediate reacts with water molecule and forms MnOOH. The MnOOH is then oxidized to be MnO_2 after treated with appropriate annealing temperature.

For RGO-manganese oxide composite electrode (Chapter 4), the formation process can be described as following. The basal plane of RGO consists of epoxy and hydroxyl groups while the edges are decorated with carbonyl and carboxyl groups. These functional groups can interact with ions and form composite. Thus, Mn^{2+} ions produced from the dissolution of $\text{Mn}(\text{CH}_3\text{COO})_2 \cdot 4\text{H}_2\text{O}$ can form bond with the oxygen functional groups on the RGO via electrostatic interaction (Chen et al., 2010). In overall, the formation of RGO-manganese oxide is initiated by the anchor of manganese ions on the edge or defect sites of RGO (Lee et al., 2014).

In the case of manganese-nickel oxide composite electrode (Chapter 5), it can be explained via common deposition route. The manganese and nickel ions dissociate from their salts then precipitate onto the stainless steel, as described in Reaction 7.1 to 7.3.

After that, the deposited composite films will be transformed into oxide under the heat treatment of 300 °C (Ezema et al., 2008; Shinomiya et al., 2006).

On the other hand, the formation of manganese oxide-PEDOT: PSS involves the electrostatic interaction (Chapter 6) (Su et al., 2013). As the composite electrode undergoes annealing temperature of 60 °C, the manganese oxide formed still contain large portion of water as there is only small amount of water lost even at 120 °C. The water content in this composite electrode plays important role in its electrochemical performance and it has been shown in Chapter 6.

As the electrodeposition being employed as the preparation method, the relationship between deposition duration and the formation of composite film is studied. RGO-manganese oxide composite electrode was initially exhibited irregular morphology when the deposition duration is only 10 mins, **Figure 4.2**. However, the composite film has fully covered on the stainless steel surface though the resulted morphology is non-uniform. Additionally, the deposited composite film is compact and non-porous which does not offer a good ionic and electronic transportation pathway. When there is more ions deposited onto the film, the interaction between ions is dominant compared to the attraction between substrate and ions. This is shown by the transformation of morphology from irregular to flaky structure, **Figure 4.3**. At even longer deposition duration (15 and 18 mins), the ions accumulated on the flakes and then further agglomerated to form cluster-like structure. The mass per area for composite film deposited at 13, 15, and 18 mins are 4.6×10^{-5} , 6.0×10^{-5} and 2.6×10^{-4} g cm⁻². The addition in mass per area with deposition duration indicating that the film are still adhered well on substrate after exposed to 18 mins of deposition duration. The morphology that led to the highest specific capacitance was produced by 13 mins of electrodeposition duration.

For manganese-nickel oxide composite electrode, the morphology does not varied with deposition duration, **Figure 5.1**. The deposited ions are accumulated and continued to grow randomly on the deposits formed before them. There is no further significant interaction between deposits that causes the evolution of morphology or structure. Similar to RGO-manganese oxide composite electrode, 13 mins appears to be the optimum electrodeposition duration to produce the best electrochemical performance for this composite electrode system. In contrast, the evolution of morphology is observable for manganese oxide-PEDOT: PSS composite electrode, **Figure 6.1**. The morphology transforms from flaky to globular structure with longer deposition duration, 20 s to 50 s. Different from RGO-manganese oxide, the structure is agglomerated and formed nodes connecting with each other. Although the morphologies are porous, the porosity test is unable to be carried out due to the low-yield production for each deposited samples.

In overall, all composite electrodes revealed the formation of continuous coating on the substrate. The formation of different morphology is determined by the interaction type between different materials. Although morphology formed is different, all composite films are amorphous in nature, as examined by XRD. Hence, the empirical formula cannot be deduced for the composite formed in this thesis. The amorphousness, or structural disorderness, does not prohibit an efficient electronic and ionic transportation. Instead, all composite electrodes display a good electrochemical performance. In RM, MN, and MP composite electrode systems, the optimum deposition durations are 13 mins, 13 mins, and 40 s respectively. The result is summarised in **Table 7.1**. As shown in **Table 7.1**, MN 13 with spongy-like structure achieved the highest specific capacitance, 404 F g^{-1} in 1 mV s^{-1} and 670 F g^{-1} in 1 A g^{-1} . This can be attributed to the relatively low charge transfer resistance R_{ct} of 1.79Ω of this composite electrode. On the other hand, RM 13 and MP 40 have R_{ct} of 2.4Ω and

11.4 Ω respectively. The relatively higher R_{ct} of MP 40 also led to the lowest specific capacitance obtained.

Table 7.1: Comparison study on three composite electrode systems.

Composite system	Specific capacitance / F g ⁻¹		Capacitance retention percentage % after 1000 cycles
	Cyclic voltammetry at 1 mV s ⁻¹	Galvanostatic charge-discharge at 1 A g ⁻¹	
RM 13	407	498	78.0
MN 13	404	670	67.0
MP 40	250	394	84.8

The CV curves appear to be a little bit different from each systems. Generally, the CV curve has a rectangular envelope. RM and MN systems have a broad hump while MP system has an obvious redox peak. MN system is observed to have broader hump compared to RM system. The appearance of redox peak is an indication of the insertion/de-insertion processes. The presence of broad hump in CV curves of RM and MN composite electrode systems indicate the more distributive of the charge transfer reactions. In contrast, the prominent redox peak of MP system shows the metal-centred property of the composite film. The CV curve can be explained via band theory as well (Bard & Faulkner, 2001). Based on band theory, the rectangular CV curve is generated by the near and interactive redox active sites. The redox active sites with short separation distance can interact with each other and therefore create a wide range of energy states. In contrast, a well-separated and non-interactive redox active sites will possess similar energy states. This results in peak-shaped CV curve. From here, we can deduce that the redox active sites in RM and MN composite electrode systems have shorter separation gaps compared with redox active sites in MP composite electrode system.

The galvanostatic charge-discharge curves and impedance spectrum are found similar among these three systems. The galvanostatic charge-discharge curve exhibits

non-linearity indicating the participation of Faradaic reactions. On the other hand, the impedance spectrum show a combination of depressed semicircle and sloping straight line. The detailed evaluation has been explained in each section.

In terms of cycle stability upon 1000 cycles, MP 40 performs the best cycle stability compared with RM 13 and MN 13. MP 40 can retain 84.8 % of initial capacitance while RM 13 and MN 13 retains only 78 % and 67 % respectively. Even after 2000 cycles, MP 40 still able to retain 78 % of initial capacitance. This good cycle stability can be credited to the conductive backbone of conducting polymer, which is PEDOT: PSS in this system. The composite electrode system made up of only transition metal oxide exhibits even lower cycle stability, which is 67 % of initial capacitance after 1000 cycles. This can be caused by the lacking of supporting backbone and severe dissolution of deposited film. The dissolution of film is unavoidable during the cycling test. However, the effect is prominent when the film consists only transition metal oxide. For RM and MP systems, RGO and PEDOT: PSS act as supporter for manganese oxide. Nevertheless, MN only have transition metal oxides which contribute mainly to the charge storage process instead of stability. The corresponding CV curves of these three composite electrode systems can describe the redox activities on the composite films (**Figure 4.9 (b)**, **Figure 5.8 (b)**, and **Figure 6.5 (f)**). The redox peak of MP composite electrode system is clearly seen even at 1000th cycle while the redox activity in RM composite electrode system starts to diminish at 500th cycle. However, the redox activity in MN composite electrode system is merely seen start from 250th cycle. Since the MN composite electrode system consists only transition metal oxide, the lacking of conductive backbone affects the stability of the composite electrode upon repeated cycling process. On the other hand, RGO acts as the conductive backbone for the RM composite electrode system which brings about an intermediate performance between MN and MP composite electrode systems. From here, we can deduce that the

conductive backbone is important for cycle stability. This rises up a possibility of forming a better composite which consists of RGO, manganese oxide, nickel oxide and PEDOT: PSS. By combining the beneficial properties of each materials, this new composite is expected to achieve higher specific capacitance and cycle stability.

Our group has carried out an additional cohesiveness test to examine the adhesion strength and cohesiveness of the deposited film on the stainless steel. The half part of dried deposited film of RM 13, MN 13 and MP 40 are attached with transparent adhesive tape. Then, the tapes are removed at the same time. The surfaces are observed carefully and the images are shown in **Figure 7.2**.

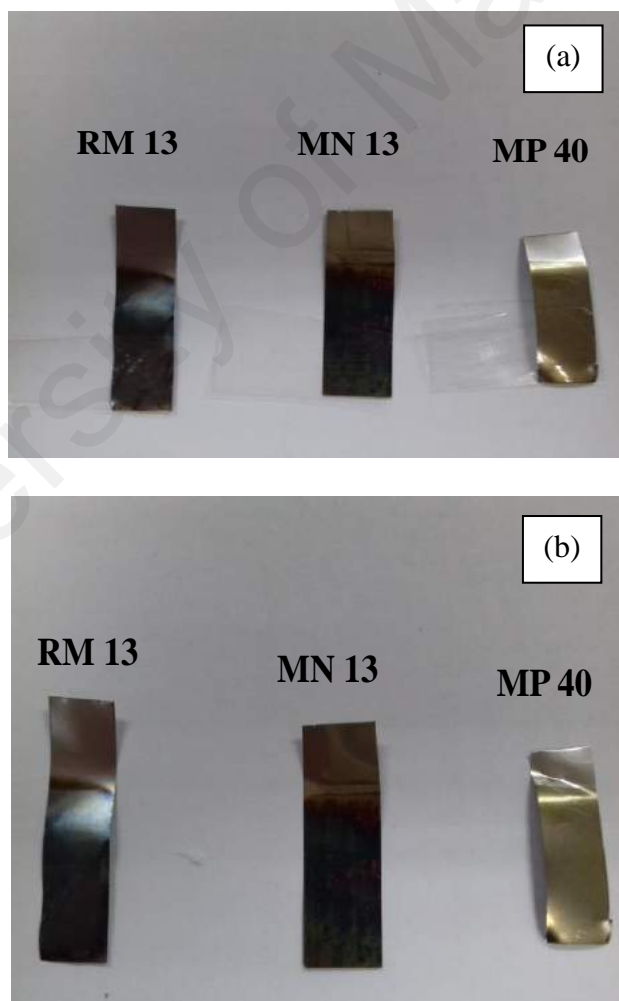


Figure 7.2: Images of composite electrodes (a) before and (b) after peeling off the adhesive tapes.

The result shows that all the composite films can resist the peeling force as they show insignificant detachment from the stainless steel. This suggests a good cohesion strength between the particles. In addition, there is nothing detected on the adhesive tape after being removed from composite electrode. This depicts a good adhesion between the composite film and stainless steel. The adhesion strength can be attributed to the van der Waals force which keep the composite film attached on the stainless steel during the peeling process of adhesive tape. The bonding between stainless steel and composite films studied is shown to be very good.

University of Malaya

CHAPTER 8: CONCLUSIONS AND SUGGESTIONS ON FUTURE WORK

8.1 Conclusion

In this work, the first objective was to fabricate and optimize three composite electrodes in terms of electrodeposition duration. By employing chronopotentiometry method, RGO-manganese oxide, manganese-nickel oxide and manganese oxide-PEDOT: PSS composite electrodes are prepared. The optimized electrodeposition durations for RGO-manganese oxide, manganese-nickel oxide and manganese oxide-PEDOT: PSS composite electrodes are 13 mins, 13 mins and 40 s respectively. This objective has been achieved.

The second objective was to examine the impacts of electrodeposition duration towards morphology and structure of prepared composite electrode. For RGO-manganese oxide composite electrode, the morphology was evolved with electrodeposition duration. The morphology grew from an irregular structure to a flaky structure when the electrodeposition duration was extended from 10 mins to 13 mins. Further increasing in electrodeposition duration resulted in a structure aggregation. However, electrodeposition duration did not affect significantly on the structure formed. The structure formed is amorphous in nature. This condition is similar to another two set of composite electrodes. For manganese-nickel oxide composite electrodes, all samples exhibited spongy-like morphology regardless of electrodeposition duration. Nonetheless, the morphology of manganese oxide-PEDOT: PSS composite electrode changed from globular to fiber-like structure. From here we can deduce that, due to different kind of interaction takes place when different types of materials are combined, the morphology formed can be varied. Therefore, this objective has been achieved.

The third objective was to study the electrochemical performances of the prepared composite electrodes. In overall, the electrochemical performance was inspected through cyclic voltammetry (CV) test, galvanostatic charge-discharge test (GCD), and impedance study. CV test was carried out by varying the scan rate in order to determine the predominant course that governs the charge storage process. The CV curves of three set of composite electrodes remained identical with the changing scan rate. This indicates that the diffusion process is governing the ionic transportation in the electrolyte. In addition, the charge storage process is mainly conducted by surface redox reaction. GCD test was performed in order to estimate the specific capacitance obtained by each composite electrodes. The specific capacitances obtained by RGO-manganese oxide, manganese-nickel oxide, and manganese oxide-PEDOT: PSS are 498, 670 and 394 F g⁻¹ respectively. This result is consistent with the impedance study that showed the lowest charge transfer resistance of manganese-nickel oxide composite electrode while manganese oxide-PEDOT: PSS had the highest charge transfer resistance. Combining all the electrochemical performance results, the third objective in this thesis is said to be accomplished.

The fourth objective was to demonstrate the cycle stability of the optimized composite electrodes upon 1000 cycles. The sequence of composite electrodes with cycle stabilities arranged in ascending order are manganese-nickel oxide, RGO-manganese oxide and manganese oxide-PEDOT: PSS. It can be seen that manganese oxide-nickel oxide does not possess the highest cycle stability although it has highest specific capacitance. This can be due to the lacking of supportive backbone like RGO and PEDOT: PSS, which makes this composite electrode suffered from metal oxide dissolution. On the other hand, compared with RGO, PEDOT: PSS acts as the stronger backbone for manganese oxide. It is therefore to say that the fourth objective in this thesis has been achieved.

8.2 Suggestions on future works

Future work may involve the preparation of composite consists of RGO, manganese oxide, nickel oxide, and PEDOT: PSS. The optimisation on the composite by varying the concentration, weight ratio, and annealing temperature can be carried out. However, the mass loading of the composite film must be taken care because thick film does not contribute to better electrochemical performance.

The electrode preparation method can be improved further. As chronopotentiometry technique is employed throughout the thesis, chronoamperometry may offer more information about the formation process of the film. Although electrodeposition is a green and simple method, the product formed usually appear as amorphous. By varying the annealing temperature, the crystallinity can be evolved. The effect on the electrochemical performance of the film can thus be evaluated by comparing with amorphous composite. The stainless steel is an inert substrate. Alternative substrate such as fluorine-doped tin oxide (FTO) glass or indium tin oxide (ITO) glass which are conducting substrate can be a good attempt.

REFERENCES

- Acerce, M., Voiry, D., & Chhowalla, M. (2015). Metallic 1T phase MoS₂ nanosheets as supercapacitor electrode materials. *Nature nanotechnology*, *10*(4), 313-318.
- Allen, M. J., Tung, V. C., & Kaner, R. B. (2010). Honeycomb carbon: A review of graphene. *Chemical Reviews*, *110*(1), 132-145.
- Anson, F. C. (1961). Chronopotentiometry of Iron(II) and Iron(III) adsorbed on platinum electrodes. *Analytical Chemistry*, *33*(11), 1498-1502.
- Antiohos, D., Folkes, G., Sherrell, P., Ashraf, S., Wallace, G. G., Aitchison, P., . . . Minett, A. I. (2011). Compositional effects of PEDOT-PSS/single walled carbon nanotube films on supercapacitor device performance. *Journal of Materials Chemistry*, *21*(40), 15987-15994.
- Ardizzone, S., Fregonara, G., & Trasatti, S. (1990). "Inner" and "outer" active surface of RuO₂ electrodes. *Electrochimica Acta*, *35*(1), 263-267.
- Aref, A. A., & Tang, Y. W. (2014). Chemical bath deposition synthesis and electrochemical properties of MnO₂ thin film: Effect of deposition time and bath temperature. *Materials Science-Poland*, *32*(4), 555-564.
- Augustyn, V., Simon, P., & Dunn, B. (2014). Pseudocapacitive oxide materials for high-rate electrochemical energy storage. *Energy & Environmental Science*, *7*(5), 1597-1614.
- Bard, A. J., & Faulkner, L. R. (2001). *Electrochemical Methods: Fundamentals and Applications*. New York: John Wiley & Sons.
- Barranco, V., Pico, F., Ibañez, J., Lillo-Rodenas, M. A., Linares-Solano, A., Kimura, M., . . . Rojo, J. M. (2009). Amorphous carbon nanofibres inducing high specific capacitance of deposited hydrous ruthenium oxide. *Electrochimica Acta*, *54*(28), 7452-7457.
- Becker, H. I. (1957). United States Patent No. 2800616. U. S. P. Office.
- Biswal, A., Chandra Tripathy, B., Sanjay, K., Subbaiah, T., & Minakshi, M. (2015). Electrolytic manganese dioxide (EMD): a perspective on worldwide production, reserves and its role in electrochemistry. *RSC Advances*, *5*(72), 58255-58283.

- Bockris, J. O. M., Devanathan, M.A., Muller, K. (1963). On the structure of charged interfaces. *Proceedings of the Royal Society of London. Series A. Mathematical and Physical Sciences*, 274(1356), 55-79.
- Bolto, B., McNeill, R., & Weiss, D. (1963). Electronic conduction in polymers. iii. electronic properties of polypyrrole. *Australian Journal of Chemistry*, 16(6), 1090-1103.
- Boos, D. L. (1970). United States Patent No. 3536963. U. S. P. Office.
- Brousse, T., Bélanger, D., & Long, J. W. (2015). To be or not to be pseudocapacitive? *Journal of The Electrochemical Society*, 162(5), A5185-A5189.
- Burke, L. D., & Healy, J. F. (1981). The importance of reactive surface groups with regard to the electrocatalytic behaviour of oxide (Especially RuO₂) anodes. *Journal of Electroanalytical Chemistry and Interfacial Electrochemistry*, 124(1), 327-332.
- Burke, L. D., & McCarthy, M. (1984). Oxygen gas evolution at, and deterioration of, RuO₂/ZrO₂-coated titanium anodes at elevated temperature in strong base. *Electrochimica Acta*, 29(2), 211-216.
- Burke, L. D., & Murphy, O. J. (1980). The electrochemical behaviour of RuO₂-based mixed-oxide anodes in base. *Journal of Electroanalytical Chemistry and Interfacial Electrochemistry*, 109(1), 199-212.
- Cavani, F., Trifirò, F., & Vaccari, A. (1991). Hydrotalcite-type anionic clays: Preparation, properties and applications. *Catalysis Today*, 11(2), 173-301.
- Chaitra, K., Sivaraman, P., Vinny, R. T., Bhatta, U. M., Nagaraju, N., & Kathyayini, N. (2016). High energy density performance of hydrothermally produced hydrous ruthenium oxide/multiwalled carbon nanotubes composite: Design of an asymmetric supercapacitor with excellent cycle life. *Journal of Energy Chemistry*, 25(4), 627-635.
- Chang, J.-K., Chen, Y.-L., & Tsai, W.-T. (2004). Effect of heat treatment on material characteristics and pseudo-capacitive properties of manganese oxide prepared by anodic deposition. *Journal of Power Sources*, 135(1-2), 344-353.

- Chang, J.-K., Lee, M.-T., Huang, C.-H., & Tsai, W.-T. (2008). Physicochemical properties and electrochemical behavior of binary manganese–cobalt oxide electrodes for supercapacitor applications. *Materials Chemistry and Physics*, *108*(1), 124-131.
- Chapman, D. L. (1913). *Philosophical Magazine*, *25*.
- Chen, C.-Y., Wang, S.-C., Tien, Y.-H., Tsai, W.-T., & Lin, C.-K. (2009). Hybrid manganese oxide films for supercapacitor application prepared by sol–gel technique. *Thin Solid Films*, *518*(5), 1557-1560.
- Chen, H., Zhou, S., & Wu, L. (2014). Porous nickel hydroxide–manganese dioxide-reduced graphene oxide ternary hybrid spheres as excellent supercapacitor electrode materials. *ACS Applied Materials & Interfaces*, *6*(11), 8621-8630.
- Chen, J., Li, Y., Huang, L., Li, C., & Shi, G. (2015). High-yield preparation of graphene oxide from small graphite flakes via an improved Hummers method with a simple purification process. *Carbon*, *81*, 826-834.
- Chen, J., Yao, B., Li, C., & Shi, G. (2013). An improved Hummers method for eco-friendly synthesis of graphene oxide. *Carbon*, *64*, 225-229.
- Chen, P., Chen, H., Qiu, J., & Zhou, C. (2010). Inkjet printing of single-walled carbon nanotube/RuO₂ nanowire supercapacitors on cloth fabrics and flexible substrates. *Nano Research*, *3*(8), 594-603.
- Chen, S.-H., Wu, C.-H., Fang, A., & Lin, C.-K. (2016). Effects of adding different morphological carbon nanomaterials on supercapacitive performance of sol–gel manganese oxide films. *Ceramics International*, *42*(4), 4797-4805.
- Chen, S., Zhu, J., Wu, X., Han, Q., & Wang, X. (2010). Graphene oxide–MnO₂ nanocomposites for supercapacitors. *ACS nano*, *4*(5), 2822-2830.
- Chen, Y., Xu, J., Yang, Y., Zhao, Y., Yang, W., Mao, X., . . . Li, S. (2016). The preparation and electrochemical properties of PEDOT:PSS/MnO₂/PEDOT ternary film and its application in flexible micro-supercapacitor. *Electrochimica Acta*, *193*, 199-205.
- Chen, Y., Zhang, X., Zhang, D., & Ma, Y. (2012). High power density of graphene-based supercapacitors in ionic liquid electrolytes. *Materials Letters*, *68*, 475-477.

- Chen, Y., Zhang, X., Zhang, D., Yu, P., & Ma, Y. (2011). High performance supercapacitors based on reduced graphene oxide in aqueous and ionic liquid electrolytes. *Carbon*, 49(2), 573-580.
- Cheng, T., Zhang, Y.-Z., Zhang, J.-D., Lai, W.-Y., & Huang, W. (2016). High-performance free-standing PEDOT:PSS electrodes for flexible and transparent all-solid-state supercapacitors. *Journal of Materials Chemistry A*, 4(27), 10493-10499.
- Cho, S., Kim, M., & Jang, J. (2015). Screen-printable and flexible RuO₂ nanoparticle-decorated PEDOT:PSS/graphene nanocomposite with enhanced electrical and electrochemical performances for high-capacity supercapacitor. *ACS Applied Materials & Interfaces*, 7(19), 10213-10227.
- Choucair, M., Thordarson, P., & Stride, J. A. (2009). Gram-scale production of graphene based on solvothermal synthesis and sonication. *Nature Nanotechnology*, 4(1), 30-33.
- Clarke, C. J., Browning, G. J., & Donne, S. W. (2006). An RDE and RRDE study into the electrodeposition of manganese dioxide. *Electrochimica Acta*, 51(26), 5773-5784.
- Conway, B. E. (1999). *Electrochemical Supercapacitors: Scientific Fundamentals and Technological Applications*: Springer US.
- Conway, B. E., Birss, V., & Wojtowicz, J. (1997). The role and utilization of pseudocapacitance for energy storage by supercapacitors. *Journal of Power Sources*, 66(1-2), 1-14.
- Cornell, A., & Simonsson, D. (1993). Ruthenium dioxide as cathode material for hydrogen evolution in hydroxide and chlorate solutions. *Journal of The Electrochemical Society*, 140(11), 3123-3129.
- Cuentas Gallegos, A. K., & Rincón, M. E. (2006). Carbon nanofiber and PEDOT-PSS bilayer systems as electrodes for symmetric and asymmetric electrochemical capacitor cells. *Journal of Power Sources*, 162(1), 743-747.
- Davis, M., Gümeçi, C., Kiel, C., & Hope-Weeks, L. J. (2011). Preparation of porous manganese oxide nanomaterials by one-pot synthetic sol-gel method. *Journal of Sol-Gel Science and Technology*, 58(2), 535-538.

- Delhaès, P. (2000). Polymorphism of carbon. In P. Delhaès (Ed.), *World of Carbon* (pp. 1): Gordon and Breach Science Publishers.
- Della Noce, R., Eugenio, S., Boudard, M., Rapenne, L., Silva, T. M., Carnezim, M. J., . . . Montemor, M. F. (2016). One-step process to form a nickel-based/carbon nanofoam composite supercapacitor electrode using Na₂SO₄ as an eco-friendly electrolyte. *RSC Advances*, 6(19), 15920-15928.
- Deng, L., Wang, J., Zhu, G., Kang, L., Hao, Z., Lei, Z., . . . Liu, Z.-H. (2014). RuO₂/graphene hybrid material for high performance electrochemical capacitor. *Journal of Power Sources*, 248, 407-415.
- Desai, B. D., Fernandes, J. B., & Dalal, V. N. K. (1985). Manganese dioxide: A review of a battery chemical Part II. Solid state and electrochemical properties of manganese dioxides. *Journal of Power Sources*, 16(1), 1-43.
- Deshmukh, P. R., Patil, S. V., Bulakhe, R. N., Sartale, S. D., & Lokhande, C. D. (2014). Inexpensive synthesis route of porous polyaniline–ruthenium oxide composite for supercapacitor application. *Chemical Engineering Journal*, 257, 82-89.
- Deshpande, R. P. (2015). Ultracapacitors: the future of energy storage *Capacitors: McGraw Hill Professional, Access Engineering*.
- Ding, R., Qi, L., Jia, M., & Wang, H. (2013). Facile and large-scale chemical synthesis of highly porous secondary submicron/micron-sized NiCo₂O₄ materials for high-performance aqueous hybrid AC-NiCo₂O₄ electrochemical capacitors. *Electrochimica Acta*, 107, 494-502.
- Du, J., Zhou, G., Zhang, H., Cheng, C., Ma, J., Wei, W., . . . Wang, T. (2013). Ultrathin Porous NiCo₂O₄ Nanosheet Arrays on Flexible Carbon Fabric for High-Performance Supercapacitors. *ACS Applied Materials & Interfaces*, 5(15), 7405-7409.
- Ezema, F., Ekwealor, A., & Osuji, R. (2008). Optical properties of chemical bath deposited nickel oxide (NiO_x) thin films. *Superficies y vacío*, 21(1), 6-10.
- Fleischmann, M., Thirsk, H. R., & Tordesillas, I. M. (1962). Kinetics of electrodeposition of γ -manganese dioxide. *Transactions of the Faraday Society*, 58(0), 1865-1877.

- Fox, D. M., Gilman, J. W., Morgan, A. B., Shields, J. R., Maupin, P. H., Lyon, R. E., . . . Trulove, P. C. (2008). Flammability and thermal analysis characterization of imidazolium-based ionic liquids. *Industrial & Engineering Chemistry Research*, 47(16), 6327-6332.
- Francois Beguin, E. F. (2009). *Carbon Materials for Electrochemical Energy Storage Systems*: CRC Press.
- Frackowiak, E., Khomenko, V., Jurewicz, K., Lota, K., & Béguin, F. (2006). Supercapacitors based on conducting polymers/nanotubes composites. *Journal of Power Sources*, 153(2), 413-418.
- Gamby, J., Taberna, P. L., Simon, P., Fauvarque, J. F., & Chesneau, M. (2001). Studies and characterisations of various activated carbons used for carbon/carbon supercapacitors. *Journal of Power Sources*, 101(1), 109-116.
- Geim, A. K., & Novoselov, K. S. (2007). The rise of graphene. *Nature Materials*, 6(3), 183-191.
- Gouy, L. G. (1910). *Comptes Rendus Chimie*, 149.
- Grahame, D. C. (1947). The electrical double layer and the theory of electrocapillarity. *Chemical Reviews*, 41, 441-501.
- Groenendaal, L., Jonas, F., Freitag, D., Pielartzik, H. and Reynolds, J. R. (2000). Poly(3,4-ethylenedioxythiophene) and its derivatives: past, present, and future. *Advanced Materials*, 12, 481-494.
- Guo, X. L., Liu, X. Y., Hao, X. D., Zhu, S. J., Dong, F., Wen, Z. Q., & Zhang, Y. X. (2016). Nickel-manganese layered double hydroxide nanosheets supported on nickel foam for high-performance supercapacitor electrode materials. *Electrochimica Acta*, 194, 179-186.
- Gurunathan, K., Murugan, A. V., Marimuthu, R., Mulik, U. P., & Amalnerkar, D. P. (1999). Electrochemically synthesised conducting polymeric materials for applications towards technology in electronics, optoelectronics and energy storage devices. *Materials Chemistry and Physics*, 61(3), 173-191.
- Gómez-Navarro, C., Weitz, R. T., Bittner, A. M., Scolari, M., Mews, A., Burghard, M., & Kern, K. (2007). Electronic transport properties of individual chemically reduced graphene oxide sheets. *Nano Letters*, 7(11), 3499-3503.

- Hareesh, K., Shateesh, B., Joshi, R. P., Dahiwal, S. S., Bhoraskar, V. N., Haram, S. K., & Dhole, S. D. (2016). PEDOT:PSS wrapped NiFe₂O₄/rGO tertiary nanocomposite for the super-capacitor applications. *Electrochimica Acta*, 201, 106-116.
- He, H., Klinowski, J., Forster, M., & Lerf, A. (1998). A new structural model for graphite oxide. *Chemical Physics Letters*, 287(1-2), 53-56.
- Helmholtz, H. (1853). Ueber einige Gesetze der Vertheilung elektrischer Ströme in körperlichen Leitern mit Anwendung auf die thierisch-elektrischen Versuche. *Annalen der Physik*, 165(6).
- Herman, H. B., & Bard, A. J. (1963). Cyclic chronopotentiometry. diffusion controlled electrode reaction of a single component system. *Analytical Chemistry*, 35(9), 1121-1125.
- Heywang, G., & Jonas, F. (1992). Poly(alkylenedioxythiophene)s—new, very stable conducting polymers. *Advanced Materials*, 4(2), 116-118.
- Higgins, T. M., & Coleman, J. N. (2015). Avoiding resistance limitations in high-performance transparent supercapacitor electrodes based on large-area, high-conductivity PEDOT:PSS Films. *ACS Applied Materials & Interfaces*, 7(30), 16495-16506.
- Hong, S., Lee, S., & Paik, U. (2014). Core-shell tubular nanostructured electrode of hollow carbon nanofiber/manganese oxide for electrochemical capacitors. *Electrochimica Acta*, 141, 39-44.
- Hou, Y., Cheng, Y., Hobson, T., & Liu, J. (2010). Design and synthesis of hierarchical MnO₂ nanospheres/carbon nanotubes/conducting polymer ternary composite for high performance electrochemical electrodes. *Nano Letters*, 10(7), 2727-2733.
- Huang, L., Chen, D., Ding, Y., Feng, S., Wang, Z. L., & Liu, M. (2013). Nickel-cobalt hydroxide nanosheets coated on NiCo₂O₄ nanowires grown on carbon fiber paper for high-performance pseudocapacitors. *Nano Letters*, 13(7), 3135-3139.
- Huang, M., Li, F., Ji, J. Y., Zhang, Y. X., Zhao, X. L., & Gao, X. (2014). Facile synthesis of single-crystalline NiO nanosheet arrays on Ni foam for high-performance supercapacitors. *Crystal Engineering Communications*, 16(14), 2878-2884.

- Huang, N. M., Lim, H. N., Chia, C. H., Yarmo, M. A., & Muhamad, M. R. (2011). Simple room-temperature preparation of high-yield large-area graphene oxide. *International Journal of Nanomedicine*, 6, 3443-3448.
- Hu, C.-C., & Tsou, T.-W. (2002). Ideal capacitive behavior of hydrous manganese oxide prepared by anodic deposition. *Electrochemistry Communications*, 4(2), 105-109.
- Hwang, J. Y., El-Kady, M. F., Wang, Y., Wang, L., Shao, Y., Marsh, K., . . . Kaner, R. B. (2015). Direct preparation and processing of graphene/RuO₂ nanocomposite electrodes for high-performance capacitive energy storage. *Nano Energy*, 18, 57-70.
- Jacob, G. M., & Zhitomirsky, I. (2008). Microstructure and properties of manganese dioxide films prepared by electrodeposition. *Applied Surface Science*, 254(20), 6671-6676.
- Jagadale, A. D., Guan, G., Li, X., Du, X., Ma, X., Hao, X., & Abudula, A. (2016). Ultrathin nanoflakes of cobalt–manganese layered double hydroxide with high reversibility for asymmetric supercapacitor. *Journal of Power Sources*, 306, 526-534.
- Jin, Y., Huang, S., Zhang, M., Jia, M., & Hu, D. (2013). A green and efficient method to produce graphene for electrochemical capacitors from graphene oxide using sodium carbonate as a reducing agent. *Applied Surface Science*, 268, 541-546.
- Jing, M., Wang, C., Hou, H., Wu, Z., Zhu, Y., Yang, Y., . . . Ji, X. (2015). Ultrafine nickel oxide quantum dots embedded with few-layer exfoliative graphene for an asymmetric supercapacitor: Enhanced capacitances by alternating voltage. *Journal of Power Sources*, 298, 241-248.
- Juang, Z.-Y., Wu, C.-Y., Lu, A.-Y., Su, C.-Y., Leou, K.-C., Chen, F.-R., & Tsai, C.-H. (2010). Graphene synthesis by chemical vapor deposition and transfer by a roll-to-roll process. *Carbon*, 48(11), 3169-3174.
- Jurewicz, K., Delpeux, S., Bertagna, V., Béguin, F., & Frackowiak, E. (2001). Supercapacitors from nanotubes/polypyrrole composites. *Chemical Physics Letters*, 347(1-3), 36-40.
- Kandalkar, S. G., Lee, H.-M., Seo, S. H., Lee, K., & Kim, C.-K. (2011). Preparation and characterization of the electrodeposited Ni-Co oxide thin films for electrochemical capacitors. *Korean Journal of Chemical Engineering*, 28(6), 1464-1467.

- Kao, W.-H., & Weibel, V. J. (1992). Electrochemical oxidation of manganese(II) at a platinum electrode. *Journal of Applied Electrochemistry*, 22(1), 21-27.
- Karade, S. S., & Sankapal, B. R. (2016). Room temperature PEDOT: PSS encapsulated MWCNTs thin film for electrochemical supercapacitor. *Journal of Electroanalytical Chemistry*, 771, 80-86.
- Kvarnström, C., Neugebauer, H., Blomquist, S., Ahonen, H. J., Kankare, J., & Ivaska, A. (1999). In situ spectroelectrochemical characterization of poly(3,4-ethylenedioxythiophene). *Electrochimica Acta*, 44(16), 2739-2750.
- Khomenko, V., Frackowiak, E., & Béguin, F. (2005). Determination of the specific capacitance of conducting polymer/nanotubes composite electrodes using different cell configurations. *Electrochimica Acta*, 50(12), 2499-2506.
- Kim, H.-S., Cook, J. B., Tolbert, S. H., & Dunn, B. (2015). The development of pseudocapacitive properties in nanosized-MoO₂. *Journal of The Electrochemical Society*, 162(5), A5083-A5090.
- Kim, J.-Y., Kim, K.-H., Kim, H.-K., Park, S.-H., Roh, K. C., & Kim, K.-B. (2015). Template-free synthesis of ruthenium oxide nanotubes for high-performance electrochemical capacitors. *ACS Applied Materials & Interfaces*, 7(30), 16686-16693.
- Kissinger, P. T., & Heineman, W. R. (1983). Cyclic voltammetry. *Journal of Chemical Education*, 60(9), 702-706.
- Kumar, P. V., Bardhan, N. M., Tongay, S., Wu, J., Belcher, A. M., & Grossman, J. C. (2014). Scalable enhancement of graphene oxide properties by thermally driven phase transformation. *Nature Chemistry*, 6(2), 151-158.
- Lee, H.-M., Jeong, G. H., Kang, D. W., Kim, S.-W., & Kim, C.-K. (2015). Direct and environmentally benign synthesis of manganese oxide/graphene composites from graphite for electrochemical capacitors. *Journal of Power Sources*, 281, 44-48.
- Lee, H.-M., Lee, K., & Kim, C.-K. (2014). Electrodeposition of manganese-nickel oxide films on a graphite sheet for electrochemical capacitor applications. *Materials*, 7(1), 265-274.

- Lee, H., Kim, H., Cho, M. S., Choi, J., & Lee, Y. (2011). Fabrication of polypyrrole (PPy)/carbon nanotube (CNT) composite electrode on ceramic fabric for supercapacitor applications. *Electrochimica Acta*, 56(22), 7460-7466.
- Lee, H. Y., Manivannan, V., & Goodenough, J. B. (1999). Electrochemical capacitors with KCl electrolyte. *Comptes Rendus de l'Académie des Sciences - Series IIC - Chemistry*, 2(11), 565-577.
- Lee, S.-W., Bak, S.-M., Lee, C.-W., Jaye, C., Fischer, D. A., Kim, B.-K., . . . Kim, K.-B. (2014). Structural changes in reduced graphene oxide upon MnO₂ deposition by the redox reaction between carbon and permanganate ions. *The Journal of Physical Chemistry C*, 118(5), 2834-2843.
- Leng, X., Zou, J., Xiong, X., & He, H. (2015). Electrochemical capacitive behavior of RuO₂/graphene composites prepared under various precipitation conditions. *Journal of Alloys and Compounds*, 653, 577-584.
- Li, D., Muller, M. B., Gilje, S., Kaner, R. B., & Wallace, G. G. (2008). Processable aqueous dispersions of graphene nanosheets. *Nature Nanotechnology*, 3(2), 101-105.
- Li, L., Zhang, Y., Shi, F., Zhang, Y., Zhang, J., Gu, C., . . . Tu, J. (2014). Spinel manganese–nickel–cobalt ternary oxide nanowire array for high-performance electrochemical capacitor applications. *ACS Applied Materials & Interfaces*, 6(20), 18040-18047.
- Li, M., Cheng, J. P., Liu, F., & Zhang, X. B. (2015). In situ growth of nickel-cobalt oxyhydroxide/oxide on carbon nanotubes for high performance supercapacitors. *Electrochimica Acta*, 178, 439-446.
- Liaw, H.-J., Huang, S.-K., Chen, H.-Y., & Liu, S.-N. (2012). Reason for ionic liquids to be combustible. *Procedia Engineering*, 45, 502-506.
- Lin, C.-K., Chuang, K.-H., Lin, C.-Y., Tsay, C.-Y., & Chen, C.-Y. (2007). Manganese oxide films prepared by sol–gel process for supercapacitor application. *Surface and Coatings Technology*, 202(4–7), 1272-1276.
- Liu, F.-J. (2008). Electrodeposition of manganese dioxide in three-dimensional poly(3,4-ethylenedioxythiophene)–poly(styrene sulfonic acid)–polyaniline for supercapacitor. *Journal of Power Sources*, 182(1), 383-388.

- Liu, J., Essner, J., & Li, J. (2010). Hybrid supercapacitor based on coaxially coated manganese oxide on vertically aligned carbon nanofiber arrays. *Chemistry of Materials*, 22(17), 5022-5030.
- Liu, Y., Weng, B., Razal, J. M., Xu, Q., Zhao, C., Hou, Y., . . . Chen, J. (2015). High-performance flexible all-solid-state supercapacitor from large free-standing graphene-PEDOT/PSS films. *Scientific Reports*, 5, 17045-17054.
- Lokhande, C. D., Dubal, D. P., & Joo, O.-S. (2011). Metal oxide thin film based supercapacitors. *Current Applied Physics*, 11(3), 255-270.
- Lota, K., Khomenko, V., & Frackowiak, E. (2004). Capacitance properties of poly(3,4-ethylenedioxythiophene)/carbon nanotubes composites. *Journal of Physics and Chemistry of Solids*, 65(2-3), 295-301.
- Lu, X., Zheng, D., Zhai, T., Liu, Z., Huang, Y., Xie, S., & Tong, Y. (2011). Facile synthesis of large-area manganese oxide nanorod arrays as a high-performance electrochemical supercapacitor. *Energy & Environmental Science*, 4(8), 2915-2921.
- Madou, M. J. (2011). Electrochemical and optical analytical techniques *Solid-State Physics, Fluidics, and Analytical Techniques in Micro-and Nanotechnology* (Vol. 1, pp. 517): CRC Press.
- Mamak, M., Coombs, N., & Ozin, G. A. (2001). Mesoporous nickel–yttria–zirconia fuel cell materials. *Chemistry of Materials*, 13(10), 3564-3570.
- Marsh, H., & Reinoso, F. R. (2006a). Activated carbon (origins) *Activated Carbon*. Amsterdam London: Elsevier.
- Marsh, H., & Reinoso, F. R. (2006b). Characterization of activated carbon *Activated Carbon*. Amsterdam London: Elsevier.
- Marcano, D. C., Kosynkin, D. V., Berlin, J. M., Sinitskii, A., Sun, Z., Slesarev, A., . . . Tour, J. M. (2010). Improved synthesis of graphene oxide. *ACS Nano*, 4(8), 4806-4814.
- McNally, E. A., Zhitomirsky, I., & Wilkinson, D. S. (2005). Cathodic electrodeposition of cobalt oxide films using polyelectrolytes. *Materials Chemistry and Physics*, 91(2-3), 391-398.

- Melsheimer, J., & Ziegler, D. (1988). The oxygen electrode reaction in acid solutions on RuO₂ electrodes prepared by the thermal decomposition method. *Thin Solid Films*, 163, 301-308.
- Messaoudi, B., Joiret, S., Keddou, M., & Takenouti, H. (2001). Anodic behaviour of manganese in alkaline medium. *Electrochimica Acta*, 46(16), 2487-2498.
- Michalak, F., von Rottkay, K., Richardson, T., Slack, J., & Rubin, M. (1999). Electrochromic lithium nickel oxide thin films by RF-sputtering from a LiNiO₂ target. *Electrochimica Acta*, 44(18), 3085-3092.
- Miller, J. (2007). A brief history of supercapacitors. *Batteries and Energy Storage Technology*, Autumn 2007.
- Miller, J. R. (2006). Electrochemical capacitor thermal management issues at high-rate cycling. *Electrochimica Acta*, 52(4), 1703-1708.
- Mondal, S. K., & Munichandraiah, N. (2008). Anodic deposition of porous RuO₂ on stainless steel for supercapacitor studies at high current densities. *Journal of Power Sources*, 175(1), 657-663.
- Mousavi, M. P. S., Wilson, B. E., Kashefolgheta, S., Anderson, E. L., He, S., Bühlmann, P., & Stein, A. (2016). Ionic liquids as electrolytes for electrochemical double-layer capacitors: structures that optimize specific energy. *ACS Applied Materials & Interfaces*, 8(5), 3396-3406.
- Nagarajan, N., Humadi, H., & Zhitomirsky, I. (2006). Cathodic electrodeposition of MnO_x films for electrochemical supercapacitors. *Electrochimica Acta*, 51(15), 3039-3045.
- Novoselov, K. S., Geim, A. K., Morozov, S., Jiang, D., Zhang, Y., Dubonos, S., . . . Firsov, A. (2004). Electric field effect in atomically thin carbon films. *Science*, 306(5696), 666-669.
- Ohno, H., & Fukumoto, K. (2008). Progress in ionic liquids for electrochemical reaction matrices. *Electrochemistry*, 76(1), 16-23.
- Pandolfo, A. G., & Hollenkamp, A. F. (2006). Carbon properties and their role in supercapacitors. *Journal of Power Sources*, 157(1), 11-27.

- Pang, S. C., Anderson, M. A., & Chapman, T. W. (2000). Novel electrode materials for thin film ultracapacitors: comparison of electrochemical properties of sol-gel derived and electrodeposited manganese dioxide. *Journal of The Electrochemical Society*, 147(2), 444-450.
- Patake, V. D., & Lokhande, C. D. (2008). Chemical synthesis of nano-porous ruthenium oxide (RuO₂) thin films for supercapacitor application. *Applied Surface Science*, 254(9), 2820-2824.
- Patil, D. S., Pawar, S. A., Kim, J. H., Patil, P. S., & Shin, J. C. (2016). Facile preparation and enhanced capacitance of the Ag-PEDOT:PSS/polyaniline nanofiber network for supercapacitors. *Electrochimica Acta*, 213, 680-690.
- Paul, R. L., & Cartwright, A. (1986). The mechanism of the deposition of manganese dioxide. *Journal of Electroanalytical Chemistry and Interfacial Electrochemistry*, 201(1), 113-122.
- Paunovic, M. (1967). Chronopotentiometry. *Journal of Electroanalytical Chemistry and Interfacial Electrochemistry*, 14(4), 447-474.
- Pei, L., Zhang, X., Zhang, L., Zhang, Y., & Xu, Y. (2016). Solvent influence on the morphology and supercapacitor performance of the nickel oxide. *Materials Letters*, 162, 238-241.
- Pei, Q., Zuccarello, G., Ahlskog, M., & Inganäs, O. (1994). Electrochromic and highly stable poly(3,4-ethylenedioxythiophene) switches between opaque blue-black and transparent sky blue. *Polymer*, 35(7), 1347-1351.
- Peng, C., Jin, J., & Chen, G. Z. (2007). A comparative study on electrochemical co-deposition and capacitance of composite films of conducting polymers and carbon nanotubes. *Electrochimica Acta*, 53(2), 525-537.
- Peng, C., Zhang, S., Jewell, D., & Chen, G. Z. (2008). Carbon nanotube and conducting polymer composites for supercapacitors. *Progress in Natural Science*, 18(7), 777-788.
- Pico, F., Morales, E., Fernandez, J. A., Centeno, T. A., Ibañez, J., Rojas, R. M., . . . Rojo, J. M. (2009). Ruthenium oxide/carbon composites with microporous or mesoporous carbon as support and prepared by two procedures. A comparative study as supercapacitor electrodes. *Electrochimica Acta*, 54(8), 2239-2245.

- Poizot, P., Laruelle, S., Grugeon, S., Dupont, L., & Tarascon, J. M. (2000). Nano-sized transition-metal oxides as negative-electrode materials for lithium-ion batteries. *Nature*, 407(6803), 496-499.
- Qiu, G., Huang, H., Dharmarathna, S., Benbow, E., Stafford, L., & Suib, S. L. (2011). Hydrothermal synthesis of manganese oxide nanomaterials and their catalytic and electrochemical properties. *Chemistry of Materials*, 23(17), 3892-3901.
- Ranjusha, R., Sajesh, K. M., Roshny, S., Lakshmi, V., Anjali, P., Sonia, T. S., . . . Balakrishnan, A. (2014). Supercapacitors based on freeze dried MnO₂ embedded PEDOT: PSS hybrid sponges. *Microporous and Mesoporous Materials*, 186, 30-36.
- Reddy, R. N., & Reddy, R. G. (2004). Synthesis and electrochemical characterization of amorphous MnO₂ electrochemical capacitor electrode material. *Journal of Power Sources*, 132(1-2), 315-320.
- Rightmire, R. A. (1966). United States Patent No. 3288641. U. S. P. Office.
- Rodríguez-Reinoso, F., & Molina-Sabio, M. (1992). Activated carbons from lignocellulosic materials by chemical and/or physical activation: an overview. *Carbon*, 30(7), 1111-1118.
- Rudge, A., Raistrick, I., Gottesfeld, S., & Ferraris, J. P. (1994). A study of the electrochemical properties of conducting polymers for application in electrochemical capacitors. *Electrochimica Acta*, 39(2), 273-287.
- Sarkar, A., Kumar Satpati, A., Kumar, V., & Kumar, S. (2015). Sol-gel synthesis of manganese oxide films and their predominant electrochemical properties. *Electrochimica Acta*, 167, 126-131.
- Sato, T., Masuda, G., & Takagi, K. (2004). Electrochemical properties of novel ionic liquids for electric double layer capacitor applications. *Electrochimica Acta*, 49(21), 3603-3611.
- Sawangphruk, M., Pinitsoontorn, S., & Limtrakul, J. (2012). Surfactant-assisted electrodeposition and improved electrochemical capacitance of silver-doped manganese oxide pseudocapacitor electrodes. *Journal of Solid State Electrochemistry*, 16(8), 2623-2629.
- Sharma, P., & Bhatti, T. S. (2010). A review on electrochemical double-layer capacitors. *Energy Conversion and Management*, 51(12), 2901-2912.

- Shen, J., Li, T., Huang, W., Long, Y., Li, N., & Ye, M. (2013). One-pot polyelectrolyte assisted hydrothermal synthesis of RuO₂-reduced graphene oxide nanocomposite. *Electrochimica Acta*, *95*, 155-161.
- Shi, X., Zeng, Z., Guo, E., Long, X., Zhou, H., & Wang, X. (2017). A growth mechanism investigation on the anodic deposition of nanoporous gold supported manganese oxide nanostructures for high performance flexible supercapacitors. *Journal of Alloys and Compounds*, *690*, 791-798.
- Shi, Y., Peng, L., Ding, Y., Zhao, Y., & Yu, G. (2015). Nanostructured conductive polymers for advanced energy storage. *Chemical Society Reviews*, *44*(19), 6684-6696.
- Shinomiya, T., Gupta, V., & Miura, N. (2006). Effects of electrochemical-deposition method and microstructure on the capacitive characteristics of nano-sized manganese oxide. *Electrochimica Acta*, *51*(21), 4412-4419.
- Shirakawa, H., Louis, E. J., MacDiarmid, A. G., Chiang, C. K., & Heeger, A. J. (1977). Synthesis of electrically conducting organic polymers: halogen derivatives of polyacetylene, (CH). *Journal of the Chemical Society, Chemical Communications*(16), 578-580.
- Singh, A. K., Sarkar, D., Karmakar, K., Mandal, K., & Khan, G. G. (2016). High-performance supercapacitor electrode based on cobalt oxide–manganese dioxide–nickel oxide ternary 1D hybrid nanotubes. *ACS Applied Materials & Interfaces*, *8*(32), 20786-20792.
- Snook, G. A., Kao, P., & Best, A. S. (2011). Conducting-polymer-based supercapacitor devices and electrodes. *Journal of Power Sources*, *196*(1), 1-12.
- Song, Z., Liu, W., Wei, W., Quan, C., Sun, N., Zhou, Q., . . . Wen, X. (2016). Preparation and electrochemical properties of Fe₂O₃/reduced graphene oxide aerogel (Fe₂O₃/rGOA) composites for supercapacitors. *Journal of Alloys and Compounds*, *685*, 355-363.
- Srinivasan, S. (2006). Electrode/electrolyte interfaces: Structure and kinetics of charge transfer *Fuel Cells: From Fundamentals to Applications* (pp. 27). Boston, MA: Springer US.
- Stankovich, S., Dikin, D. A., Piner, R. D., Kohlhaas, K. A., Kleinhammes, A., Jia, Y., . . . Ruoff, R. S. (2007). Synthesis of graphene-based nanosheets via chemical reduction of exfoliated graphite oxide. *Carbon*, *45*(7), 1558-1565.

- Stern, O. (1924). *Zeitschrift für Elektrochemie*, 30.
- Su, Z., Yang, C., Xu, C., Wu, H., Zhang, Z., Liu, T., . . . Kang, F. (2013). Co-electrodeposition of the MnO₂-PEDOT:PSS nanostructured composite for high areal mass, flexible asymmetric supercapacitor devices. *Journal of Materials Chemistry A*, 1(40), 12432-12440.
- Sugimoto, W., Iwata, H., Yokoshima, K., Murakami, Y., & Takasu, Y. (2005). Proton and electron conductivity in hydrous ruthenium oxides evaluated by electrochemical impedance spectroscopy: The origin of large capacitance. *The Journal of Physical Chemistry B*, 109(15), 7330-7338.
- Suksomboon, M., Srimuk, P., Krittayavathananon, A., Luanwuthi, S., & Sawangphruk, M. (2014). Effect of alkaline electrolytes on the charge storage capacity and morphology of porous layered double cobalt hydroxide-coated graphene supercapacitor electrodes. *RSC Advances*, 4(100), 56876-56882.
- Taberna, P. L., & Simon, P. (2013). Electrochemical techniques *Supercapacitors: Materials, System, and Applications* (pp. 111): Wiley-VCH Verlag GmbH & Co. KGaA.
- Toupin, M., Brousse, T., & Bélanger, D. (2004). Charge storage mechanism of MnO₂ electrode used in aqueous electrochemical capacitor. *Chemistry of Materials*, 16(16), 3184-3190.
- Unnikrishnan, B., Wu, C.-W., Chen, I. W. P., Chang, H.-T., Lin, C.-H., & Huang, C.-C. (2016). Carbon dot-mediated synthesis of manganese oxide decorated graphene nanosheets for supercapacitor application. *ACS Sustainable Chemistry & Engineering*, 4(6), 3008-3016.
- Vadukumpully, S., Paul, J., & Valiyaveetil, S. (2009). Cationic surfactant mediated exfoliation of graphite into graphene flakes. *Carbon*, 47(14), 3288-3294.
- Vijayakumar, S., Nagamuthu, S., & Muralidharan, G. (2013). Supercapacitor studies on NiO nanoflakes synthesized through a microwave route. *ACS Applied Materials & Interfaces*, 5(6), 2188-2196.
- Wang, C., Liu, J., Yang, Q., Sun, P., Gao, Y., Liu, F., . . . Lu, G. (2015). Ultrasensitive and low detection limit of acetone gas sensor based on W-doped NiO hierarchical nanostructure. *Sensors and Actuators B: Chemical*, 220, 59-67.

- Wang, G., Wang, B., Park, J., Wang, Y., Sun, B., & Yao, J. (2009). Highly efficient and large-scale synthesis of graphene by electrolytic exfoliation. *Carbon*, 47(14), 3242-3246.
- Wang, G., Zhang, L., & Zhang, J. (2012). A review of electrode materials for electrochemical supercapacitors. *Chemical Society Reviews*, 41(2), 797-828.
- Wang, X., Han, X., Lim, M., Singh, N., Gan, C. L., Jan, M., & Lee, P. S. (2012). Nickel cobalt oxide-single wall carbon nanotube composite material for superior cycling stability and high-performance supercapacitor application. *The Journal of Physical Chemistry C*, 116(23), 12448-12454.
- Wang, X., Yin, Y., Hao, C., & You, Z. (2015). A high-performance three-dimensional micro supercapacitor based on ripple-like ruthenium oxide-carbon nanotube composite films. *Carbon*, 82, 436-445.
- Wang, Y.-M., Zhang, X., Guo, C.-Y., Zhao, Y.-Q., Xu, C.-L., & Li, H.-L. (2013). Controllable synthesis of 3D $\text{Ni}_x\text{Co}_{1-x}$ oxides with different morphologies for high-capacity supercapacitors. *Journal of Materials Chemistry A*, 1(42), 13290-13300.
- Wang, Y., Zhao, C., Fu, W., Zhang, Z., Zhang, M., Zhou, J., . . . Xie, E. (2016). Growth of zinc cobaltate nanoparticles and nanorods on reduced graphene oxide porous networks toward high-performance supercapacitor electrodes. *Journal of Alloys and Compounds*, 668, 1-7.
- Wei, J., Nagarajan, N., & Zhitomirsky, I. (2007). Manganese oxide films for electrochemical supercapacitors. *Journal of Materials Processing Technology*, 186(1-3), 356-361.
- Wu, C.-H., Ma, J.-S., & Lu, C.-H. (2012). Synthesis and characterization of nickel-manganese oxide via the hydrothermal route for electrochemical capacitors. *Current Applied Physics*, 12(4), 1190-1194.
- Wu, X., Wang, Q., Zhang, W., Wang, Y., & Chen, W. (2016). Nano nickel oxide coated graphene/polyaniline composite film with high electrochemical performance for flexible supercapacitor. *Electrochimica Acta*, 211, 1066-1075.
- Wu, X., Xiong, W., Chen, Y., Lan, D., Pu, X., Zeng, Y., . . . Zhu, Z. (2015). High-rate supercapacitor utilizing hydrous ruthenium dioxide nanotubes. *Journal of Power Sources*, 294, 88-93.

- Wu, Z.-S., Wang, D.-W., Ren, W., Zhao, J., Zhou, G., Li, F., & Cheng, H.-M. (2010). Anchoring hydrous RuO₂ on graphene sheets for high-performance electrochemical capacitors. *Advanced Functional Materials*, 20(20), 3595-3602.
- Xie, X., & Gao, L. (2007). Characterization of a manganese dioxide/carbon nanotube composite fabricated using an in situ coating method. *Carbon*, 45(12), 2365-2373.
- Xiong, X., Ding, D., Chen, D., Waller, G., Bu, Y., Wang, Z., & Liu, M. (2015). Three-dimensional ultrathin Ni(OH)₂ nanosheets grown on nickel foam for high-performance supercapacitors. *Nano Energy*, 11, 154-161.
- Xu, J., Fan, X., Xia, Q., Shao, Z., Pei, B., Yang, Z., . . . Zhang, W. (2016a). A highly atom-efficient strategy to synthesize reduced graphene oxide-Mn₃O₄ nanoparticles composites for supercapacitors. *Journal of Alloys and Compounds*, 685, 949-956.
- Xu, J., Ju, Z., Cao, J., Wang, W., Wang, C., & Chen, Z. (2016b). Microwave synthesis of nitrogen-doped mesoporous carbon/nickel-cobalt hydroxide microspheres for high-performance supercapacitors. *Journal of Alloys and Compounds*, 689, 489-499.
- Xu, Y., Wang, L., Cao, P., Cai, C., Fu, Y., & Ma, X. (2016c). Mesoporous composite nickel cobalt oxide/graphene oxide synthesized via a template-assistant co-precipitation route as electrode material for supercapacitors. *Journal of Power Sources*, 306, 742-752.
- Xu, Z., Li, H., Li, W., Cao, G., Zhang, Q., Li, K., . . . Wang, J. (2011). Large-scale production of graphene by microwave synthesis and rapid cooling. *Chemical Communications*, 47(4), 1166-1168.
- Yadav, A. A., Jadhav, S. N., Chougule, D. M., Patil, P. D., Chavan, U. J., & Kolekar, Y. D. (2016). Spray deposited Hausmannite Mn₃O₄ thin films using aqueous/organic solvent mixture for supercapacitor applications. *Electrochimica Acta*, 206, 134-142.
- Yan, D., Liu, Y., Li, Y., Zhuo, R., Wu, Z., Ren, P., . . . Geng, Z. (2014). Synthesis and electrochemical properties of MnO₂/rGO/PEDOT:PSS ternary composite electrode material for supercapacitors. *Materials Letters*, 127, 53-55.

- Yin, C., Yang, C., Jiang, M., Deng, C., Yang, L., Li, J., & Qian, D. (2016). A novel and facile one-pot solvothermal synthesis of PEDOT–PSS/Ni–Mn–Co–O hybrid as an advanced supercapacitor electrode material. *ACS Applied Materials & Interfaces*, 8(4), 2741-2752.
- Yin, Z., & Zheng, Q. (2012). Controlled synthesis and energy applications of one-dimensional conducting polymer nanostructures: An overview. *Advanced Energy Materials*, 2(2), 179-218.
- Yuan, C., Li, J., Hou, L., Zhang, X., Shen, L., & Lou, X. W. (2012). Ultrathin mesoporous NiCo₂O₄ nanosheets supported on ni foam as advanced electrodes for supercapacitors. *Advanced Functional Materials*, 22(21), 4592-4597.
- Zang, X., Sun, C., Dai, Z., Yang, J., & Dong, X. (2017). Nickel hydroxide nanosheets supported on reduced graphene oxide for high-performance supercapacitors. *Journal of Alloys and Compounds*, 691, 144-150.
- Zhao, B., Wang, T., Jiang, L., Zhang, K., Yuen, M. M. F., Xu, J.-B., . . . Wong, C.-P. (2016). NiO mesoporous nanowalls grown on RGO coated nickel foam as high performance electrodes for supercapacitors and biosensors. *Electrochimica Acta*, 192, 205-215.
- Zhao, D., Guo, X., Gao, Y., & Gao, F. (2012). An electrochemical capacitor electrode based on porous carbon spheres hybridized with polyaniline and nanoscale ruthenium oxide. *ACS Applied Materials & Interfaces*, 4(10), 5583-5589.
- Zhao, X., Sanchez, B. M., Dobson, P. J., & Grant, P. S. (2011). The role of nanomaterials in redox-based supercapacitors for next generation energy storage devices. *Nanoscale*, 3(3), 839-855.
- Zhi, M., Manivannan, A., Meng, F., & Wu, N. (2012). Highly conductive electrospun carbon nanofiber/MnO₂ coaxial nano-cables for high energy and power density supercapacitors. *Journal of Power Sources*, 208, 345-353.
- Zhou, H., Han, G., Chang, Y., Fu, D., & Xiao, Y. (2015). Highly stable multi-wall carbon nanotubes@poly(3,4-ethylenedioxythiophene)/poly(styrene sulfonate) core-shell composites with three-dimensional porous nano-network for electrochemical capacitors. *Journal of Power Sources*, 274, 229-236.
- Zhuo, L., Wu, Y., Zhou, W., Wang, L., Yu, Y., Zhang, X., & Zhao, F. (2013). Trace amounts of water-induced distinct growth behaviors of NiO nanostructures on graphene in CO₂-expanded ethanol and their applications in lithium-ion batteries. *ACS Applied Materials & Interfaces*, 5(15), 7065-7071.

- Zu, C.-X., & Li, H. (2011). Thermodynamic analysis on energy densities of batteries. *Energy & Environmental Science*, 4(8), 2614-2624.
- Zhang, J., Kong, L.-B., Cai, J.-J., Li, H., Luo, Y.-C., & Kang, L. (2010). Hierarchically porous nickel hydroxide/mesoporous carbon composite materials for electrochemical capacitors. *Microporous and Mesoporous Materials*, 132(1-2), 154-162.
- Zhang, J., Ma, J., Zhang, L. L., Guo, P., Jiang, J., & Zhao, X. S. (2010). Template synthesis of tubular ruthenium oxides for supercapacitor applications. *The Journal of Physical Chemistry C*, 114(32), 13608-13613.
- Zhang, J., Yang, H., Shen, G., Cheng, P., Zhang, J., & Guo, S. (2010). Reduction of graphene oxide via L-ascorbic acid. *Chemical Communications*, 46(7), 1112-1114.
- Zhang, R., Liu, J., Guo, H., & Tong, X. (2014). Hierarchically porous nickel oxide nanoflake arrays grown on carbon cloth by chemical bath deposition as superior flexible electrode for supercapacitors. *Materials Letters*, 136, 198-201.
- Zheng, J. P. (1999). Ruthenium Oxide-Carbon Composite Electrodes for Electrochemical Capacitors. *Electrochemical and Solid-State Letters*, 2(8), 359-361.
- Zheng, J. P., Cygan, P. J., & Jow, T. R. (1995). Hydrous ruthenium oxide as an electrode material for electrochemical capacitors. *Journal of The Electrochemical Society*, 142(8), 2699-2703.
- Zheng, J. P., & Jow, T. R. (1995). A new charge storage mechanism for electrochemical capacitors. *Journal of The Electrochemical Society*, 142(1), L6-L8.

LIST OF PUBLICATIONS AND PAPERS PRESENTED

Articles published in ISI-cited journals:

Chan, P. Y., Rusi, & Majid, S. R. (2014). RGO-wrapped MnO₂ composite electrode for supercapacitor application. *Solid State Ionics*, 262(0), 226.

Rusi, **Chan, P. Y.**, & Majid, S. R. (2015). Layer by Layer Ex-Situ Deposited Cobalt-Manganese Oxide as Composite Electrode Material for Electrochemical Capacitor. *PLoS ONE*, 10(7).

Chan, P. Y. & Majid, S. R, (2017). Synthesis and electrochemical characterisation of amorphous manganese-nickel oxide as supercapacitor electrode material. *Ionics*, 1.

Papers presented:

Chan, P. Y. & Majid, S. R, Reduced graphene oxide-nickel-manganese oxide as composite electrode for supercapacitor application. International Conference on Advanced Capacitor (ICAC), Osaka, Japan, 27–30 May 2013.

Chan, P. Y. & Majid, S. R, Comparison study of electrochemical performances between manganese oxide film and manganese-nickel oxide film. 9th Mathematics and Physical Sciences Graduate Congress, Kuala Lumpur, Malaysia, 8–10 January 2014.

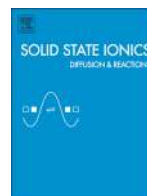
Chan, P. Y. & Majid, S. R, The effect of electrodeposition duration on the electrochemical performance of RGO-MnO₂-NiO composite electrode. International Conference on Materials Science and Technology (ICMST), Batan, Indonesia, 13–16 October 2014.

Chan, P. Y. & Majid, S. R, Cyclic voltammetric studies of cobalt oxide-nickel hydroxide composite film. International Conference on Nanotechnology, Nanomaterials & Thin Films, Manchester, United Kingdom, 13–16 June 2016.



Contents lists available at ScienceDirect

Solid State Ionics

journal homepage: www.elsevier.com/locate/ssi

RGO-wrapped MnO₂ composite electrode for supercapacitor application

P.Y. Chan, Rusi, S.R. Majid*

Centre for Ionics University of Malaya, Department of Physics, Faculty of Science, University of Malaya, 50603 Kuala Lumpur, Malaysia

ARTICLE INFO

Article history:

Received 16 May 2013

Received in revised form 13 September 2013

Accepted 1 October 2013

Available online xxxx

Keywords:

RGO

MnO₂

Electrodeposition

Supercapacitors

Green synthesis

ABSTRACT

In this paper, we report on a facile electrodeposition method to produce reduced graphene oxide (RGO)–manganese oxide (MnO₂) composite electrode for supercapacitor application. The nature of the composite electrode was examined by X-ray diffraction (XRD). The morphology and composition of the composite electrode were studied using field emission scanning electron microscope (FESEM) and energy dispersive X-ray spectroscopy (EDX). FESEM revealed the wrapping of MnO₂ nanoparticles by RGO sheets. Supercapacitor cell behavior was examined using cyclic voltammetry (CV), galvanostatic charge–discharge (CD) and electrochemical impedance. The optimum specific capacitance obtained was 378 F/g at scan rate of 1 mV/s for 13 min of electrodeposition. This is attributed to the high surface area contributed by MnO₂ nanoparticles and conductive pathway provided by RGO sheets. Cycling studies showed that this cell can retain 83% of original specific capacitance after 1000 cycles. This high capacitance composite electrode has long cycle stability which makes it suitable for supercapacitor application.

© 2013 Elsevier B.V. All rights reserved.

1. Introduction

There are many studies that focus on energy storage devices in order to overcome the problems of fossil fuel depletion. Supercapacitor is one of the attractions for many energy storage researches. There are two types of supercapacitor according to the charge storage mechanism: electric double layer capacitor (EDLC) and pseudocapacitor. The mechanism of EDLC is based on reversible adsorption of ions whereas pseudocapacitor is based on reversible surface redox reactions [1]. However, supercapacitors face the problem of low energy density. Appropriate cell design and combination of materials are believed to overcome this problem.

Transition metal oxides are one of the good candidates acting as an electrode material for pseudocapacitor because the high capacitance attributed to the fast and reversible faradaic reaction occurred at the surface. Manganese oxide (MnO₂) is one of the promising and green electrode material for supercapacitor. Although it is low cost, environmental friendly and abundant in nature, there are still some problems regarding to its poor conductivity and low cycling stability that set drawbacks for energy storage application.

Graphene has been known for its excellent mechanical, structural, thermal and electronic behaviors [2]. Such properties enable graphene alone or graphene composites to be applicable in many fields such as energy storage devices, sensors and solar cells. There are various methods such as hydrothermal treatment [3] and microwave irradiation [4] to produce reduced graphene oxide (RGO) but the most common approach is using the chemical route. Solution-based chemical reduction is

low cost and applicable for large scale production. However, the RGO sheets produced have low solubility which makes it hard to dissolve in water and organic solvent. Thus, agglomerations are easily formed between the RGO sheets due to strong π – π interactions [5]. Most of the famous reducing agents such as hydrazine, hydroquinone and hydrogen sulfide are not preferable because they are poisonous and hazardous. However, there's one reducing agent namely L-ascorbic acid, that turns out to be a good candidate for the reduction of graphene oxide (GO). Besides reducing the GO, it can also act as a surfactant to reduce the occurrence of RGO sheet re-stacking [5].

The incorporation of MnO₂ particles with RGO sheets is believed to enhance the electrochemical performance of MnO₂ itself. According to Kim et al. [6], the electrochemical supercapacitor with RGO–MnO₂ as electrode has achieved specific capacitance as high as 383.82 F/g at 10 mV/s. Herein, we prepared RGO–MnO₂ composite via green electrodeposition method. The composite electrode was characterized by X-ray diffraction (XRD), field emission scanning electron microscope (FESEM), energy dispersive X-ray spectroscopy (EDX), cyclic voltammetry (CV), galvanostatic charge–discharge (CD) and frequency response analyzer (FRA).

2. Methodology

2.1. Material

Graphite flakes (Nippon Graphite Industries, Ltd.), potassium permanganate (KMnO₄) (Bendosen), L-ascorbic acid (UNILAB), manganese acetate (Mn(CH₃COO)₂) (Fluka), sulfuric acid (H₂SO₄), phosphoric acid (H₃PO₄), hydrogen peroxide 30% (H₂O₂) and hydrogen chloride (HCl) (Friendemann Schmidt) were used as received.

* Corresponding author. Tel.: +60 379674146x4238.

E-mail address: shana@um.edu.my (S.R. Majid).

2.2. Graphite oxide synthesis

The graphite oxide is produced using simplified Hummer's method [7]. H_2SO_4 , H_3PO_4 , graphite flake and KMnO_4 were mixed together and stirred for 3 days. Next, H_2O_2 was added gradually. The precipitate formed was washed with 1 M HCl for three times and deionized water for six times by centrifugation technique. A brown solution with dispersed graphite oxide was formed.

2.3. Reduced graphene oxide–manganese oxide composite synthesis

The solution was sonicated heavily in order to exfoliate the graphite oxide to become graphene oxide (GO). Next, L-ascorbic acid solution was added into it and stirred vigorously until the solution turns black. After that the manganese acetate ($\text{Mn}(\text{CH}_3\text{COO})_2$) was added to the solution and stirred for 24 h. The solution produced acts as electrolyte for the electrodeposition process.

2.4. Electrodeposition

The electrodeposition was carried out using two-electrode system. A carbon rod and stainless steel act as counter electrode and working electrode respectively. Chronoamperometry was used to investigate the process occurred during the formation of film. The duration of the electrodeposition was varied: 10, 13, 15 and 18 min. After the electrodeposition, the stainless steel was rinsed with distilled water and heated at 100 °C for 3 h. The mass of the film formed was determined from the weight difference of the stainless steel before and after electrodeposition using a high precision microbalance (Mettler Toledo MT5).

2.5. Characterizations

The nature of the sample was examined by using D8-Advance X-ray diffraction XRD Bruker AXS with $\text{CuK}\alpha$ monochromatized radiation at 40 kV and 40 mA at ambient temperature. Jeol JSM-7600F Field-Emission Scanning Electron Microscope (FESEM) was used to investigate the surface morphology and Energy Dispersive X-Ray Spectroscopy (EDX) was used to analyze the composition of the composite electrode. The electrochemical properties of the composite electrode were studied through cyclic voltammetry (CV) and galvanostatic charge–discharge (CD) which are carried out using Autolab PGSTAT12 in 1 M Na_2SO_4 within 0–1 V potential window. Frequency Response Analyzer (FRA) in Autolab PGSTAT30 was used to run the impedance analysis of the composite electrode.

3. Results and discussion

3.1. XRD

Fig. 1 shows the XRD patterns for all electrodeposited composite on stainless steel and bare stainless steel. As seen in Fig. 1, there is no sharp (001) reflection peak of graphite oxide (GO) at $2\theta = 10.3^\circ$ indicating the GO has been successfully reduced [8]. In all XRD patterns of deposited samples, only two intensive peaks assigned to (111) and (200) reflection peaks of stainless steel was observed [9]. This may arise from amorphousness of RGO– MnO_2 thin film formed on stainless steel as reported by S. Hassan et al. [10].

3.2. FESEM and EDX

Fig. 2 shows the FESEM images obtained for 10 min, 13 min and 18 min of deposition and EDX result. Fig. 2(a) reveals that in the shortest time of electrodeposition, MnO_2 particles are difficult to be observed since the agglomeration of RGO sheets has covered most of the particles. As the duration increased to 13 min, the spherical

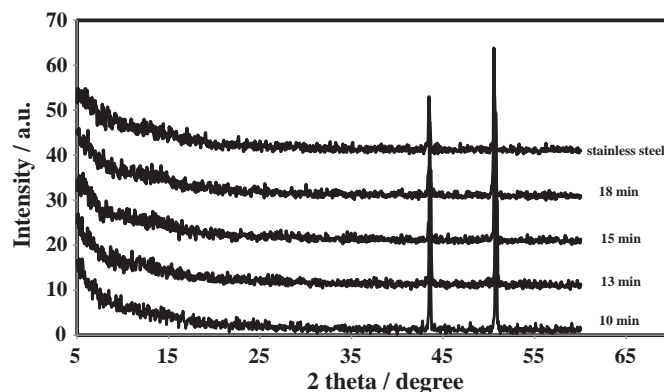
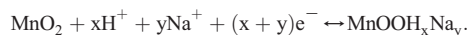


Fig. 1. XRD result for all composite electrodes and stainless steel.

shaped- MnO_2 particles are more visible and the agglomeration of RGO sheets is absent, Fig. 2(b). Thus, MnO_2 particles can be considered to play a role to prevent the re-stacking of RGO sheets as discussed by Y.J. Mai et al. [11]. The MnO_2 particle size increases when the electrodeposition duration increases. This can be seen when comparing Fig. 2(b) and (c). The increase of MnO_2 particle size increases the interfacial contact between RGO sheet and MnO_2 particles. However, this also breaks down the conductive pathway provided by the RGO as can be seen from Fig. 2(c). The elemental composition of the 13 minute-deposited composite electrode is shown in Fig. 2(d) which reveals that the RGO and MnO_2 are actually deposited on the stainless steel even though it cannot be seen from XRD patterns.

3.3. Cyclic voltammetry and charge–discharge studies

In order to explore the applicability of the composite electrodes in supercapacitor, CV measurement has been carried out at different scan rates: 1, 5, 10, 15 and 20 mV/s. The results are shown in Fig. 3. The cyclic voltammetry curves for all electrode samples at 1 mV/s are illustrated in Fig. 3(a). The nearly rectangular feature of CV curves coupled with redox peaks indicates the combination of double layer and pseudocapacitance behaviors which are resulted from the synergistic integration of RGO– MnO_2 composition [12]. The symmetrical nature of the CV curves implies the kinetic reversibility in the intercalation/deintercalation process. The broad peaks that appeared is caused by the redox reaction of $\text{Mn}^{3+}/\text{Mn}^{4+}$ in sodium electrolyte system based on the following charge storage mechanism :



The anodic peak at ~ 0.7 V and cathodic peak at ~ 0.2 V are due to the redox reaction assigned to $\text{Mn}^{3+}/\text{Mn}^{4+}$ couple and in agreement with other reports [13].

The specific capacitance was calculated with the equation $\text{SC} = I_{\text{av}} / (\text{SR} \times m_d)$ where SC = specific capacitance, I_{av} = average current, SR = scan rate and m_d = mass difference of the composite electrode. The masses of the composite films obtained are 0.29 mg, 0.184 mg, 0.24 mg and 1.054 mg for 10, 13, 15 and 18 minute-deposited composite electrode respectively. The optimum specific capacitance obtained was 378 F/g when the electrodeposition duration of 13 min is applied. This may attribute to the well distribution and large surface area offered by MnO_2 nanoparticles together with the conductive pathway built up by the RGO sheets as shown in Fig. 2(b). MnO_2 in nano-scale helps to reduce the diffusion path of electrolyte ions during the charging and discharging process [14]. Fig. 3(c) provides graphs of the calculated specific capacitance against scan rate and it was found that the SC decreases with increases of the scan rate. This may be due to the dependence of electrochemical performance on diffusion of electrolyte ions [15]. When the scan rate is high, the diffusion of electrolyte ions will

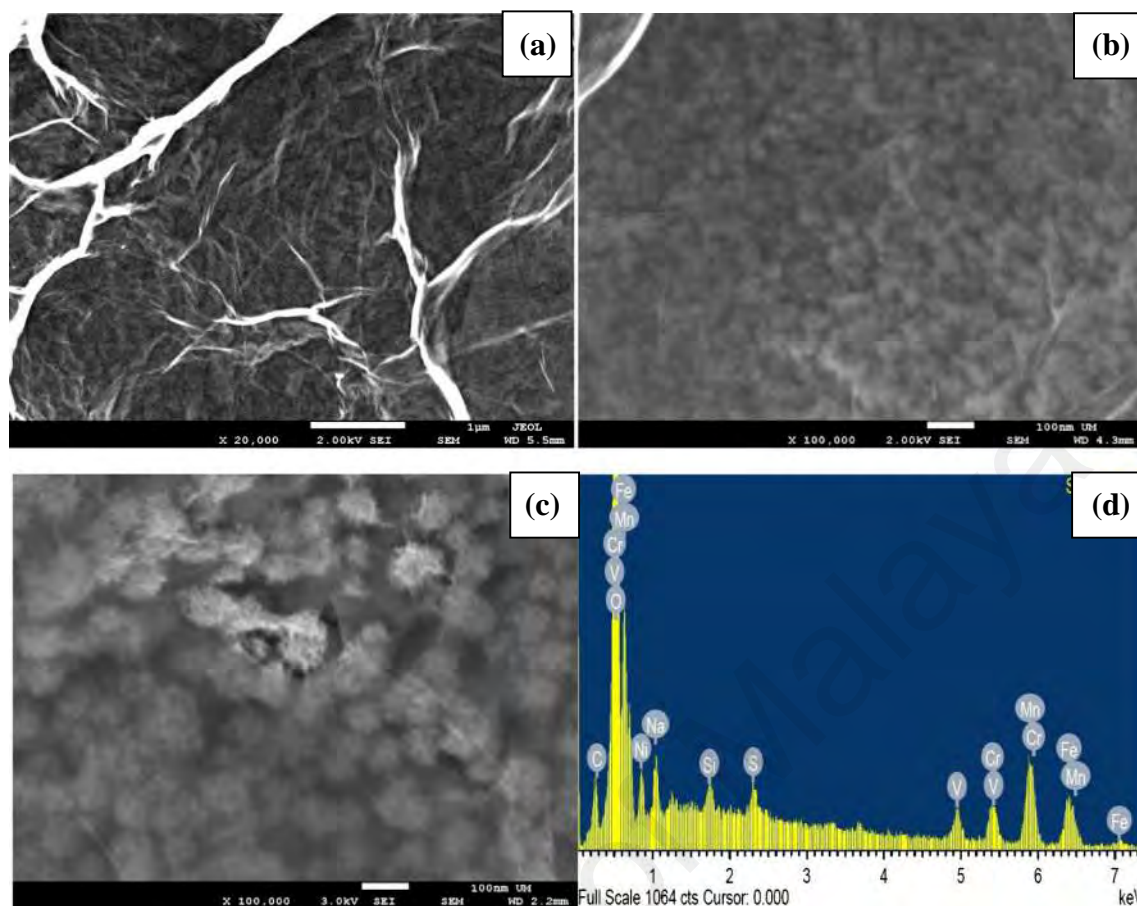


Fig. 2. FESEM images for (a) 10 min of deposition duration at 20K magnification, (b) 13 min of deposition duration and (c) 18 min of deposition duration at 100K magnification, (d) EDX result for 13 min of deposition duration.

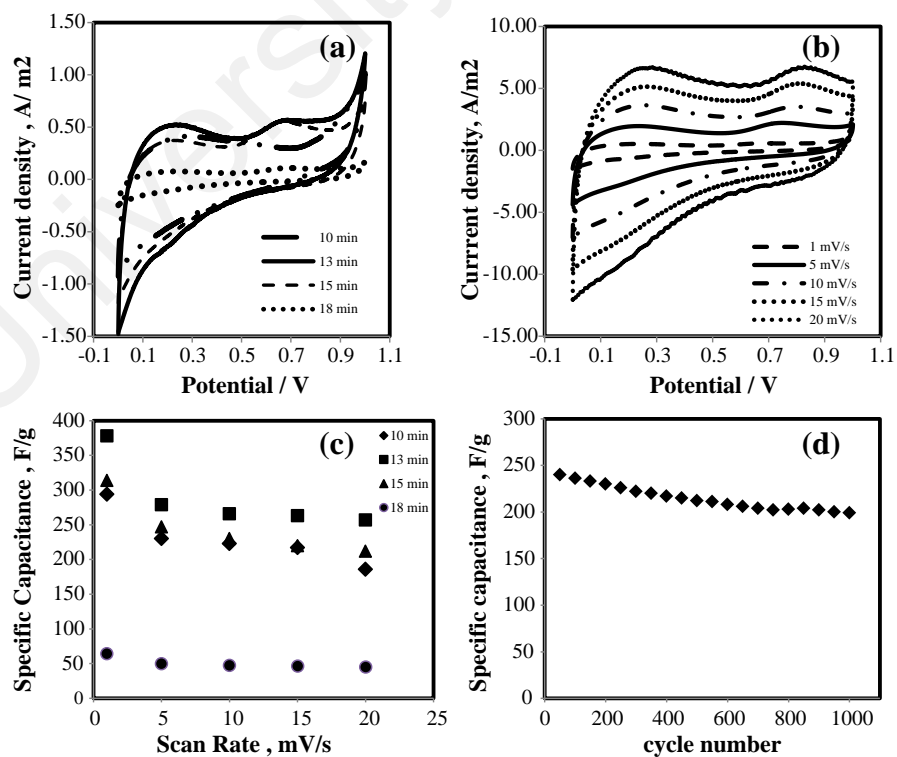


Fig. 3. (a) CV curves for all sample electrodes at a constant scan rate of 1 mV/s, (b) CV curve for 13 min of deposition duration for different scan rate, (c) graph specific capacitance versus scan rate for all sample electrodes and (d) specific capacitance versus cycle number for 13 min of deposition duration.

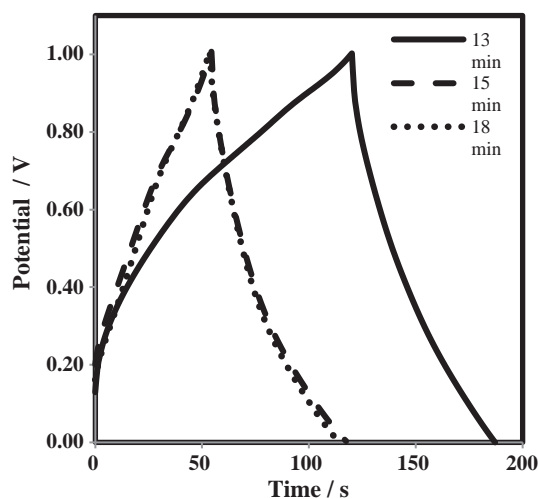


Fig. 4. Charge–discharge curve of all composite electrodes at a constant current of 1 mA.

be confined on the surface of the electrode. At low scan rate, the electrolyte ions are able to diffuse into deeper surface of the electrode [16].

At a scan rate of 10 mV/s, the cycle stability of the 13 minute-deposited composite electrode remains at a specific capacitance of 83% from the initial value. The energy density was calculated using the equation $E_{\text{density}} = 1/2(CV^2)/3600$ where the E_{density} = energy density, C = specific capacitance obtained in the previous calculation and V = potential window range. The energy density calculated for composite electrode with 13 min of deposition is 52.5 Wh/kg.

Fig. 4 compares the galvanostatic charge–discharge curves at a constant current of 1 mA for all electrode samples using 1.0 M Na_2SO_4 as electrolyte.

In comparison with 13, 15 and 18 min of electrodeposition, 13 minute-deposited electrode exhibits the longest discharging time. In other words, it can deliver more charges. This is consistent with the CV result at which the electrode has the optimum specific capacitance [17]. The observation from FESEM image also reveals that the 13 minute-deposited electrode has the optimum wrapping condition of MnO_2 particles by RGO sheet that allows more electrolyte ions to participate in the intercalation/deintercalation process. Thus, 13 minute deposited composite electrode is believed to be the best composite electrode in this work. In addition, the charge–discharge curve has almost symmetrical nature with slight curvature suggesting to the contribution of both double layer (EDLC) and pseudocapacitive in the charge storage mechanism of the composite electrodes.

4. Impedance analysis

The capacitive behavior of the composite electrode can be highlighted by analyzing the Nyquist plots in Fig. 5. A nearly vertical straight line at low frequency region of impedance data represents a capacitive behavior of the composite electrodes. The straight line closest to vertical is exhibited by the 13 minute-deposited composite electrode indicating it has the highest capacitive behavior among other electrodes and this behavior is due to the ion diffusive process of the electrolyte into the electrode. Furthermore, the diameter (d) of the depressed semicircle at high frequency region can be attributed to the charge transfer resistance. It was found that $d_{13} < d_{18} < d_{15} < d_{10}$, which indicates the best ion diffusion into the 13 minute-deposited electrode.

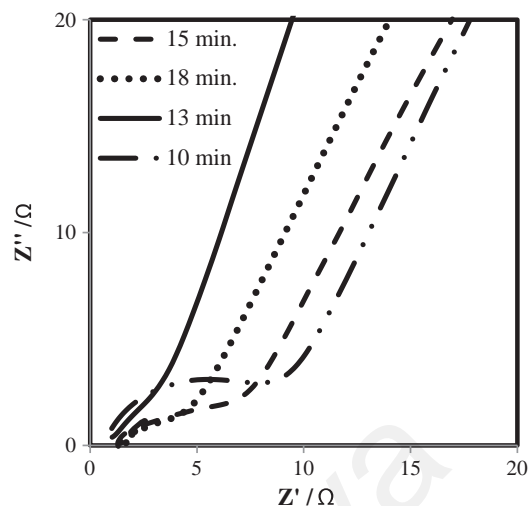


Fig. 5. Nyquist plot for all composite electrodes.

5. Conclusion

An RGO-wrapped MnO_2 composite electrode has been synthesized by simple electrodeposition technique using green reducing agent. Structure, morphology, elemental composition and electrochemical properties are evaluated for the potential application in supercapacitor. The best performance of the electrode is produced by 13 min of electrodeposition with the specific capacitance of 378 F/g at 1 mV/s. The capacitance retention of 83% after 1000 cycles indicates a good electrochemical stability. These results reveal the potential of RGO– MnO_2 composite as a promising electrode material for supercapacitor.

Acknowledgments

The authors acknowledge the University of Malaya for providing financial support through the project HIRG-J21002-73852 and PG010-2013A. Rusi thanks Skim Bright Spark University Malaya (SBSUM) for the scholarship awarded.

References

- [1] M.N. Patel, X. Wang, D.A. Slanac, D.A. Ferrer, S. Dai, K.P. Johnston, K.J. Stevenson, *J. Mater. Chem.* 22 (2012) 3160.
- [2] L. Tian, Q. Zhuang, J. Li, Y. Shi, J. Chen, F. Lu, S. Sun, *Chin. Sci. Bull.* 56 (2011) 3204.
- [3] X. Zhou, T. Shi, H. Zhou, *Appl. Surf. Sci.* 258 (2012) 6204.
- [4] T. Lv, L. Pan, X. Liu, T. Lu, G. Zhu, Z. Sun, *J. Alloys Compd.* 509 (2011) 10086.
- [5] J. Zhang, H. Yang, G. Shen, P. Cheng, J. Zhang, S. Guo, *Chem. Commun.* 46 (2010) 1112.
- [6] M. Kim, Y. Hwang, K. Min, J. Kim, *Phys. Chem. Chem. Phys.* 15 (2013) 15602–15611.
- [7] N.M. Huang, H.N. Lim, C.H. Chia, M.A. Yarmo, M.R. Muhamad, *Int. J. Nanomedicine* 6 (2011) 3443.
- [8] Z. Ji, X. Shen, G. Zhu, H. Zhou, A. Yuan, *J. Mater. Chem.* 22 (2012) 3471.
- [9] J. Elambasseril, R.N. Ibrahim, R. Das, *Compos. Part B Eng.* 42 (2011) 1596.
- [10] S. Hassan, M. Suzuki, A.A. El-Moneim, *Am. J. Mater. Sci.* 2 (2012) 11.
- [11] Y.J. Mai, D. Zhang, Y.Q. Qiao, C.D. Gu, X.L. Wang, J.P. Tu, *J. Power Sources* 216 (2012) 201.
- [12] B. Ding, X. Lu, C. Yuan, S. Yang, Y. Han, X. Zhang, Q. Che, *Electrochim. Acta* 62 (2012) 132.
- [13] L. Mai, H. Li, Y. Zhao, L. Xu, X. Xu, Y. Luo, Z. Zhang, W. Ke, C. Niu, Q. Zhang, *Sci. Rep.* 3 (2013).
- [14] M. Kim, Y. Hwang, J. Kim, *J. Power Sources* 239 (2013) 225.
- [15] M. Sawangphruk, P. Srimuk, P. Chiochan, A. Kritayavathananon, S. Luanwuthi, *J. Limtrakul, Carbon* 50 (2012) 5156.
- [16] M. Sawangphruk, S. Pinitsoontorn, J. Limtrakul, *J. Solid State Electrochem.* 16 (2012) 2623.
- [17] Z. Li, J. Wang, L. Niu, J. Sun, P. Gong, W. Hong, L. Ma, S. Yang, *J. Power Sources* 245 (2014) 224.

RESEARCH ARTICLE

Layer by Layer Ex-Situ Deposited Cobalt-Manganese Oxide as Composite Electrode Material for Electrochemical Capacitor

Rusi, P. Y. Chan, S. R. Majid*

Centre for Ionics University of Malaya, Department of Physics, Faculty of Science, University of Malaya, Kuala Lumpur, Malaysia

* shana@um.edu.my



OPEN ACCESS

Citation: Rusi, Chan PY, Majid SR (2015) Layer by Layer Ex-Situ Deposited Cobalt-Manganese Oxide as Composite Electrode Material for Electrochemical Capacitor. PLoS ONE 10(7): e0129780. doi:10.1371/journal.pone.0129780

Editor: Yogendra Kumar Mishra, Institute for Materials Science, GERMANY

Received: February 13, 2015

Accepted: May 12, 2015

Published: July 9, 2015

Copyright: © 2015 Rusi et al. This is an open access article distributed under the terms of the [Creative Commons Attribution License](https://creativecommons.org/licenses/by/4.0/), which permits unrestricted use, distribution, and reproduction in any medium, provided the original author and source are credited.

Data Availability Statement: All relevant data are within the paper.

Funding: The authors thank the University of Malaya for financial assistance through grants UM.C/625/11/ HIR/157, RP025B-14AFR, and PG010-2013A. Rusi acknowledges the Skim Bright Sparks University Malaya (SBSUM) for the scholarship award. The funders had no role in study design, data collection and analysis, decision to publish, or preparation of the manuscript.

Competing Interests: The authors have declared that no competing interests exist.

Abstract

The composite metal oxide electrode films were fabricated using ex situ electrodeposition method with further heating treatment at 300°C. The obtained composite metal oxide film had a spherical structure with mass loading from 0.13 to 0.21 mg cm⁻². The structure and elements of the composite was investigated using X-ray diffraction (XRD) and energy dispersive X-ray (EDX). The electrochemical performance of different composite metal oxides was studied by cyclic voltammetry (CV) and galvanostatic charge-discharge (CD). As an active electrode material for a supercapacitor, the Co-Mn composite electrode exhibits a specific capacitance of 285 Fg⁻¹ at current density of 1.85 Ag⁻¹ in 0.5M Na₂SO₄ electrolyte. The best composite electrode, Co-Mn electrode was then further studied in various electrolytes (i.e., 0.5M KOH and 0.5M KOH/0.04M K₃Fe(CN)₆ electrolytes). The pseudocapacitive nature of the material of Co-Mn lead to a high specific capacitance of 2.2 x 10³ Fg⁻¹ and an energy density of 309 Whkg⁻¹ in a 0.5MKOH/0.04MK₃Fe(CN)₆ electrolyte at a current density of 10 Ag⁻¹. The specific capacitance retention obtained 67% of its initial value after 750 cycles. The results indicate that the ex situ deposited composite metal oxide nanoparticles have promising potential in future practical applications.

Introduction

Electrochemical supercapacitors are appealing as devices for storing electrical energy, because they can deliver power at higher rates than batteries and higher energy density than conventional capacitors [1–3]. They can also be classified by their charge storage mechanism (i.e., as electrical double layer capacitors (EDLC) and pseudocapacitors). The energy storage mechanism of EDLC depends on the accumulated charge at the electrode-electrolyte interface. Pseudocapacitors are being developed in order to improve energy density through the storage mechanism of intercalation/deintercalation cations from the electrolyte into the electrode. In pseudocapacitors, the joint action of non-Faradic double-layer charge storage processes and redox reactions results in high capacitance and energy storage density [4–7]. A lot of materials have been studied as potential electrode materials for supercapacitors including (1)

carbonaceous materials, (2) conducting polymers, and (3) transition metal oxides [7, 8]. Out of these materials, metal oxide electrode materials have attracted considerable interest because of their large capacitance and fast redox kinetics. There are some other fields of studies, such as optical, membrane fusion, and magnetron sputtering, that have utilized metal oxides to obtain a higher level of performance [9–12]. Metal oxide materials such as MnO_2 , NiO , Co_3O_4 , and VO are commonly used as candidate materials for pseudocapacitor electrodes [5–6].

MnO_2 has received attention because its physical and chemical properties can be used to make relatively high quantities of low-cost, non-toxic pseudocapacitors with a high specific capacitance value [7, 13–14]. However, as a supercapacitor electrode material, MnO_2 is still hampered by its poor electrical conductivity and material dissolution during electrochemical cycling, which leads to a severe specific capacitance drop as the scan rate increases. To mitigate these problems, many measures such as making nanocomposites and carbon-mixing have been carried out [7, 14]. To obtain nanocomposite compounds, the primary MnO_2 metal oxide can be incorporated with secondary/ternary metal oxide materials [7, 15]. In this case, an electrode containing mixed metal oxides performs better than a single transition metal oxide when it is used as the electrode in a supercapacitor [15]. For instance, F. Gobal and S. Jafarzadeh [16] employed the deposition method to obtain binary cobalt-manganese oxides on stainless steel substrate, and the ex situ deposited metal oxide showed higher specific capacitance than a single deposited metal oxide. However, the morphology changes and the effect of the second layer have not been studied. According to Lee et al. [17], binary manganese-nickel (Mn-Ni) oxide films in situ electrodeposited from a bath consisting of manganese acetate and nickel chloride on a graphite sheet can achieve a specific capacitance of 424 Fg^{-1} in Na_2SO_4 electrolyte at a scan rate of 20 mVs^{-1} . In the work of Prasad and Miura [18], the addition of cobalt oxide showed an improved specific capacitance of the manganese oxide electrode. The purpose of this work is to investigate the electrochemical characteristics of a composite MnO_2 -based electrode that has been prepared by the ex situ electrodeposition technique. We have chosen to use the electrodeposition technique due to several advantages provides, such as being simple to set up, requiring low deposition temperature, allowing for easy control of the deposited thickness, consuming less energy, and being fast to be carry out [19]. A layer of MnO_2 was used as a first layer, followed by the ex situ deposition of a second layer containing mixed metal hydroxide solutions, such as $\text{Co}(\text{OH})_2$, NiOH , and $\text{Mn}(\text{OH})_2$, performed according to the chronopotentiometry method. The influence of the second layer on the morphological structure and the electrochemical performance of the best electrode tested in different electrolytes are also discussed within this study.

Experimental

Materials

In this work, manganese acetate tetrahydrate ($\text{Mn}(\text{CH}_3\text{COO})_2 \cdot 4\text{H}_2\text{O}$) and nickel acetate tetrahydrate, ($\text{Ni}(\text{CH}_3\text{COO})_2 \cdot 4\text{H}_2\text{O}$), were purchased from Aldrich and used without further purification. Cobalt sulphate ($\text{CoSO}_4 \cdot 7\text{H}_2\text{O}$) and sulphuric acid H_2SO_4 were obtained from Unilab and Friendemann Schmidt, respectively.

Electrodeposition

The electrodeposition was conducted under ambient conditions at 27°C with a three-electrode configuration in chronopotentiometry mode using an Autolab PGSTAT30. Stainless steel (SS), Ag/AgCl and carbon rod were respectively used as the working, reference and counter electrodes. The area of the working electrode in contact with the solution was fixed at 4 cm^2 . The first layer was made up of manganese hydroxide particles electrodeposited from a 0.01M of Mn

Table 1. List of deposition solutions for the second layer.

Sample	Deposition solution
Co-Mn	6ml of 0.8 M of H ₂ SO ₄ +30 ml of 0.01M Mn(CH ₃ COO) ₂ .4H ₂ O+30 ml 0.15M CoSO ₄ .7H ₂ O
Ni-Mn	6ml of 0.8M H ₂ SO ₄ +30ml of 0.01M Mn(CH ₃ COO) ₂ .4H ₂ O+30ml of 0.25M Ni(CH ₃ COO) ₂ .4H ₂ O
Co-Ni	6ml of 0.8M H ₂ SO ₄ +30 ml 0.15M CoSO ₄ .7H ₂ O+30ml of 0.25M Ni(CH ₃ COO) ₂ .4H ₂ O
Co-Ni-Mn	6ml of 0.8M of H ₂ SO ₄ +20ml of 0.01M Mn(CH ₃ COO) ₂ .4H ₂ O+20ml of 0.25M Ni(CH ₃ COO) ₂ .4H ₂ O+20 ml 0.15M CoSO ₄ .7H ₂ O

doi:10.1371/journal.pone.0129780.t001

(CH₃COO)₂.4H₂O aqueous solution for 300s [20]. The current density was fixed at 2 mAcm⁻² and the obtained sample was further heated at 150°C for 6 hours. The second layer was electro-deposited on the first layer after the sample was cooled to 27°C. The deposition current density was fixed at 2 mA cm⁻² for 300s using the different deposition solutions listed in Table 1.

Lastly, all of the prepared electrodes were rinsed with distilled water and heated at 300°C for 6 hours before further characterization. The sample preparation and measurements are reproducible.

Characterization

The morphology of the deposited film was investigated using field emission scanning electron microscopy (FESEM), Joel JSM-7600F, and transmission electron spectroscopy (TEM) Jeol JEM-2100F. The crystal structure of deposited metal oxide and powder from the selected sample scraped off the SS was examined by an X-ray diffraction (XRD) D8 Advance X-Ray diffractometer-Bruker AXS using CuK_α monochromatized radiation at 40 kV and 40 mA at ambient temperature. The electrochemical performance was examined using electrochemical impedance spectroscopy (EIS), cyclic voltammetry (CV) and charge-discharge (CD) studies. All the electrochemical tests were set up with three electrode systems: prepared electrode as working electrode, platinum as a counter electrode, and Ag/AgCl as a reference electrode. The electrochemical impedance spectroscopy (EIS) tests were performed at a frequency of 0.1Hz to 100 kHz at applied AC potential of 0 V.

Results and Discussion

Morphological and structural studies

FESEM and TEM analyses were carried out to probe the surface structural identities of Co-Mn, Ni-Mn, Co-Ni, and Co-Ni-Mn deposited samples. The FESEM images are displayed in Figs 1 and 2. As can be seen from the low magnification image of all samples, most of the deposited particles are spherical in shape. The sizes of the spherical particles are in the range of 100 to 400 nm. The contiguous particles are only observed in the FESEM images of Ni-Mn and Ni-Co-Mn, shown in Fig 1B and 1C, which tended to form large agglomerated particles. The surface of the particles exhibits a nanoflake-like structure, which is influenced by the nucleation process of the second electrodeposited layer. As shown in Fig 2, higher magnification of TEM images reveals that a flower-like structure is clearly seen in all samples. The thickest layer of the flower-like structure at the outer particles (40–70 nm) is observed in the Co-Mn sample (Fig 2A and 2B), which may be constructive for ion intercalation. The interplanar spacing of Co-Mn is shown in Fig 2C. The periodic lattice fingers' distance of 0.21 nm and 0.31 nm might attributed to the interplanar spacing of the (301) and (310) MnO₂ plane, while 0.25 nm belongs to the (311) plane of Co₃O₄ [20–21]. In the deposited Ni-Mn and Ni-Co-Mn samples (Fig 2D and 2F), the flower-like structure overlaps because of the adjoining particles, as evidenced in the FESEM results. The overlapping of the flower-like structure can limit the cation

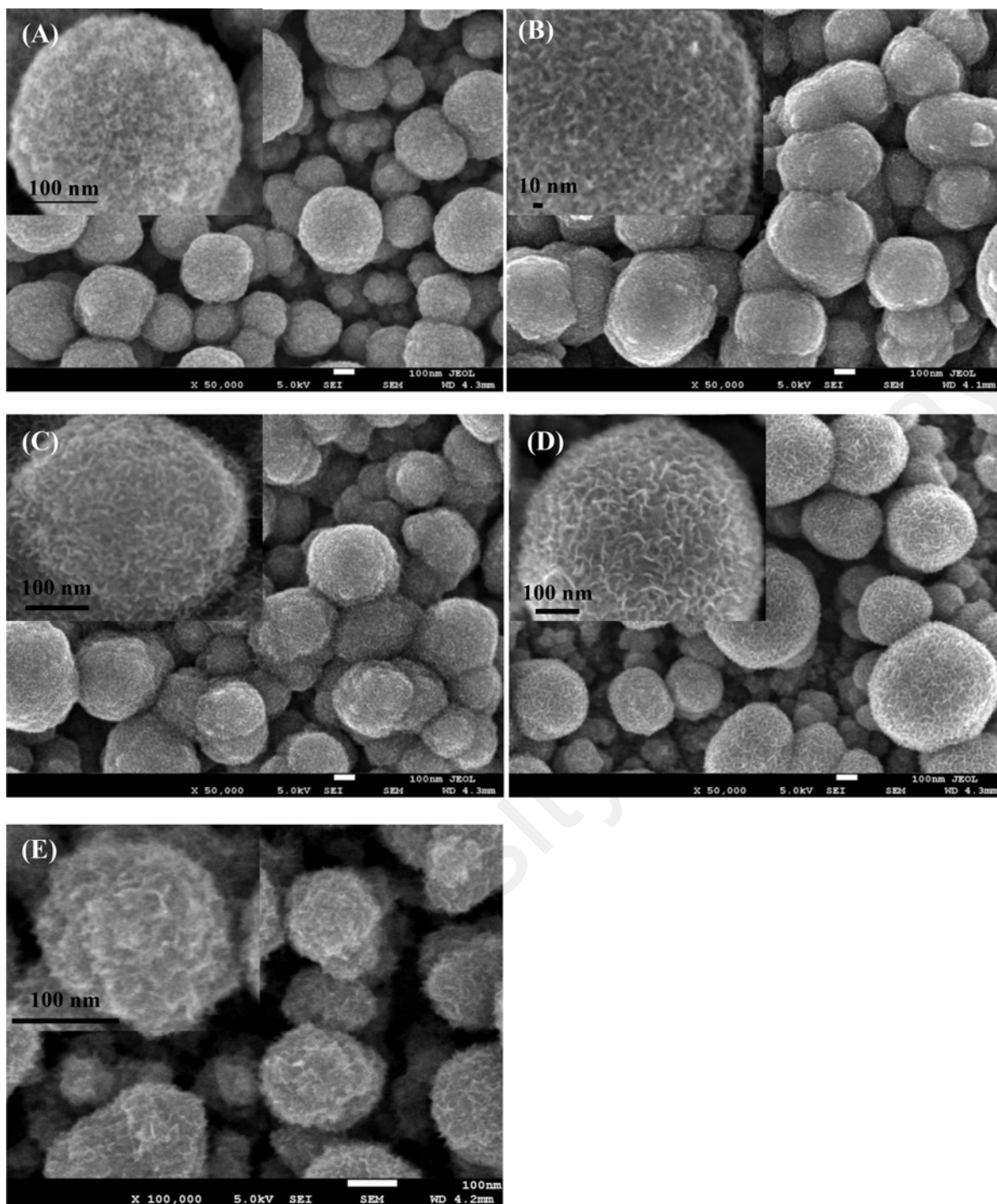


Fig 1. FESEM images at high and low magnification: (A) Co-Mn, (B) Ni-Mn, (C) Co-Ni-Mn, (D) Co-Ni, and (E) first layer of deposited MnO₂.

doi:10.1371/journal.pone.0129780.g001

intercalation in the electrode matrix and leads to low electrochemical performance. The presence of spherical particles can be attributed to the instantaneous nucleation at all available sites during the first electrodeposition of MnO₂ step (Fig 1E). The development of various textures on the flower-like structure on top of MnO₂ is influenced by the progressive nucleation from

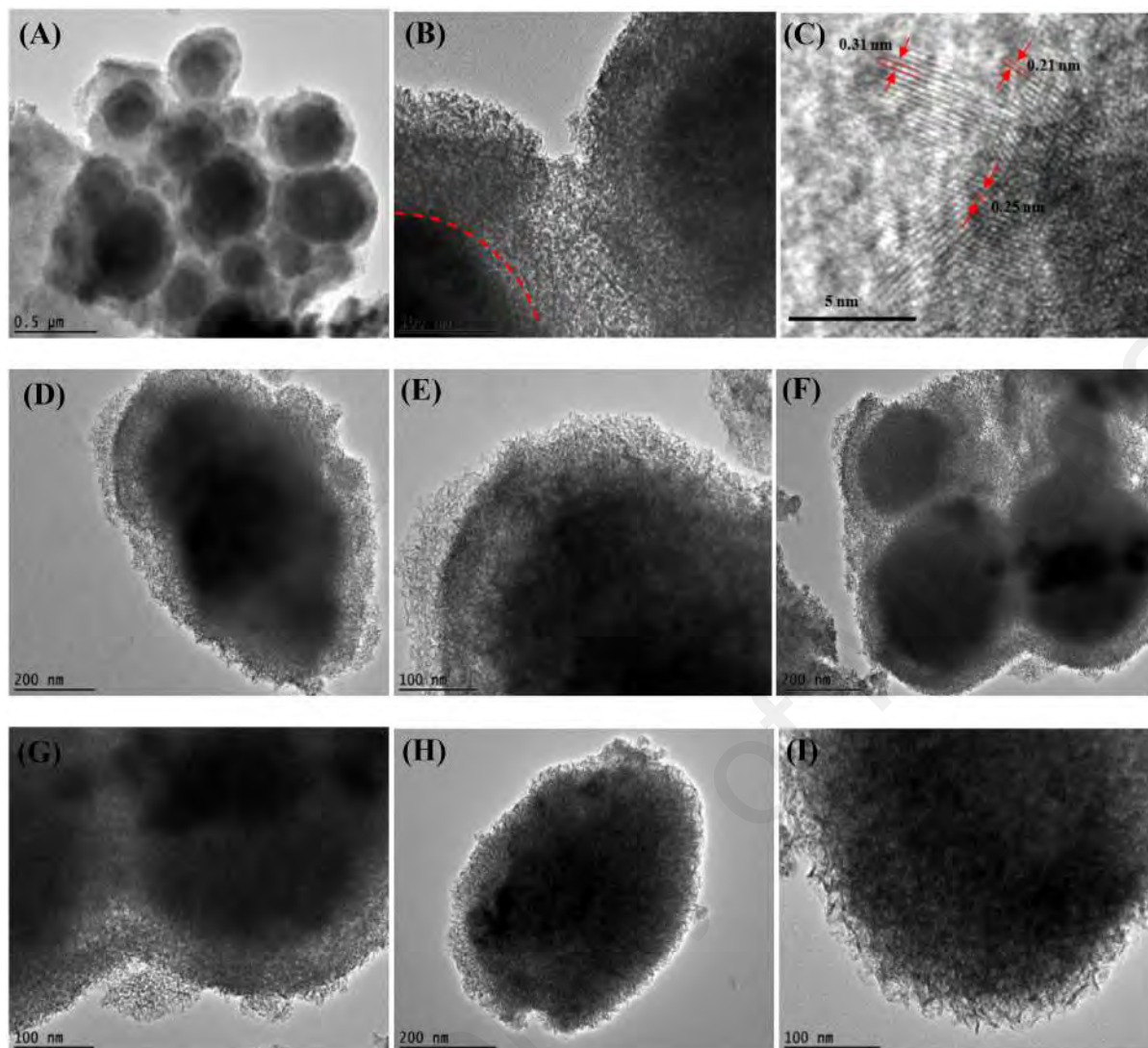


Fig 2. TEM images at low and high magnification: (A-B) Co-Mn, (C) inter-planar lattice spacing of Co-Mn, (D-E) Ni-Mn, (F-G) Co-Ni-Mn, and (H-I) Co-Ni.

doi:10.1371/journal.pone.0129780.g002

the second electrodeposition step. Previous studies [22–23] reported that progressive nucleation occurs on a larger number of active sites than instantaneous nucleation does, and it not only forms on the substrate surface but also on previously formed nuclei, resulting in the growth of compact grains. The growth of thicker, more compact grains in Ni-Mn and Ni-Co-Mn samples caused the overlapping of the particles.

The elemental identity of the deposited metal oxide on SS was confirmed by XRD. No significant peaks could be observed from the XRD patterns of all deposited electrodes on SS substrate (Fig 3A). This absence is attributed to the thin amorphous deposited sample [24]. Fig 3B shows the XRD pattern of scraped-off powder from Co-Mn deposits on SS, which was collected after the second electrodeposition step. The peaks at $2\theta = 29.1^\circ$, 37.3° , 42.5° and 56.6° in the XRD pattern of deposited MnO_2 from the first electrodeposition step confirm the formation of $\alpha\text{-MnO}_2$ with planes of (310), (211), (301), and (600), respectively (JCPDSNO.44-0141) [25]. A low intensity peak around $2\theta = 38.5^\circ$ corresponding to the (222) plane of Co_3O_4 (JCPDS

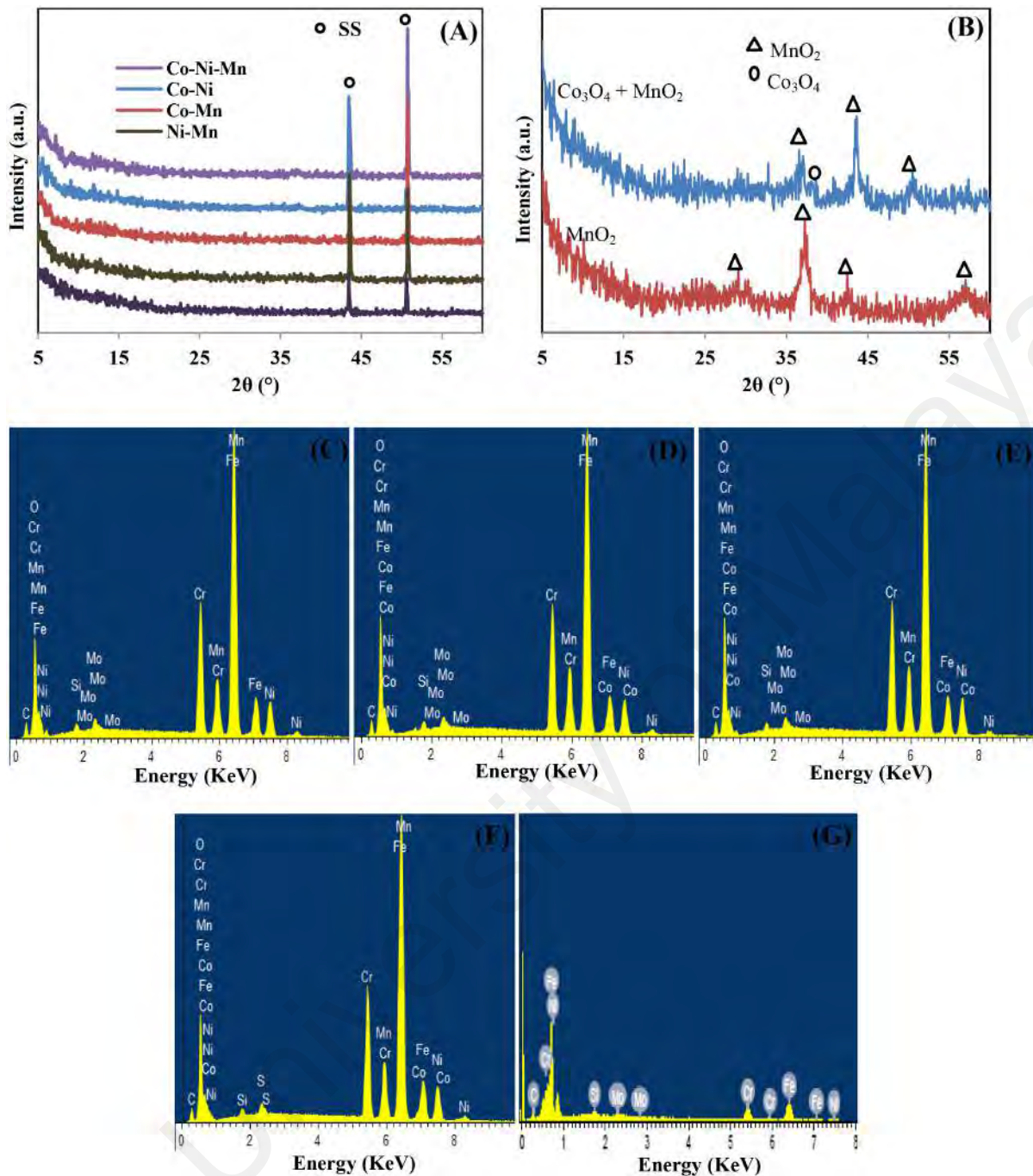


Fig 3. (A) XRD pattern of all deposited electrodes on top of SS, **(B)** XRD pattern of scraped off powder of MnO₂ deposits (first electrodeposition) and scraped-off powder of Co-Mn deposits after the second electrodeposition step, EDX images of: **(C)** Co-Mn, **(D)** Ni-Mn, **(E)** Co-Ni-Mn, **(F)** Co-Ni, and **(G)** Empty SS.

doi:10.1371/journal.pone.0129780.g003

No. 76–1802) [26] is detected at the point when the second layer composed of Co-Mn was deposited on the MnO₂ particle layer, and other peaks at 2θ = 37.3°, 42.5°, and 50.6° belong to (211), (301), and (411) planes of α-MnO₂ peaks [25]. The broad nature and weak relative intensity of the Co₃O₄ peak imply a small size of Co₃O₄ and the amorphous nature of

deposits, which is feasible for a supercapacitor application [24, 27–28]. The elemental composition has been confirmed from EDX studies (Fig 3C to 3G). The presence of C, Cr, Fe, Si, Mo, and some element traces of Ni were detected from empty SS.

Electrochemical studies

The electrochemical performance of the electrode materials can be influenced by the morphology of materials, so the prepared electrodes were subjected to cyclic voltammetry (CV), charge-discharge (CD), and impedance tests to investigate the effect of the second electrodeposited layer on the electrochemical performance of MnO₂-based electrodes. The metal oxide electrode can store charges at the electrode/electrolyte interface, and a redox reaction takes place in the alkaline electrolyte. The cyclic voltammetry curves of all samples in a potential window of 0-1V using a 0.5 M Na₂SO₄ electrolyte at a scan rate of 1 mVs⁻¹ are displayed in Fig 4A. CV curves show well-defined redox peaks indicating the significant contribution of faradic behaviour than the EDLC. The maximum area under the curve is obtained from the CV curves of the Co-Mn sample. The specific capacitance can be calculated from the CV curve with the

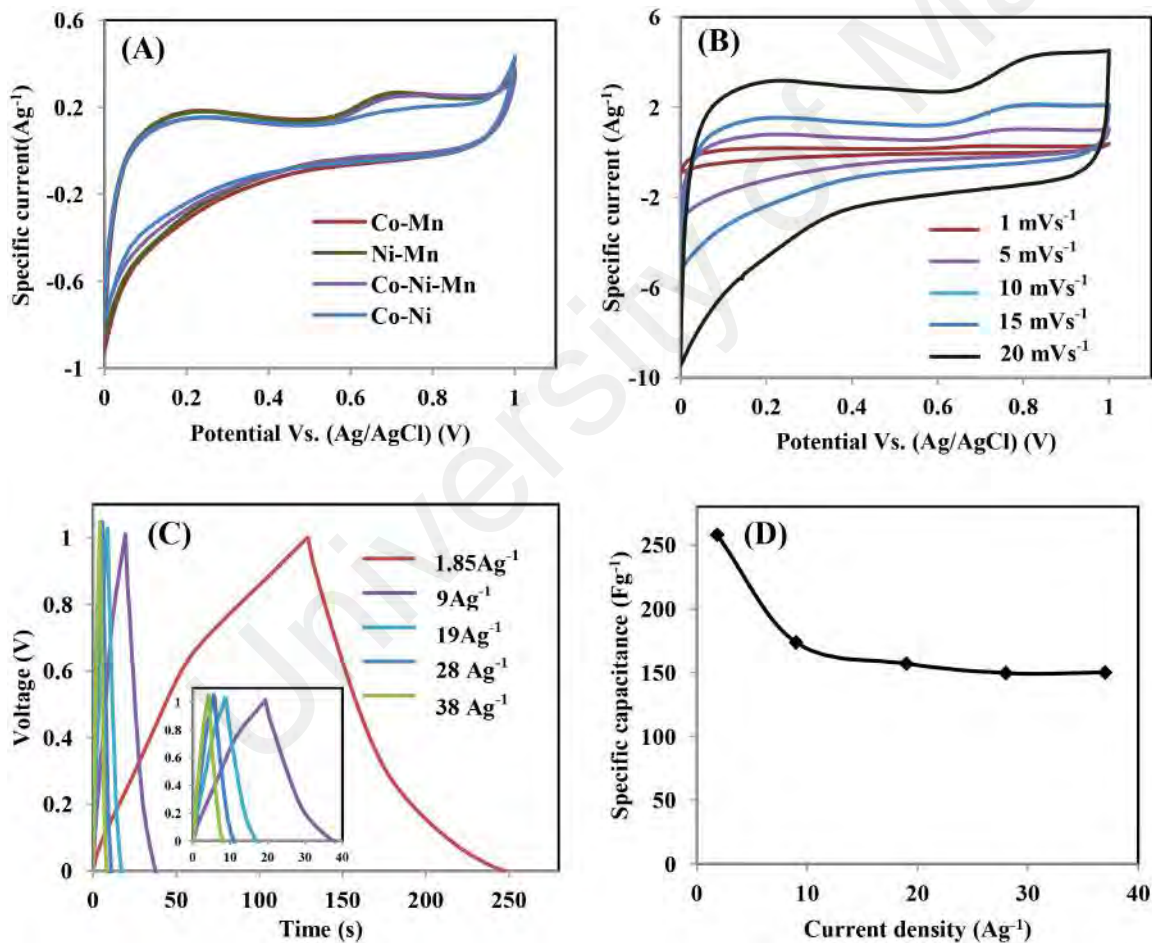


Fig 4. (A) CV curve of all deposited electrodes at 1 mVs⁻¹, (B) CV curve of the best Co-Mn deposited electrode at different scan rates, (C) charge-discharge performance of Co-Mn electrode at different current densities in 0.5M Na₂SO₄ electrolyte, (D) the specific capacitance calculated at different current densities.

doi:10.1371/journal.pone.0129780.g004

following equation: Eq 1:

$$C = \frac{\int I dt}{\Delta E x m} \quad (1)$$

where I is the oxidation/reduction current, dt is time differential, m is the mass of active material and ΔE is the operating potential.

The calculated specific capacitance values for Co-Mn, Ni-Mn, Co-Ni-Mn, and Co-Ni samples are 186 Fg^{-1} , 169 Fg^{-1} , 156 Fg^{-1} , and 153 Fg^{-1} , respectively. Hence, the Co-Mn sample is identified as the best electrode in the present study. To further understand the capacity behaviour of this sample, the cyclic voltammetry curves were run at different scan rates, as illustrated in Fig 4B. As the scan rate increased, the specific capacitance reduced by 20% from 186 Fg^{-1} to 149 Fg^{-1} at a scan rate of 1 mVs^{-1} and 20 mVs^{-1} , suggesting good electrode properties [29].

The charge-discharge measurement of the Co-Mn electrode was conducted from 0–1 V, using the same electrolyte (see Fig 4C). The specific capacitance from the discharging curve can be calculated using Eq 2:

$$C = \frac{I}{\frac{dE}{dt} x m} \quad (2)$$

where I is the discharge current, dE/dt is the change of discharge potential with the discharge time and m is mass of active materials.

The electrode can deliver a high specific capacitance of 258 Fg^{-1} at a current density of 1.85 Ag^{-1} . Furthermore, a specific capacitance of 150 Fg^{-1} is still retained at a very high current density of 37 Ag^{-1} , implying good specific capacitance retention behavior. (Fig 4D). The specific capacitance decreases as the increasing scan rate or current density reveals the minimum utilization of active materials. At higher scan rates or higher discharge constant currents, the Na^+ ions reach only the outer surface of the electrode; the active material at the inner surface does not get fully involved in the electrochemical process [20, 28].

The best electrochemical performance is in deposited film with Co-Mn as a second layer and the success of this performance could be attributed to the following reasons: (1) the small particle size and no agglomeration between the particles increases the surface area of the electrode; (2) the thicker porous layer at the outer surface of the nanosphere facilitates fast electron transport paths for diffusion of the electrolyte into electroactive materials; (3) homogeneous distribution of the flower-like structure at the outer sphere surface might strongly improve the conductivity and contribute to high capacitance [28].

Fig 5A shows an impedance plot of all deposits recorded in the $0.5\text{M Na}_2\text{SO}_4$ electrolyte in a frequency range from 0.1 Hz to 100 kHz with a potential of 0V. The measured impedances were analyzed using a Nyquist plot, and the impedance data were employed to estimate quantities of the elements of the equivalent circuit by using Nova simulation software (Fig 5B). Generally, the impedance plot of supercapacitors can be divided into three regions according to processes, such as equivalent series resistance (ESR, R_s), transfer resistance (R_{ct}), and the Warburg diffusion region. The R_s value is obtained at the intercept of the high frequency of the impedance plots on the x-axis (Fig 5A) and represents the electrolyte resistance, intrinsic resistance of the electrode, and the contact resistance of metal oxide-current collector interfaces [30]. The R_s value of Co-Mn, Ni-Mn, Co-Ni-Mn and Co-Ni electrodes are 1.12, 1.27, 1.20, and 1.21Ω , respectively. The high-frequency arc corresponds to the charge transfer resistance (R_{ct}), which is caused by a faradic reaction between electrode/electrolyte interface and can be determined by arc semicircle diameter [30–31]. It was found that the sum of series resistance and transfer resistance ($R_s + R_{ct}$) values of the Co-Mn electrode is lower than that of the Ni-Mn,

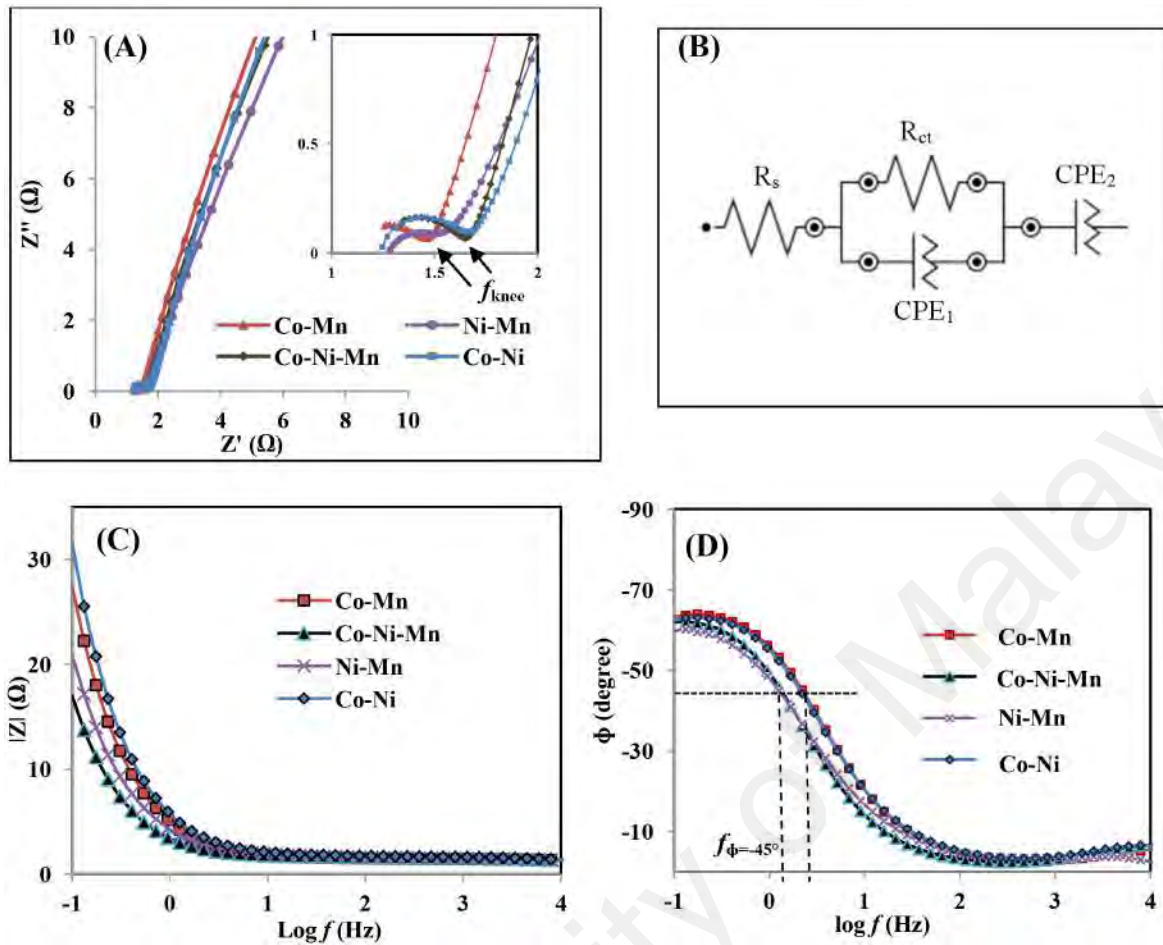


Fig 5. (A) Nyquist plots, (B) Simulation equivalent circuit, (C) frequency versus impedance magnitude, (D) frequency versus phase angle for all deposited samples.

doi:10.1371/journal.pone.0129780.g005

Co-Ni-Mn, and Co-Ni electrodes, as shown in Table 2. Overall, the impedance of the Co-Mn electrode is smaller than others (evidenced by smaller R_s and R_{ct}), which indicates that the cation insertion/extraction process into/from Co-Mn is more efficient than in the case of other electrodes, which might be due to the improved wettability properties. In the Warburg region, the smaller angle between the straight line portion at the low-frequency region and the real x-axis implies that there is a longer diffusion path length, which leads to a greater ion movement's hindrance [32–33]. The biggest angle of Co-Mn indicates the faster ion diffusion of electrolytes than in Ni-Mn, Co-Ni-Mn, and Co-Ni electrodes, which implies a better electrochemical performance. The knee frequency (f_{knee}) represents the maximum frequency

Table 2. Resistance and frequency values obtained from EIS for all deposited film.

Sample	R_s (Ω)	R_{ct} (Ω)	$R_s + R_{ct}$ (Ω)	f_{knee} (Hz)	$f_{\phi = -45^\circ}$ (Hz)	R_s (Ω) (simulation)	R_{ct} (Ω) (simulation)
Co-Mn	1.12	0.35	1.47	356	2.22	1.07	0.23
Ni-Mn	1.27	0.37	1.64	268	1.26	1.28	0.31
Co-Ni-Mn	1.20	0.46	1.67	202	1.27	1.19	0.47
Co-Ni	1.21	0.49	1.70	268	2.09	1.16	0.58

doi:10.1371/journal.pone.0129780.t002

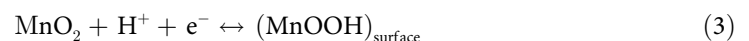
that the stored energy can fully access. The determined f_{knee} value is as high as 356 Hz for Co-Mn and showed a good frequency response, indicating that this electrode has higher power capability and can be rapidly charged [34]. For further investigation, the electrode can be represented by an equivalent circuit, Fig 5B. In the circuit in this study, CPE_1 and CPE_2 were used to replace the double-layer capacity and Warburg diffusion impedance, respectively [35]. The simulation impedance values are close to the experimental values (see Table 2).

The bode plots shown in Fig 5C and 5D are the frequency dependence on impedance magnitude ($|Z|$) and phase angle (ϕ) of all deposited films. A typical capacitive characteristic of the electrode can be manifested from the analysis of these plots, which can be divided into three main segments [36–37]. In the first segment, at low frequency region ($f < 1$ Hz), all the samples exhibit a slope of ~ -1 in the plot $\log f$ versus ($|Z|$) and the phase angle between -70° and -45° in the plot $\log f$ versus (ϕ), showing the capacitive characteristic. In the second segment, at intermediate frequency region, with a high frequency value at $\phi = -45^\circ$, represents a better capacitive response (Fig 5D). From this figure, it is seen that the deposited electrode of Co-Mn exhibits the highest frequency value of 2.22 Hz, indicating that it has a fast response time compared to other electrodes (see Table 2) [34] and results in a high specific capacitance of the Co-Mn electrode. This impedance study is in agreement with the CV and CDC results. In the third segment, at high frequency ($f > 10$ Hz), the phase angle starts to decrease from 20° to \sim zero with increasing frequency.

Electrolyte study

To further investigate the performance of the Co-Mn electrode in different alkaline electrolytes, cyclic stability tests for 750 cycles at a scan rate of 10 mVs^{-1} were performed (Fig 6A). The specific capacitance retention of Co-Mn in Na_2SO_4 , KOH and mixed KOH/ $\text{K}_3\text{Fe}(\text{CN})_6$ electrolytes after 750 cycles was 57%, 29%, and 67%, respectively. Low capacitance retention over 750 cycles could be attributed to high degradation of the electrode, resulting from the high current passed through during the cyclability test and volume loss of active materials [38]. In comparison with the Na_2SO_4 electrolyte, KOH is less stable for the Co-Mn electrode. However, the capacitance retention of the Co-Mn electrode in KOH is remarkably enhanced when 0.4M $\text{K}_3\text{Fe}(\text{CN})_6$ is added to the KOH electrolyte. The retention test of the Co-Mn electrode was further studied at a higher scan rate of 100 mV s^{-1} in a mixed KOH/ $\text{K}_3\text{Fe}(\text{CN})_6$ electrolyte, as shown in Fig 6B. The specific capacitance retained 43% of initial capacitance value after 3500 cycles. However, the long term cycling test changed the morphology of the Co-Mn electrode (Fig 6B insert) and caused the loss of specific capacitance retention.

The cyclic voltammograms of the obtained Co-Mn electrode were recorded in 0.5M Na_2SO_4 , 0.5 M KOH, 0.04M $\text{K}_3\text{Fe}(\text{CN})_6$, and mixed 0.5M KOH/0.04M $\text{K}_3\text{Fe}(\text{CN})_6$ electrolytes by sweeping the potential from -0.5V to 0.5V at a scan rate of 5 mVs^{-1} , as shown in Fig 6C, 6D and 6E. In the case of the Na_2SO_4 electrolyte (Fig 6C), a CV curve with a well-defined pair of anodic peaks (A_0) and a cathodic peak (C_0) centered at +0.22 and -0.12 V (vs. Ag/AgCl) was observed. These peaks correspond to the redox reaction dominated by MnO_2 , according to Eqs 3–4 [4]:



or



(K: cations in electrolyte (i.e., Na^+ or K^+))

The KOH electrolyte is known to be a better electrolyte for Co_3O_4 materials than Na_2SO_4 aqueous solution, due to the higher OH^- concentration in the electrolyte solution. OH^- ions

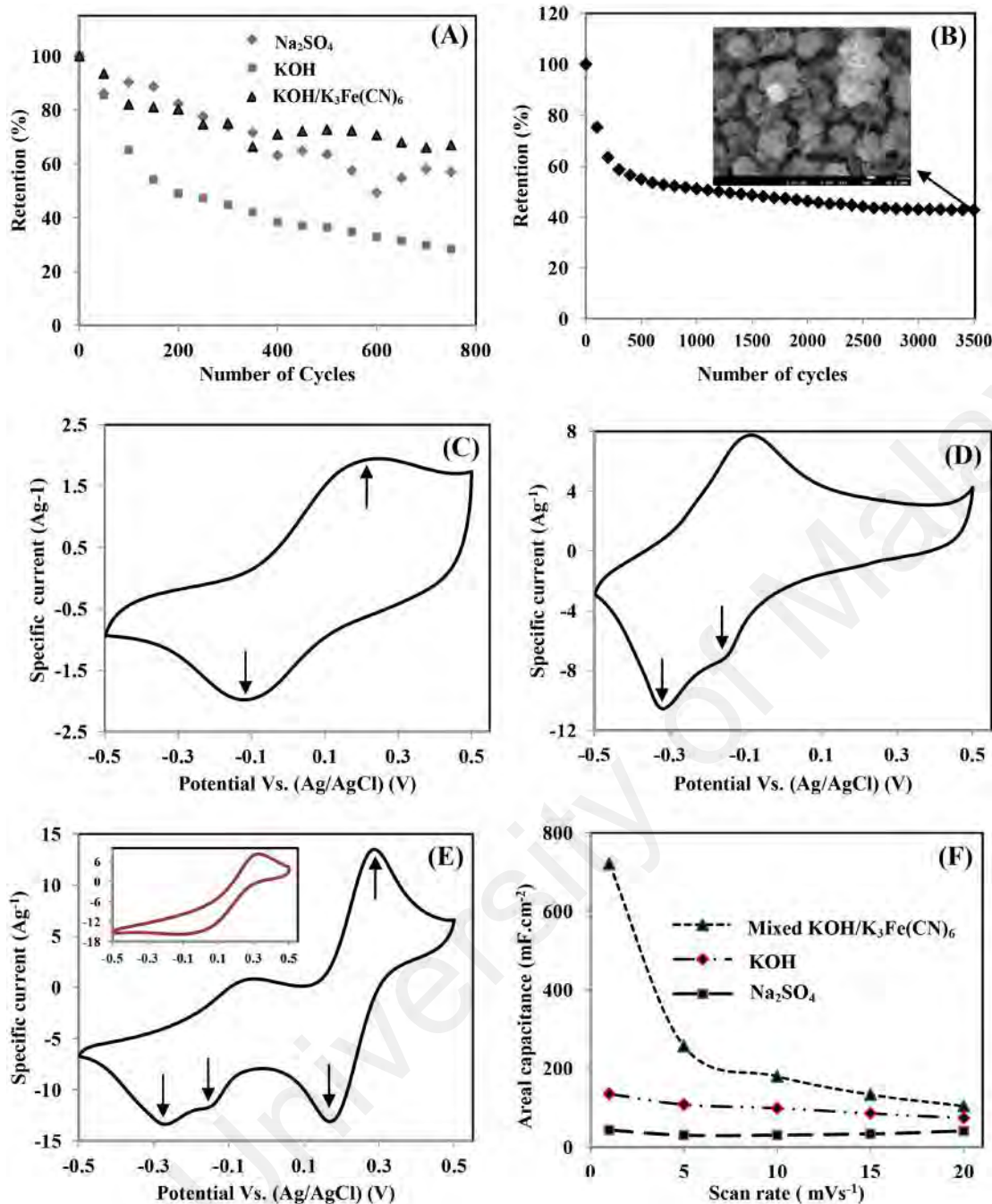


Fig 6. Electrochemical stability at voltage range of -0.5V 0.5V in: (A) three different electrolytes at a scan rate of 10 mVs⁻¹ until 750 cycles, (B) mixed 0.5M KOH/0.04M K₃Fe(CN)₆ electrolyte at a scan rate of 100 mVs⁻¹ until 3500 cycles and The FESEM images after 3500 cycles (insert), CV responses of Co-Mn in different electrolytes: (C) 0.5M Na₂SO₄, (D) 0.5M KOH, (E) mixed 0.5M KOH/0.04M K₃Fe(CN)₆ electrolyte (inset: bare 0.04M K₃Fe(CN)₆ electrolyte) in voltage range of -0.5 V to 0.5 V at scan rate of 5 mVs⁻¹, and (F) the specific capacitance per surface area of Co-Mn electrodes in three different electrolytes at varying scan rates.

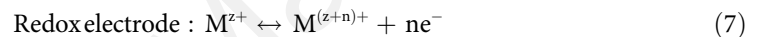
doi:10.1371/journal.pone.0129780.g006

play an important role in Co₃O₄ reaction [19,39] during charging/discharging (Eq 5).



The combined contribution of $\text{MnO}_2\text{-Co}_3\text{O}_4$ in the KOH electrolyte (Fig 6D), is supported by the appearance of C_0 peaks at -0.14 and -0.31 V, according to reactions shown in Eqs 3–5. The increment of current response in the KOH electrolyte is also attributed to the K^+ ion's smaller cation radius (3.31 Å) compared to Na^+ ions (3.35 Å), as well as the higher conductivity of K^+ ions (73 $\text{cm}^2/\Omega \text{ mol}$) than Na^+ ions (50 $\text{cm}^2/\Omega \text{ mol}$). Easy passage of K^+ ions into the electrode matrix during the charging process is achieved because it has a smaller radius and faster ion movements [40].

When KOH is replaced with mixed KOH/ $\text{K}_3\text{Fe}(\text{CN})_6$ electrolyte, as in Fig 6E, an additional pair of anodic peaks at +0.27V (A_{02}) and a cathodic peak at +0.17V (C_{02}) are detected, which can be attributed to the redox reaction of $\text{K}_4\text{Fe}(\text{CN})_6$ to $\text{K}_3\text{Fe}(\text{CN})_6$, and it is consistent with the CV plot of bare $\text{K}_3\text{Fe}(\text{CN})_6$ electrolyte (insert picture) [39]. In this system, there are two types of charge storage reaction that could contribute to the capacitance. The first reaction is originated from the redox couple of $[\text{Fe}(\text{CN})_6]^{3-} / [\text{Fe}(\text{CN})_6]^{4-}$ in the electrolyte (Eq 6). The second type of charge storage can be derived from the redox reaction in highly electroactive electrodes (Eq 7). The reaction can be written as follows [41]:



Where M is the Co^{2+} or Mn^{2+} cations, and $1 \leq n \leq z$.

Other than the electrode redox reaction of Co-Mn oxide in the KOH electrolyte, the hexacyanoferrate ions also play a role as “electron shuttles” in the charging/discharging process [42]. When the electrode is charged, $[\text{Fe}(\text{CN})_6]^{3-}$ will accept the electron via the reduction of hexacyanoferrate (III) to (II), the hexacyanoferrate ions of which act as “electron carriers” (Fig 7A). When the reaction is reversible, the hexacyanoferrate ions act as “electron donors” and $[\text{Fe}(\text{CN})_6]^{4-}$ returns to $[\text{Fe}(\text{CN})_6]^{3-}$ will provide the electron for the transition process from Co (III) to Co (II) or Mn(III) to Mn(II) (Fig 7B). This performance helps the active material to lose and gain electrons smoothly and improves the capacitive performance [41].

Comparing all the curves, we see that the Co-Mn electrode in the mixed KOH/ $\text{K}_3\text{Fe}(\text{CN})_6$ electrolyte has a bigger area under the curve, implying high specific capacitance. The calculated specific capacitances from the CV at 5 mVs^{-1} are as follows: 210 Fg^{-1} , 757 Fg^{-1} , and 1658 Fg^{-1}

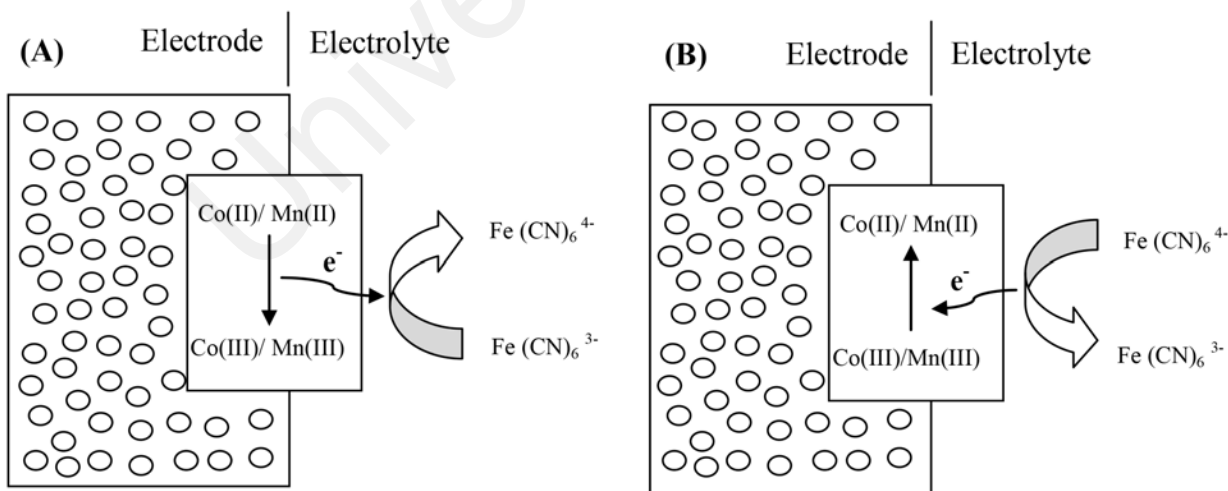


Fig 7. Schematic of the role of hexacyanoferrate (II) and (III) in the process of: (A) charge and (B) discharge of Co-Mn electrode.

doi:10.1371/journal.pone.0129780.g007

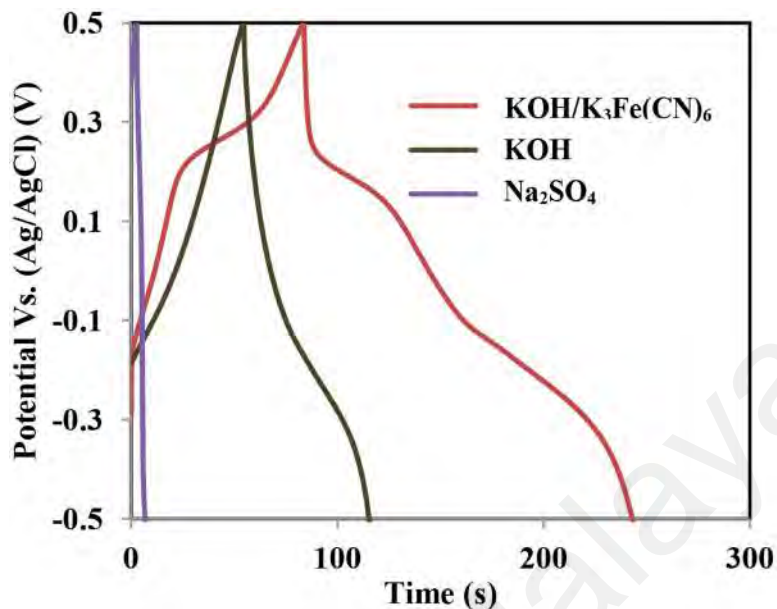


Fig 8. Charge-discharge profiles of Co-Mn electrode at current density of 10 Ag^{-1} in three different electrolytes.

doi:10.1371/journal.pone.0129780.g008

for Na_2SO_4 , KOH, and mixed $\text{KOH}/\text{K}_3\text{Fe}(\text{CN})_6$ electrolytes, respectively. The areal capacitances of the Co-Mn samples in three electrolytes at different scan rates is shown in Fig 6F. The low scan rate results in a higher specific capacitance, due to the slow charging/discharging process in which the cation could access almost all available pores and materials was fully utilized [20]. The importance of $\text{K}_3\text{Fe}(\text{CN})_6$ has been confirmed by the enhancement of specific capacitance and improvement of electrode stability, suggesting that the mixed electrolyte is the stable electrolyte for the Co-Mn electrode.

Fig 8 illustrates the charge/discharge profiles of Co-Mn in Na_2SO_4 , KOH, and mixed $\text{KOH}/\text{K}_3\text{Fe}(\text{CN})_6$ electrolytes at a current density of 10 Ag^{-1} . The voltage range applied is from -0.5V to 0.5V. The charge/discharge profile displayed a slightly non-linear curve, which represented the pseudocapacitance characteristic resulting from the faradic reaction in the studied voltage range [43]. The specific capacitance, energy, and power densities calculated from the discharging curve for the mixed $\text{KOH}/\text{K}_3\text{Fe}(\text{CN})_6$ electrolyte are 2222 Fg^{-1} , 309 Whkg^{-1} , and 73 kWkg^{-1} at a current density of 10 Ag^{-1} . In the KOH and Na_2SO_4 electrolytes, the specific capacitances of 909 Fg^{-1} and 39 Fg^{-1} were obtained. The energy and power densities of Co-Mn electrodes in KOH and Na_2SO_4 electrolytes are 126 Whkg^{-1} , 5 Whkg^{-1} , 82 kWkg^{-1} , and 24 kWkg^{-1} , respectively.

Conclusions

In summary, we have successfully fabricated a MnO_2 -based binder-free composite electrode material using the electrodeposition method. The composite electrode was obtained when a layer of secondary and ternary metal oxide containing Co, Mn, and Ni was ex situ deposited on a MnO_2 particle layer by the same method. From the FESEM and TEM studies, we observed that the MnO_2 particles were encapsulated by the second deposited metal oxide layer and had a strong influence on the electrochemical performance of the electrode. The capacitive performance of the Co-Mn electrode in the 0.5M Na_2SO_4 electrolyte exhibits the highest specific capacitance (285 Fg^{-1} with a current density of 1.85 Ag^{-1}), the smallest R_s and R_{ct} , and a high

knee frequency of 356 Hz. The performance of the electrochemical capacitor in a three-electrode system employing the Co-Mn electrode in KOH and mixed KOH/ $K_3Fe(CN)_6$ electrolytes confirms the importance of $K_3Fe(CN)_6$ in terms of specific capacitance enhancement and electrode stability. The calculated specific capacitance and energy density of the Co-Mn electrode in the mixed electrolyte was $2.2 \times 10^3 \text{ Fg}^{-1}$ and 309 Whkg^{-1} at a current density of 10 Ag^{-1} . These statistics show Co-Mn electrode's great potential for use as an electric energy storage device for hybrid vehicles.

Acknowledgments

The authors thank the University of Malaya for financial assistance through grants (UM.C/625/1/HIR/157, RP025B-14AFR) and PG010-2013A. Rusi acknowledges the Skim Bright Sparks University Malaya (SBSUM) for the scholarship award.

Author Contributions

Conceived and designed the experiments: R SRM. Performed the experiments: R PYC. Analyzed the data: R SRM. Contributed reagents/materials/analysis tools: SRM. Wrote the paper: R SRM.

References

1. Conway BE. *Electrochemical Supercapacitors: Scientific Fundamentals and Technological Applications*. New York: Kluwer-Plenum; 1999.
2. Hung CJ, Lin P, Tseng LY. Electrophoretic fabrication and pseudocapacitive properties of graphene/manganese oxide/carbon nanotube nanocomposites. *Journal of Power Sources* 2013; 243: 594–602.
3. Yun TG, Oh M, Hu L, Hyun S, Han SM. Enhancement of electrochemical performance of textile based supercapacitor using mechanical pre-straining. *Journal of Power Sources* 2013; 244: 783–791.
4. Lu X, Yu M, Wang G, Tong Y, Li Y. Flexible solid-state supercapacitors: design, fabrication and applications. *Energy Environmental Science* 2014; 7: 2160–2181.
5. Babakhani B, Ivey DG. Anodic deposition of manganese oxide electrodes with rod-like structures for application as electrochemical capacitors. *Journal of Power Sources* 2010; 195: 2110–2117.
6. Lokhande CD, Dubal DP, Joo OS. Metal oxide thin film based supercapacitors. *Current Applied Physics* 2014; 11: 255–270.
7. Wei WF, Cui XW, Chen WX, Ivey DG. Manganese oxide-based materials as electrochemical supercapacitor electrodes. *Chemical society reviews* 2011; 40: 1697–1721. doi: [10.1039/c0cs00127a](https://doi.org/10.1039/c0cs00127a) PMID: [21173973](https://pubmed.ncbi.nlm.nih.gov/21173973/)
8. Sharma AS, Sharma Y, Malhotra R, Sharma JK. Solvent Tuned PANI-CNT Composites As advanced Electrode Materials For Supercapacitor. *Advanced materials letters* 2012; 3(2): 82–86.
9. Enachi M, Lupan O, Braniste T, Sarua A, Chow L, Mishra YK, Gedamu D, Adelung R, Tiginyan I. Integration of individual TiO₂ nanotube on the chip: Nanodevice for Hydrogen sensing. *Rapid Research Letters* 2015; 9:171–174.
10. Lupan O, Ghimpu L, Reimer T, Hoppe M, Paulowicz I, Gedamu D, Mishra YK, Hammerich D, Chemnitz S, Cretu V, Tiginyan I, Adelung R. Magnetron Sputtering and Characterization of Doped Zinc Oxide Nanofibrous Films and Their Applications. *Journal of Nanoelectronics and Optoelectronics*. 2014; 9:257–264.
11. Kumar M, Sandeep CSS, Kumar G, Mishra YK, Philip R & Reddy GB. Plasmonic and Nonlinear Optical Absorption Properties of Ag:ZrO₂ Nanocomposite Thin Films. *Plasmonics* 2014; 9:129–136.
12. Trigilio J, Antoine TE, Paulowicz I, Mishra YK, Adelung R, Shukla D. Tin oxide nanowires suppress herpes simplex virus-1 entry and cell-to-cell membrane fusion. *Plos One* 2012; 7:48147.
13. Hu CC, Hung CY, Chang KH, Yang YL. A hierarchical nanostructure consisting of amorphous MnO₂, Mn₃O₄ nanocrystallites, and single-crystalline MnOOH nanowires for supercapacitors. *Journal of Power Sources* 2011; 196: 847–850.
14. Li SH, Liu QH, Qi L, Lu LH, Wang HY. Progress in Research on Manganese Dioxide Electrode Materials for Electrochemical Capacitors. *Chinese Journal of Analytical Chemistry* 2012; 40: 339–346.

15. Wu CH, Ma JS, Lu CH. Synthesis and characterization of nickel–manganese oxide via the hydrothermal route for electrochemical capacitors. *Current Applied Physics* 2012; 12: 1190–1194.
16. Gobal F, Jafarzadeh S. A comparative study of sequentially layer-deposited and co-deposited Co–Mn oxides as potential redox capacitors. *Journal of Solid State Electrochemistry* 2012; 16: 1561–1569.
17. Lee MH, Lee K, Kim CK. Electrodeposition of Manganese-Nickel Oxide Films on a Graphite Sheet for Electrochemical Capacitor Applications. *Materials* 2014; 7: 265–274.
18. Rajendra PK, Miura N. Electrochemically synthesized MnO₂-based mixed oxides for high performance redox supercapacitors. *Electrochemistry Communications* 2014; 6: 1004–1008.
19. Jagadale AD, Kumbhar VS, Lokhande CD. Supercapacitive activities of potentiodynamically deposited nanoflakes of cobalt oxide (Co₃O₄) thin film electrode. *Journal of Colloid and Interface Science* 2013; 406: 225–230. doi: [10.1016/j.jcis.2013.05.037](https://doi.org/10.1016/j.jcis.2013.05.037) PMID: [23827481](https://pubmed.ncbi.nlm.nih.gov/23827481/)
20. Rusi, Majid SR. Controllable synthesis of flowerlike α-MnO₂ as electrode for pseudocapacitor application. *Solid State Ionics* 2014; 262: 220–225.
21. Wu XY, Chen P, Wu QS, Yang LF, Pan Z, Wang Q. Co/Co₃O₄/C–N, a novel nanostructure and excellent catalytic system for the oxygen reduction reaction. *Nano Energy* 2014; 8: 118–125.
22. Hwang BJ, Santhanam R, Lin YL. Nucleation and Growth Mechanism of Electropolymerization of Polypyrrole on Gold/Highly Oriented Pyrolytic Graphite Electrode. *Journal of Electrochemical Society* 200; 147: 2252–2257.
23. Babakhani B, Ivey DG. Effect of electrodeposition conditions on the electrochemical capacitive behavior of synthesized manganese oxide electrodes. *Journal of Power Sources* 2011; 196: 10762–10774.
24. Rusi, Majid SR. Synthesis of MnO₂ particles under slow cooling process and their capacitive performances. *Materials Letters* 2013; 108: 69–71.
25. Li Y, Xie H, Wang J, Chen L. Preparation and electrochemical performances of α-MnO₂ nanorod for supercapacitor. *Materials Letters* 2011; 65: 403–405.
26. Wang Y, Shi JC, Cao JL, Sun G, Zhang XY. Synthesis of Co₃O₄ nanoparticles via the CTAB-assisted method. *Materials Letters* 2011; 65: 222–224.
27. Gujar TP, Shinde VR, Lokhande CD, Kim WY, Jung KD, Joo OS. Spray deposited amorphous RuO₂ for an effective use in electrochemical supercapacitor. *Electrochemistry Communications* 2007; 9: 504–510.
28. Saranya S, Selvan RK, Priyadharsini N. Synthesis and characterization of polyaniline/MnWO₄ nanocomposites as electrodes for pseudocapacitors. *Applied Surface Science* 2012; 258: 4881–4887.
29. Li Z, Wang J, Niu L, Sun J, Gong P, Hong W, et al. Rapid synthesis of graphene/cobalt hydroxide composite with enhanced electrochemical performance for supercapacitors. *Journal of Power Sources* 2014; 245: 224–231.
30. Zhang YX, Huang M, Li F, Wang XL, Wen ZQ. One-pot synthesis of hierarchical MnO₂-modified diatomites for electrochemical capacitor electrodes. *Journal of Power Sources* 2014; 246: 449–456.
31. Chen Y, Wang JW, Shi XC, B.Z. Chen BZ. Pseudocapacitive characteristics of manganese oxide oxidized from manganese coating electrodeposited from aqueous solution. *Electrochimica Acta* 2013; 109: 678–683.
32. Sugimoto W, Iwata H, Yokoshima K, Murakami Y, Takasu Y. Proton and Electron Conductivity in Hydrous Ruthenium Oxides Evaluated by Electrochemical Impedance Spectroscopy: The Origin of Large Capacitance. *Journal of Physical Chemistry B* 2015; 109: 7330–7338.
33. Cai Y, Wang Y, Deng S, Chen G, Li Q, Han B, et al. Graphene nanosheets-tungsten oxides composite for supercapacitor electrode. *Ceramics International* 2014; 40: 4109–4116.
34. Ding R, Qi L, Jia M, Wang H. Facile and large-scale chemical synthesis of highly porous secondary submicron/micron-sized NiCo₂O₄ materials for high-performance aqueous hybrid AC–NiCo₂O₄ electrochemical capacitors. *Electrochimica Acta* 2013; 107: 494–502.
35. Hyun TS, Tuller HL, Youn DY, Kim HG, Kim ID. Facile synthesis and electrochemical properties of RuO₂ nanofibers with ionically conducting hydrous layer. *Journal of Materials Chemistry* 2010; 20: 9172–9179.
36. Girija TC, Sangaranarayanan MV. Analysis of polyaniline-based nickel electrodes for electrochemical supercapacitors. *Journal of Power Sources* 2016; 156: 705–711.
37. Farsi H, Gobal F, Raissi H, Moghiminia S. On the pseudocapacitive behavior of nanostructured molybdenum oxide. *Journal of Solid State Electrochemistry* 2010; 14: 643–650.
38. Engstrom AM and Doyle FM. Exploring the cycle behavior of electrodeposited vanadium oxide electrochemical capacitor electrodes in various aqueous environments. *Journal of Power Sources* 2013; 228: 120–131.

39. Zhao C, Zheng W, Wang X, Zhang H, Cui X, Wang H. Ultrahigh capacitive performance from both Co (OH)₂/graphene electrode and K₃Fe(CN)₆ electrolyte. *Scientific Reports* 2013; 3: 2986–2992.
40. Nithya VD, Kalai SR, Kalpana D, Vasylechko L, Sanjeeviraja C. Synthesis of Bi₂WO₆ nanoparticles and its electrochemical properties in different electrolytes for pseudocapacitor electrodes. *Electrochimica Acta* 2013; 109: 720–731.
41. Chen K, Song S, Xue D. An ionic aqueous pseudocapacitor system: electroactive ions in both a salt electrode and redox electrolyte. *RSC advances* 2014; 4: 23338.
42. Ling HS, Xiao GZ, Chang HM, Bo G, and Yan L. Improvement of capacitive performance for Co-Al layered double hydroxide by adding hexacyanoferrate into the electrolyte. *Physical Chemistry Chemical Physics* 2009; 11: 2195–2202 doi: [10.1039/b814844a](https://doi.org/10.1039/b814844a) PMID: [19305892](https://pubmed.ncbi.nlm.nih.gov/19305892/)
43. Dubal DP, Gund GS, Holze R, Jadhav HS, Lokhande CD, Park CJ. Solution-based binder-free synthetic approach of RuO₂ thin films for all solid state supercapacitors. *Electrochimica Acta* 2013; 103: 103–109.

University of Malaya